Investigation of magnetotransport properties in Ni/Pt and Co/Pd layered structures

Dissertation
with the aim of achieving a doctoral degree
at the faculty of physics
Universität Hamburg

submitted by
Afsaneh Farhadi Ghalati

Hamburg
2018

Gutachter der Dissertation:

Prof. Dr. Hans Peter Oepen
Universität Hamburg

Prof. Dr. Wolfgang Hansen
Universität Hamburg

Gutachter der Disputation:

Prof. Dr. Hans Peter Oepen
Universität Hamburg

Prof. Dr. Wolfgang Hansen
Universität Hamburg

Prof. Dr. Michael Thorwart
Universität Hamburg

Prof. Dr. Dorota Koziej
Universität Hamburg

Prof. Dr. Caren Hagner
Universität Hamburg

Datum der Disputation: 21.06.2018

Vorsitzender des Prüfungsausschusses: Prof. Dr. Wolfgang Hansen

Vorsitzende des Promotionsausschusses: Prof Dr. Michael Potthoff

Dekan der Fakultät für Mathematik,
Informatik und Naturwissenschaften: Prof. Dr. Heinrich Graener

Abstract

In this thesis two topics in the field of magnetotransport properties of thin ferromagnetic layered structure in current in-plane (CIP) geometry are studied.

First the magnetoresistance effects in Ni/Pt system were investigated in the temperature range of $4.2 \leq T \leq 295\,\mathrm{K}$. In Pt/Co/Pt the resistivity behaves as $\rho(\varphi, \theta) = \rho_{\mathrm{t}} + \Delta\rho_{\mathrm{ip}} \cos^2\varphi \sin^2\theta + \Delta\rho_{\mathrm{op}} \cos^2\theta$ where φ/θ is the angle between magnetization and current direction/film normal. While $\Delta\rho_{\mathrm{ip}}$ is caused by the conventional AMR (bulk effect) a $\Delta\rho_{\mathrm{op}} \propto 1/t$ behavior was found for Pt(5nm)/Co(t)/Pt(3nm) sandwiches revealing that $\Delta\rho_{\mathrm{op}}$ originates at the Co/Pt interfaces (anisotropic interface magnetoresistance (AIMR)). In order to study interfacial MR contribution in stacking isoelectronic materials Ni/Pt systems were investigated. We prepared Pt(5nm)/Ni(t)/Pt(3nm) sandwiches with Ni thicknesses of 1 - 50 nm by DC magnetron sputtering on Si_3N_4 substrate. As a result, in contrast to previous findings, the $\rho(\theta)$ behavior can only be satisfactorily described when considering higher orders in the expansion of the MR: $\rho(\theta) = \rho_{\mathrm{t}} + \sum_n \Delta\rho_{\mathrm{op},2n} \cos^{2n}\theta$ with $n \leqslant 3$. The thickness dependence of the amplitudes $\Delta\rho_{\mathrm{op},2n}$ behaves according to $1/t$ revealing that also the higher orders have their origin at the Ni/Pt interfaces.

The second topic of this thesis deals with investigation of the impact of aging on the various magnetoresistance effects in Pd/Co/Pd sandwiches at room temperature. By means of sputtering techniques two Pd(5 nm)/Co/Pd(3 nm) samples with 2 and 7 nm Co thicknesses were fabricated on Si_3N_4 substrate and the longitudinal and transverse resistivity of the sandwiches were measured repeatedly over 600 days. The results show strong variations of the MR properties in the first three months followed by a slower change to equilibrium values. However, there are significant differences between both samples reflecting different behavior of Co/Pd systems governed by bulk-like or interface contributions. In order to find a correlation between the changes occurring in MR effects and the structural properties of the samples, XRR measurements accompanied the transport investigations over time. It is concluded that gradual intermixing of Co and Pd at the interfaces and absorption of hydrogen are the two mechanisms responsible for the aging effect in Pd/Co/Pd systems.

Kurzzusammenfassung

Im Rahmen dieser Doktorarbeit werden zwei Themen aus dem Feld der Magnetotransporteigenschaften von ferromagnetischen Systemen untersucht, wobei der Strom entlang der Schichtebenen eingeprägt wurde.
Zum einen werden die Magnetowiderstandseffekte in Ni/Pt-Schichtsystemen im Temperaturbereich von $4.2 \leq T \leq 295\,\mathrm{K}$ untersucht. In Pt/Co/Pt-Schichtsystemen kann der Widerstand mit $\rho(\varphi,\theta) = \rho_\mathrm{t} + \Delta\rho_\mathrm{ip}\cos^2\varphi\sin^2\theta + \Delta\rho_\mathrm{op}\cos^2\theta$ beschrieben werden, wobei φ/θ der Winkel zwischen der Magnetisierung und der Stromrichtung/Filmnormalen ist. Während $\Delta\rho_\mathrm{ip}$ durch den normalen AMR (Bulk Effekt) verursacht wird, wird ein $\Delta\rho_\mathrm{op} \propto 1/t$ Verhalten für Pt(5nm)/Co(t)/Pt(3nm) Multilagen gefunden. Dies zeigt, dass $\Delta\rho_\mathrm{op}$ an der Co/Pt Grenzfläche entsteht (anisotroper Grenzflächenmagnetowiderstand (AIMR)[1]). Um den Grenzflächenbeitrag des Magnetowiderstandes in geschichteten isoelektrischen Materialen zu studieren wurden Ni/Pt Systeme untersucht. Dafür wurden Pt(5nm)/Ni(t)/Pt(3nm)-Sandwichstrukturen mit einer Ni-Dicke von 1 - 50 nm mittels DC-Magnetron-Sputtern auf Si_3N_4 als Substrat hergestellt. Im Gegensatz zu früheren Untersuchungen wurde festgestellt, dass das $\rho(\theta)$ Verhalten nur dann zufriedenstellend beschrieben werden kann, wenn höhere Ordnungen in der Entwicklung des MR berücksichtigt werden: $\rho(\theta) = \rho_\mathrm{t} + \sum_n \Delta\rho_{\mathrm{op},2n}\cos^{2n}\theta$ mit $n \leqslant 3$. Da die Dickenabhängigkeit der Amplitude $\Delta\rho_{\mathrm{op},2n}$ einem $1/t$ Verhalten folgt, konnte gezeigt werden, dass auch die höheren Ordnungen ihren Ursprung in der Ni/Pt-Grenzfläche haben.
Das zweite Thema, das in der vorliegenden Arbeit untersucht wird, behandelt den Einfluss der Probenalterung auf diverse Magnetowiderstandseffekte in Pd/Co/Pd-Schichtsystemen bei Raumtemperatur. Zwei Pd(5 nm)/Co/Pd(3 nm) Proben mit 2 und 7 nm Co-Dicke wurden mittels Sputterdeposition auf Si_3N_4-Substrate gewachsen um anschließend den longitudinalen und transversalen Widerstand der Schichtsystemen über 600 Tagen wiederholt zu messen. Die Ergebnisse zeigen eine starke Änderung der MR-Eigenschaften in den ersten drei Monaten, welche sich anschließend langsam einem Gleichgewichtswert annähern. Dennoch existieren signifikante Unterschiede zwischen beiden Proben, welche auf den unterschiedlichen Einfluss der Bulkähnlichen- oder Grenzflächenbeiträge in den Co/Pd-Proben zurückgeführt werden können. Um einen Zusammenhang zwischen den Änderungen in den MR-Effekten und strukturellen Eigenschaften der Proben zu finden haben regelmäßige XRR Messungen die Untersuchung begleitet. Es kann geschlussfolgert werden, dass die beiden verantwortlichen Mechanismen für den Alterungseffekt in Pd/Co/Pd-Systemen sowohl die graduelle Vermischung von Co und Pd an den Grenzflächen als auch die Absorption von Wasserstoff ist.

---

[1] engl. anisotropic interface magnetoresistance

Contents

---

afarhadi@physnet.uni-hamburg.de

Chapter 1

Introduction

Nowadays research in the field of *magnetic materials* is largely driven by the fast moving pace in the development of information technology, especially data storage and memory applications [1]. Moreover, conventional magnetic materials have long been used for various applications including electric motors and *sensors* [2]. Among all kind of sensors, *magnetic sensors* have assisted mankind in analyzing and controlling thousands of functions for many decades. Computers have nearly unlimited memory through the use of magnetic sensors while airplanes fly with higher safety standards because of the high reliability of non-contact switching with magnetic sensors. Automobiles use magnetic sensors to track the position and operational state of several components such as the engine crank shaft and wheel braking [3, 4]. They also play an important role in many security and military systems [5, 6].

Magnetic thin films are technologically important as they exhibit novel physical phenomena as a result of their reduced size and dimensionality [7]. Sensors based on thin magnetic films found many industrial and commercial applications in the past 20 years. By far the most important of them are magnetoresistive sensors (e.g. anisotropic magnetoresistance sensors), which have reached a 100 times higher field resolution than Hall sensors with the same size and power consumption [8].

In materials used as anisotropic magnetoresistance (AMR) sensors, the resistance depends on the direction of magnetization with respect to the current flow [3, 9]. Due to AMR, the resistance changes with the $\cos^2$ of the angle between magnetization and the direction of current. Permalloy (an alloy containing about 80% nickel and 20% iron) is the most common material for magnetoresistive sensors because it has a relatively high magnetoresistive coefficient [4]. Such magnetoresistive sensors have a sensitivity range of 10^3 - 5×10^6 nT.

Giant magnetoresistance (GMR) effect was first observed in the late 1980s and the 2007 Nobel prize in Physics was awarded to Fert and Grünberg for their discovery of GMR. The GMR effect occurs in multilayers in which thin layers of magnetic material are separated by thin layers of nonmagnetic metals. Notably the typical GMR values are one order of magnitude larger than those in AMR materials, however, GMR is not observed in all systems.

Accordingly, in systems without GMR like Co/Pt and Co/Pd layered structures another interesting magnetoresistance behavior was found in our group. As a result in 2011 a new magnetoresistance effect in Co/Pt system was found by A. Kobs et al. which originates from the Co/Pt interfaces [10]. Therefore, the effect was coined anisotropic interface magnetoresistance (AIMR) [10, 11]. Due to this effect the resistance shows a $\cos^2$ behavior when the magnetization is rotated in the plane perpendicular to the current direction. According to AIMR, the resistivity of Co/Pt is maximum when the magnetization is directed parallel to the film normal $\mathbf{n}$.

Investigating the magnetization dependence of resistance in similar layered systems (e.g. Ni/Pt and Co/Pd) was the motivation of this work. This led to the observation of a completely different behavior for Ni/Pt when the magnetization is rotated perpendicular to the current direction. Notably, Ni is one of the strong 3d ferromagnetic elements and already one of the most encountered components in spintronics applications because of its relatively high AMR ratio [12, 13]. It is observed in many studies that Ni perform different physical properties from other materials, e.g., Fe and Co [12].

Within the framework of this thesis the magnetoresistance properties of Ni/Pt and Co/Pd layered structure are presented and discussed. For this purpose, the theoretical basics of magnetic anisotropy and galvamagnetic effects used in this work are briefly introduced in chapter 2.

In chapter 3, I present the experimental methods used for magnetoresistance measurements and structural investigations. Furthermore, the setup used for sample preparation is explained.

Chapter 4 deals with the magnetoresistance effects measured for Pt/Ni/Pt sandwiches. The observation of higher order contributions to the out-of-plane-AMR (op-AMR) is the main achievement of this work. It is found that, in contrast to Co/Pt, when the magnetization rotates by an angle θ in the plane perpendicular to the current, the resistivity can be described by $\sum \cos^{(2n)} \theta$, $n \leqslant 3$. This behavior was found in the whole temperature range of 4 - 300 K studied in this thesis.

Co/Pd multilayers with perpendicular anisotropy are one of the interesting topics in ultrahigh density magnetic recording media and spintronics devices [14–16]. However, in contrast to Co/Pt system, it is reported recently that some magnetoresistance properties of Co/Pd system are changed after preparation [17–19]. Therefore, I illustrate the impact of aging process on magnetotransport effects and structural properties occurred in Co/Pd layered structure in chapter 5. In a time span of 600 days after preparation, it is found that AMR and AIMR effects of Co/Pd system change with time. Moreover, the trace of aging also observed in XRR measurements proves the correlation between MR effects and the changes of structural properties.

Chapter 2

Theory of magnetism

In this work the magnetotransport properties of Ni/Pt and Co/Pd systems are studied. For this purpose, the necessary fundamentals of ferromagnetism in thin films are introduced briefly in this chapter. I start with introducing the energy contributions of a ferromagnet in Sec. 2.1, and continue with explaining these energy contributions shortly after that.

Subsequently, in Sec. 2.2 the magnetoresistance effects, which are utilized to described the transport properties of studied systems, are presented. It is worth noticing that a comprehensive description of micromagnetism can be found in relevant textbooks [20–23].

2.1 Micromagnetic energy

Generally, a ferromagnetic material can be defined as a material that possesses a spontaneous *magnetization* M_s, independent on an applied magnetic field. The total free energy of such a material consists of four types of magnetic energy contribution [24]:

$$E_{\mathrm{tot}} = E_{\mathrm{xc}} + E_{\mathrm{mca}} + E_{\mathrm{d}} + E_{\mathrm{Z}} \tag{2.1}$$

The first three terms due to exchange (E_{xc}), magnetocrystalline anisotropy (E_{mca}) and demagnetizing field (E_{d}) are always existent to some extent in thin layered structures that we have studied in this thesis. Basically, E_{xc} is caused by the exchange interaction and has the largest contribution. The demagnetizing field is another contribution which correlates the shape of the sample with magnetic anisotropy. Furthermore, Zeeman energy (E_{Z}) is the response of material to the external magnetic field. In the following the corresponding energy contributions to this work are briefly discussed.

2.1.1 Exchange interaction

Exchange interaction is a pure quantum mechanical effect and is a result of Coulomb interaction and Pauli's exclusion principle. In a two-spin system, the exchange energy is defined as the energy difference between the parallel and antiparallel spin configuration.
According to Pauli's exclusion principle and the fact that electrons are fermions, the wave function of this two-spin system must be antisymmetric. Therefore, it can obtain one of these two options: a symmetric spatial part combined with an antisymmetric spin wave function or vice versa [25]. This means that the total wave function can be written as

$$\psi_{S,T} = \frac{1}{\sqrt{2}}(\varphi_a(\mathbf{r}_1)\varphi_b(\mathbf{r}_2) \pm \varphi_a(\mathbf{r}_2)\varphi_b(\mathbf{r}_1)) \cdot \chi_{S,T} \tag{2.2}$$

The idea of expressing the exchange interaction as an effective interaction between electron spins and neighboring atoms was first applied by Heisenberg. The correlation can be expressed in the form of dot product of the spins.

$$H_{\mathrm{xc}} = -2\sum_{i>j} J_{ij}\mathbf{S}_i \cdot \mathbf{S}_j \tag{2.3}$$

where J_{ij} is the exchange integral. If $J > 0$, the exchange energy has a minimum in the case of parallel spins and has a maximum in the case of antiparallel spins. Therefore, a positive value of J_{ij} is a necessary condition for ferromagnetism to occur. Values of $J \approx 0.01 - 0.02\,\mathrm{eV}$ have been determined for ferromagnetic metals (Ni and Fe) by Hofmann et al. [26].

2.1.2 Magnetocrystalline anisotropy

The dependence of magnetization orientation on the crystallographic direction is known as magnetocrystalline anisotropy, which is an intrinsic property of the material. The physical origin of magnetocrystalline anisotropy is spin-orbit coupling. Due to the inadequate accuracy in quantitative evaluation of the spin-orbit interaction, anisotropy energies are normally written as phenomenological expressions. Thus, the best way to express these anisotropies is by using power series expansions based on the crystal symmetry. Therefore specific expressions are given for a specific crystalline symmetry, i.e., cubic crystal and uniaxial crystal. Before going into details the spin-orbit coupling is biefly introduced.

Spin-orbit interaction

In contrast to spin-spin interaction (see Sec. 2.1.1), which is strong and isotropic, the interaction between the spin and the orbital motion of electron is a weak (fields of a few tens of kA/m is enough to rotate the spins) and anisotropic coupling.

It is the origin of some phenomena in magnetism, including magnetocrystalline anisotropy, magnetostriction, anisotropic magnetoresistance and spin Hall effect. From the electron's point of view, a positive charge (nucleus) is rotating around it and therefore produces a magnetic field at the origin that can interact with the spin of electron. So, the potential energy can be expressed as

$$U_{l,s} = -\boldsymbol{\mu_s} \cdot \mathbf{B} = \frac{A}{\hbar^2}\, \mathbf{L} \cdot \mathbf{S} \tag{2.4}$$

where $\boldsymbol{\mu_s}$ is the spin magnetic moment and $A \propto \frac{Z^4}{n^3}$, $\mathbf{L}$ and $\mathbf{S}$ are orbital and spin angular momentum, respectively, while Z is the atomic number and n is the quantum number. The Z proportionality demonstrates that spin-orbit interaction is weak for light elements and becomes much more important for heavy elements, specially for inner shells. More details can be found in Ref. [27].
In the next section, the magnetocrystalline anisotropy is explained and some certain crystal symmetries are reviewed.

Anisotropy in cubic crystals

An appropriate way to expand the magnetocrystalline energy for cubic crystals is in powers of the direction cosines, α_1, α_2, and α_3, of the magnetization relative to crystal axes. Under the symmetry of the crystal, the odd powers are ruled out and the first non-vanishing order is proportional to $\alpha_1^2 + \alpha_2^2 + \alpha_3^2$, which is a constant and equal to 1 for arbitrary α_i. Hence, the expansion of energy starts with forth power and can be written as

$$E_{\mathrm{mca}}^{\mathrm{cubic}}/V = K_0 + K_1^{\mathrm{cub}}(\alpha_1^2\alpha_2^2 + \alpha_2^2\alpha_3^2 + \alpha_3^2\alpha_1^2) + K_2^{\mathrm{cub}}(\alpha_1^2\alpha_2^2\alpha_3^2) + \cdots \tag{2.5}$$

where the values of K_1^{cub} and K_2^{cub} are anisotropy constants which are taken from experiments. Because K_0 is independent of the magnetization direction, it is meaningless in anisotropy properties. Generally, the experience proves that the constants K_1^{cub} and K_2^{cub} are sufficient for a good agreement between experiment and calculation [22]. In addition, the coefficients depend on material and temperature. On the other hand, sign and ratio of the constants determine the easy magnetization axis or the preferred axis. As an example the magnitude of anisitropy constants $K_1 = -126.3\,\mathrm{kJ/m^3}$ and $K_2 = 57.8\,\mathrm{kJ/m^3}$ were measured for fcc-Ni at $T = 4.2\,\mathrm{K}$ by Getzlaff et al. [25], while at room temperature the both constants were found negative for nickel ($K_1 = -5.7\,\mathrm{kJ/m^3}$, $K_2 = -2.3\,\mathrm{kJ/m^3}$) [28]. considering only the dominant constant, $K_1^{\mathrm{cub}} > 0$ yields an easy magnetization directions along $< 100 >$ which is called iron-type anisotropy (see Fig. 2.1(b)). Similarly, for $K_1^{\mathrm{cub}} < 0$ the preferential magnetization direction are parallel to $< 111 >$ and known as nickel-type anisotropy (see Fig. 2.1(c)).

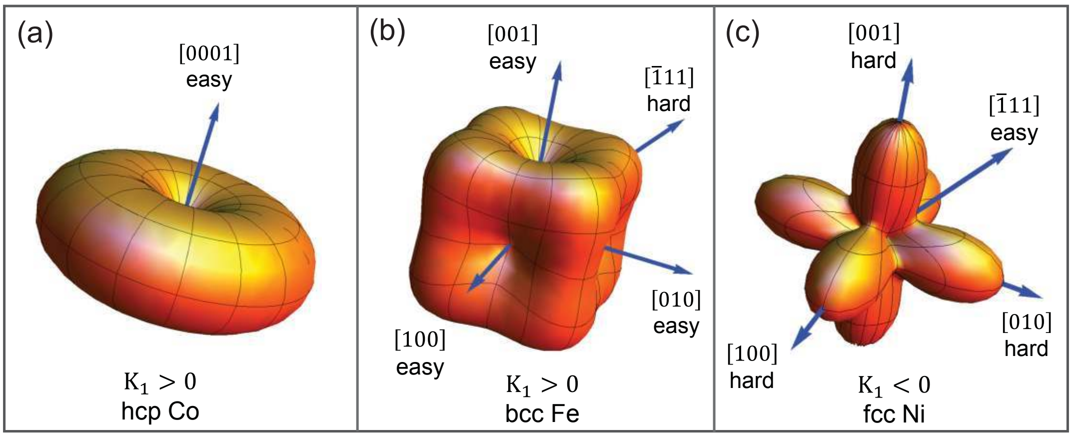

Figure 2.1: The energy density in polar plot of (a) hcp Co (b) bcc Fe and (c) fcc Ni.

However, considering the additional anisotropy constant K_2^{cub} may significantly vary the magnetic properties. For example, it was observed that the ratio of K_1/K_2 for Fe is about 250 and for Ni is about 2 [25].

Anisotropy in Hexagonal crystals

The c axis in hexagonal crystals is the direction of easy magnetization and all directions in the plane perpendicular to c axis are found to be hard. Such a crystal with a single outstanding axis is called a uniaxial crystal. Therefore the anisotropy of these materials (such as hcp-Co) is a function of the angle θ between c axis and the direction of magnetization:

$$E_{\mathrm{mca}}^{\mathrm{uni}}/V = K_0 + K_1^{\mathrm{uni}} \sin^2\theta + K_2^{\mathrm{uni}} \sin^4\theta + \cdots \tag{2.6}$$

where K_1^{uni} and K_2^{uni} are anisotropy constants of first and second order which depend strongly on temperature and K_0 again means a shift in the definition of the zero energy. Fig. 2.2 illustrates the temperature dependence of K_1^{uni} and K_2^{uni} for Co [23, 25]. According to Ibach and Lüth [28] the magnetocrystalline anisotropy $K_1^{\mathrm{uni}} = 410\,\mathrm{kJ/m^3}$ and $K_2^{\mathrm{uni}} = 100\,\mathrm{kJ/m^3}$ were obtained for hcp-Co at room temperature. In most hexagonal crystals, where the c axis is an easy axis, K_1 is positive (see Fig. 2.1(a)). However, there are materials with negative K_1, in which the easy plane is perpendicular to c axis. Fig. 2.1 shows the shape of the energy surface for Co, Fe, and Ni according to Eq. 2.5 and 2.6, respectively.

Surface or interface anisotropy

Another anisotropic energy term, first introduced by Néel in 1954 [29], is a surface contribution which considerably differs from the magnetic anisotropy in the bulk. Because the spin at the surface has a nearest neighbour on one side and none on the

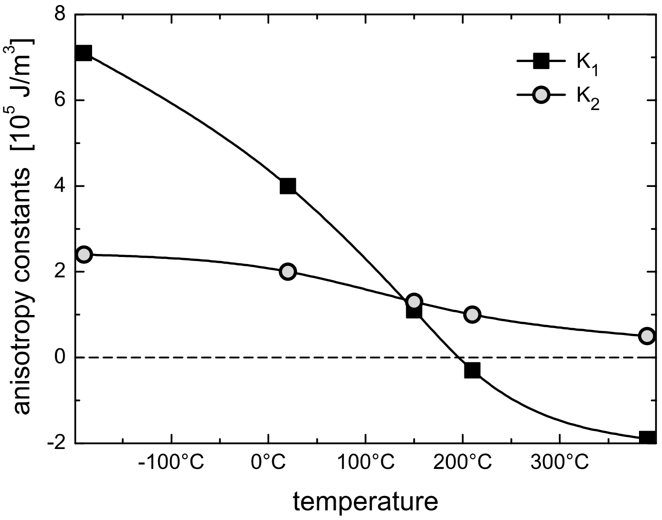

Figure 2.2: Temperature dependence of the magnetocrystalline anisotropy constants of hcp-Co [23].

other side, so that the exchange energy cannot be the same as in the bulk [22]. The perpendicular magnetic anisotropy (PMA) in many thin films is a result of surface anisotropy due to broken symmetry at the surface or interface. Surface anisotropy can be expressed as

$$E_\mathrm{s}/V = 2K_\mathrm{s}\left[1 - (\mathbf{m}\cdot\mathbf{n})^2\right]/t = \frac{2K_\mathrm{s}\sin^2\theta}{t} \tag{2.7}$$

where $\mathbf{n}$ is the surface normal, $\mathbf{m} = \dfrac{\mathbf{M}}{|\mathbf{M}|}$, and θ is the angle between both quantities. The energy should be integrated over the surface and the factor 2 is due to the two interfaces of the magnetic layer. Surface anisotropy was first measured by Gradmann and Müller on NiFe samples [30]. They showed that there is a proportionality between magnetic anisotropy and inverse of the thickness t. Afterwards the magnetic surface anisotropy of ferromagneic layers in contact with Pd, Pt, Cu, $\cdots$ has been investigated in different temperature [31–35]. As an example, Chafai et al. have measured the surface anisotropy of Ni/Pd multilayers $K_\mathrm{s} = 0.03\,\mathrm{mJ/m^2}$ at 295 K, which approximates the value obtained by den Broeder et al. and Jeong and Shin [33–35]. In addition, the value of $K_\mathrm{s} = 0.27$ - $1.29\,\mathrm{mJ/m^2}$ can be found for Co/Pt systems in literature [33, 36, 37]

2.1.3 Shape anisotropy

Shape anisotropy is a measure for the difference in the energy density associated with magnetization in the shortest and longest dimension of a ferromagnetic body. It means that for non-spherical samples there are specific directions which represent easy magnetization axes that are caused only by shape. The shape anisotropy originates from the classical interactions among the dipoles and for a continuous material it follows from Maxwell's equation $\mathbf{\nabla} \cdot \mathbf{B} = 0 \Rightarrow \mathbf{\nabla} \cdot \mathbf{M} = -\mathbf{\nabla} \cdot \mathbf{H}_\mathrm{d}$. The so called demagnetization energy can be evaluated from the interaction between magnetization $\mathbf{M}$ and demagnetizing field $\mathbf{H}_\mathrm{d}$ (see below)

$$E_\mathrm{d}/V = -\frac{\mu_0}{2}\,\mathbf{M} \cdot \mathbf{H}_\mathrm{d}(\mathbf{r}) \tag{2.8}$$

where the integration is over the ferromagnetic body. The factor $\frac{1}{2}$ is introduced in order to avoid counting each dipole's interaction two times.

Demagnetizing fields and factors

When a ferromagnetic material is magnetized with the magnetization pointing perpendicular to the surface, magnetic poles are formed at the surface. These poles cause within the specimen a magnetic field opposite to the direction of magnetization $\mathbf{M}$ which creates it. This field is called demagnetizing field $\mathbf{H}_\mathrm{d}$. The self-demagnetizing action of a magnetized material strongly influences the behavior of magnetic materials in many practical devices. The intensity of the demagnetizing field $\mathbf{H}_\mathrm{d}$ is proportional to the magnetic free pole density and therefore to the magnetization, so we have

$$\mathbf{H}_\mathrm{d} = -\overleftrightarrow{\mathcal{N}}\mathbf{M} \tag{2.9}$$

The constant proportionality $\overleftrightarrow{\mathcal{N}}$ is called the demagnetizing factor and is a tensor of second rank. The demagnetization field is a function of position and magnetization orientation therefore, $\overleftrightarrow{\mathcal{N}}$ should be a tensor function of position and orientation in a given sample. For an ellipsoid which is uniformly magnetized $\mathcal{N}$ is a diagonal tensor and can be calculated [20].

The demagnetization factors for any principle axis of an ellipsoid of any shape have been calculated by Osborn [38]. For a simple case shown in Fig. 2.3 the demagnetizing factors for the three principle axes have a relationship

$$\mathcal{N}_x + \mathcal{N}_y + \mathcal{N}_z = 1 \tag{2.10}$$

According to Brown-Morrish theorem, any uniformly magnetized ferromagnetic body behaves in the same way as an ellipsoid which has the same volume [22]. Therefore, it can be easily obtained that for a sphere $\mathcal{N}_x = \mathcal{N}_y = \mathcal{N}_z = \frac{1}{3}$ is valid. For a sample in the shape of a prolate spheroid with major axis c and minor axes a of equal length (Fig. 2.3), the shape anisotropy according to Eq. 2.8 can be written as

$$E_\mathrm{d}/V = \frac{1}{2}\mu_0 M^2 \mathcal{N}_\mathrm{z} + \underbrace{\frac{1}{2}\mu_0(\mathcal{N}_\mathrm{x} - \mathcal{N}_\mathrm{z})M^2}_{K_\mathrm{d}^\mathrm{ellipsoid}} \sin^2\theta \tag{2.11}$$

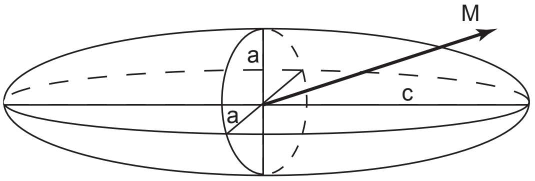

Figure 2.3: Prolate ellipsoid.

This expersion has the same mathematical form as the first-order uniaxial anisotropy term of section 2.1.2, although their physical origins are different. K_d is the shape anisotropy constant. For a very thin film which is infinitely expanded in xy plane, we have $\mathcal{N}_x = \mathcal{N}_y = 0$ and $\mathcal{N}_z = 1$. Therefore

$$E_\mathrm{d}/V = \frac{1}{2}\mu_0 M^2 \underbrace{-\frac{1}{2}\mu_0 M^2}_{K_\mathrm{d}^\mathrm{film}} \sin^2\theta \tag{2.12}$$

In principle, the demagnetizing factors can be calculated by evaluating the potential of the surface charge in Maxwell equations and solve them for boundary conditions [22]. Details of such evaluation of demagnetizing factors can be found in literature and are outside the scope of this thesis [39].

2.1.4 Effective magnetic anisotropy

The effective magnetic anisotropy of multilayers can be expressed as a phenomenological model by superposition of volume anisotropy and surface/interface contribution as

$$K_\mathrm{1,eff} = K_\mathrm{1V,eff} + 2K_\mathrm{s}/t \tag{2.13}$$

with $K_\mathrm{1V,eff}$ being the volume dependent anisotropy constant and K_s the surface dependent magnetocrystalline anisotropy constant. The factor 2 is due to appearance of two surfaces. As explained above the origin of the surface anisotropy lies in the symmetry restrictions at the surface of the crystal according to Néel model [29]. Plotting the thickness dependence of $K_\mathrm{1,eff} \cdot t$ diagram allows to determine $K_\mathrm{1V,eff}$ as the slope of the resulting line and $2K_\mathrm{s}$ as the intercept on y-axis.The structural studies on Ni/Pt and Co/Pd (only for $t_\mathrm{Co} > 2\,\mathrm{nm}$) layered structure show that these systems perform out-of-plane fcc(111)-textured behavior and can be regarded as a uniaxial polycrystalline with easy inplane-axis and perpendicular hard-axis (see chapter 4 and 5). Therefore, the volume anisotropy term contains uniaxial magnetocrystalline anisotropy and shape anisotropy as

$$K_\mathrm{1,eff} \cdot t = \left(K_\mathrm{1V} - \frac{\mu_0}{2} M_\mathrm{s}^2\right) \cdot t + 2K_\mathrm{s} \tag{2.14}$$

The linear dependence of $K_{1,\mathrm{eff}} \cdot t$ as a function of Ni or Co thickness is observed as predicted by the model and will be discussed in chapter 4 and 5, respectively. In principle, the negative slope is due to the stronger shape anisotropy in these systems.

2.1.5 Zeeman energy

Until now, we have considered all energy contributions in magnetic materials without applying an external field. In a uniform external field ($\mu_0 \mathbf{H} \neq 0$), the interaction energy of the magnetization and the field is simply given by

$$E_{\mathrm{Z}}/V = -\mu_0 \mathbf{M} \cdot \mathbf{H}_{\mathrm{ex}} = -\mu_0 M_{\mathrm{S}} H \ \cos\Phi \tag{2.15}$$

where Φ is the angle between $\mathbf{M}$ and $\mathbf{H}$. This energy term is referred to as Zeeman energy.

2.2 Galvanomagnetic effects

In this section first of all the basics of electronic transport will be briefly reviewed. In addition, some important magnetoresistance effects related to my work are described subsequently.

In a macroscopic point of view, when an electric field $\mathbf{E}$ is applied in a metal, a current density $\mathbf{j}$ flows in the material as

$$\mathbf{j} = \overleftrightarrow{\sigma} \cdot \mathbf{E} \tag{2.16}$$

where $\overleftrightarrow{\sigma}$ is called the electrical conductivity and is a tensor of second rank which depends on temperature. Equation 2.16 is usually called Ohm's law and also can be written as

$$\mathbf{E} = \overleftrightarrow{\rho} \cdot \mathbf{j} \tag{2.17}$$

where $\overleftrightarrow{\rho} \equiv \dfrac{1}{\overleftrightarrow{\sigma}}$ is the resistivity tensor and depends on the magnetic field. In about 1900, Drude described metallic conductivity using the assumption of an ideal electron gas in the solids [40]. Under applying an electric field in a metal, electrons experience a force and accelerate. For an electron emerging from a collision with velocity v_0, the velocity after time t is given by $v = v_0 - \frac{eEt}{m}$. Because of randomly scattering of the electrons after collision, v_0 will be zero. By considering the time $t = \tau$, the drift velocity is given by $\mathbf{v}_{\mathrm{d}} = -e\mathbf{E}\tau/m^*$ based on Newton's second law, while τ is the relaxation time that electrons can travel without any scattering event and m^* is the effective mass of the charge carriers. Consequently, the Drude relation will be obtained by

$$\mathbf{j} = \frac{ne^2\tau}{m^*}\,\mathbf{E} \quad \Rightarrow \quad \frac{1}{\rho} = \frac{ne^2\tau}{m^*} \tag{2.18}$$

where $\lambda = v_F\tau$ is the mean free path with Fermi velocity $v_F = \frac{\hbar k_F}{m^*}$, and $n = \frac{k_F^3}{3\pi^2}$ is the electron density. Therefore, the Drude relation can be written as

$$(\lambda \cdot \rho)^{-1} = \left(\frac{8\pi}{3}\right)^{1/3} \frac{e^2}{h}\, n^{2/3} \tag{2.19}$$

As the effective mass is proportional to band curvature ($m^* = \hbar^2(\partial^2 E(k)/\partial k^2)^{-1}$), noble metals with a half-filled s-band have the e^- of low effective mass and hence, they exhibit high mobility and low resistivity (e.g. copper).

Temperature dependence of resistivity

Here, in this study, I have investigated the resistivity of Ni/Pt sandwiches, influenced by temperature (Sec. 4.8). Therefore, in this section I describe the sources of temperature dependence of electrical resistance in materials, briefly. Generally, the temperature dependence of ferromagnetic metals arises from residual resistivity ρ_{st}, lattice resistivity ρ_{ph}, and magnetic resistivity ρ_{mag}, as

$$\rho_{\mathrm{tot}}(T) = \rho_{\mathrm{st}} + \rho_{\mathrm{ph}}(T) + \rho_{\mathrm{mag}}(T) + \cdots \tag{2.20}$$

where ρ_{st} comes from impurities and defects at $T = 0\,\mathrm{K}$; ρ_{ph} and ρ_{mag} represent the temperature-dependent resistivities, which are caused by the scattering of the electrons at phonons and magnons. Eq. 2.20 is a representation of Matthiessen's rule, which states that the resistivity of a material can be calculated from the sum of the resistivities of the individual scattering processes. Fig. 2.4(a) indicates the source of resistivity in Ni vs temperature.

According to Matthiessen's rule, it is possible to disentangle the static scattering process from the temperature-dependent processes. It is mentioned that the temperature dependence of resistivity is related directly to the phonon concentration. For temperature above Debye temperature, there is a linear dependency between resisitivity and temperature, while at $T < \Theta_{\mathrm{D}}$ the phonon concentration is proportional to T^5. Therefore, the so-called Bloch-Grüneisen formula describes the temperature dependence of resistivity within the whole span of temperature [41, 42]

$$\rho_{\mathrm{ph}}(T) = A_{\text{el-ph}} \left(\frac{T}{\Theta_D}\right)^n \int_0^{\Theta_D/T} \frac{x^n}{(e^x - 1)(1 - e^{-x})} dx \tag{2.21}$$

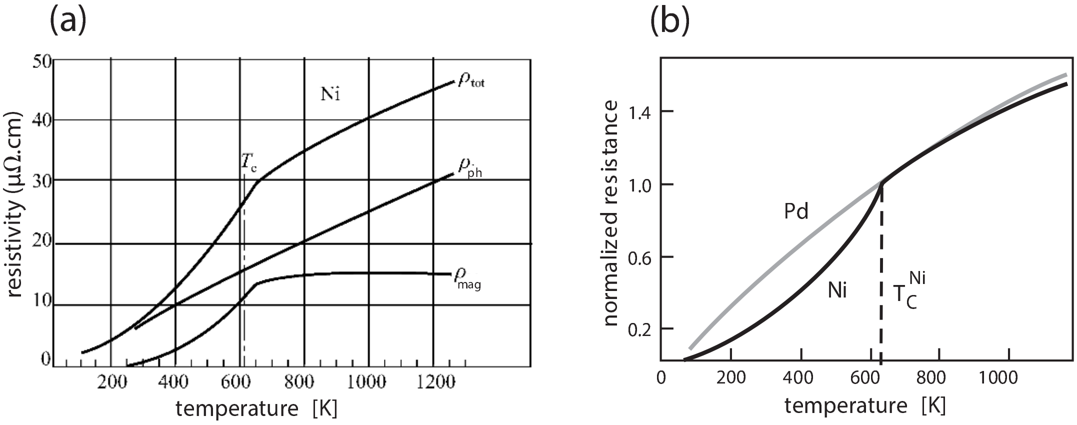

Figure 2.4: (a) Different sources of resistivity of Ni and their relation to the temperature, while lattice resistivity ρ_{ph} increases with temperature, magnetic resistivity ρ_{mag} approaches a temperature-independent saturated value when $T > T_c$ [44]. (b) Temperature dependence of the resistivities of Ni and Pd. Below the Curie temperature, Ni shows anisotropic behavior due to magnetic scattering [25, 45].

where $A_{\mathrm{el-ph}}$ is a material constant proportional to the electron-phonon coupling constant, the Debye frequency, and the plasma frequency. Θ_D is the Debye temperature, while the constant n generally takes the values 2, 3 and 5 depending on the nature of interaction. For simple metals $n = 5$ implies that the resistance is due to scattering of electrons by phonons [43].

Fig. 2.4(b) compares the resistance of a non-magnetic transition metal (Pd) with the total resistance of Ni, extracted from Fig. 2.4(a). Both Ni and Pd are valence isoelectronic and have ten electrons outside the noble gas shell. Therefore, their electronic structures are quite similar. Ni exhibit a reduced resistance below the Curie temperature which is due to appearance of spontaneous magnetization. This occurrence in ferromagnetic elements is a result of an exchange splitting of d-states (see Fig. 2.5(a)). Mott explained this phenomenon with $s-d$ scattering model [46]. In the following a descriptive explanation of the model is given.

Mott $s-d$ scattering model

As explained in Ref. [1, 47], the resistivity of transition metals is higher than simple metals like Al. The explanation of the phenomenon was given by Mott, namely, $s-d$ scattering model. In *transition metals*, the Fermi level is located in the middle of d-band, therefore, the density of states at the Fermi level is higher than for metals, where $s-$ and $p-$states exist at E_F. Moreover, the scattering probability of the conduction electrons is proportional to the density of states at the Fermi level. Consequently, the higher density of states at the Fermi level would result the higher resistivity in transition metals.

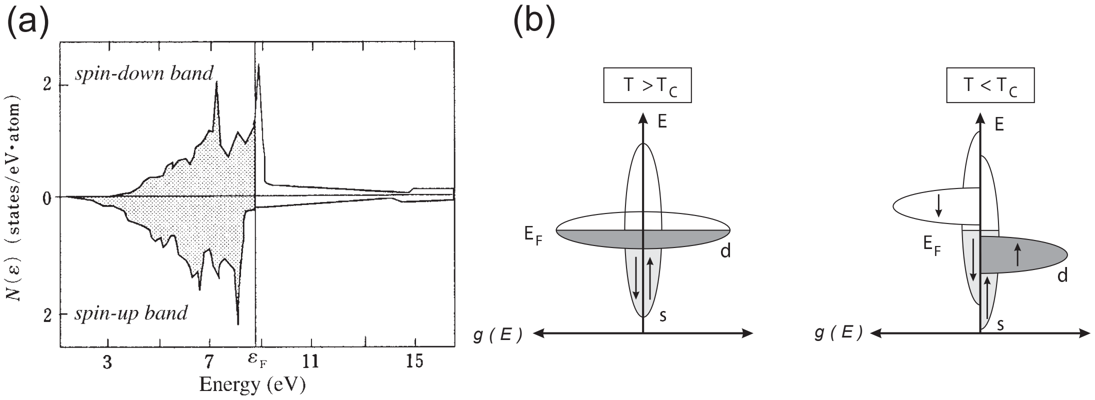

Figure 2.5: (a) Density of state in valence band for pure Ni at room temperature. There is a shift between spin-up and spin-down bands due to exchange interaction. (b) A comparative illustration for density of states between a paramagnetic and a ferromagnetic material.

In *ferromagnetic transition metals*, the spin-up band is displaced to higher energies relative to the spin-down band due to exchange energy as mentioned above (see Fig. 2.5(b)). According to Mott $s-d$ scattering model, at low temperature, during scattering, the spin-orientation of conduction electrons must be unchanged. It means that spin-up electrons can not make transitions to the spin-up d-band because it is full (see Fig. 2.5(b) right). Therefore, spin-up electrons acquire a longer mean free path comparing to spin-down electrons resulting the lowering of the resistivity in the ferromagnetic materials like Ni. On the other hand, above the Curie temperature, both spin-up and spin-down electrons participate equally in $s-d$ transition, since ferromagnetic material becomes paramagnetic [47] (see Fig. 2.5(b) left).

Magnetoresistance (MR) is a term widely used which deals with the change in resistivity of material when subjected to a magnetic field. The first magnetoresistive effect was discovered by Lord Kelvin in 1856 [48]. Up to now several types of MR effects are introduced and found their ways to industrial applications.
In the following, some of the most important types of magnetoresistance like ordinary magnetoresistance (OMR), anisotropic magnetoresistance (AMR), anisotropic interface magnetoresistance (AIMR), spin-disorder magnetoresistance (SMR), and Hall effect are reviewed.

2.2.1 Ordinary Magnetoresistance

Almost all of the conductive materials show normal or ordinary magnetoresistance (OMR) effect. When both a magnetic field and an electric field are applied to a conductor, electrons follow cyclic motions around magnetic field due to Lorenz force and do not contribute to the current density until they are scattered. Thus, the effective mean free path λ (the component of the mean free path along the direction

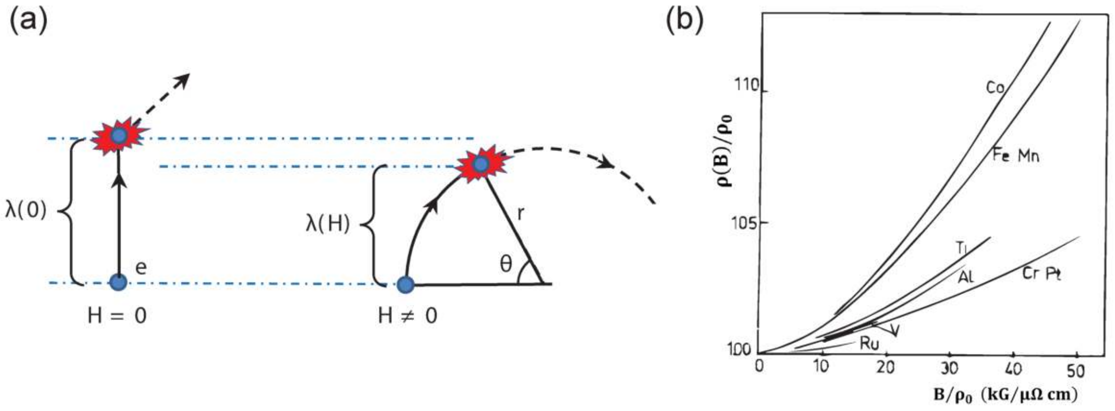

Figure 2.6: (a) Schematic illustration of comparing mean free path in magnetoresistance mechanism at H = 0 and H ≠ 0. Note that the component of mean free path along the applied electric field is smaller in non-zero field (from Ref. [20]). (b) Quadratic behavior of transverse magnetoresistance in Ni containing impurities (Co, Fe, Mn, Ti, …) according to Kohler's rule [49].

of applied electric field) is reduced comparing to zero magnetic field situation (See Fig. 2.6(a)). Since mean free path is proportional to relaxation time ($\lambda = v_F\tau$) and according to Eq. 2.18, the resistivity is increased, so that the corresponding effect is called positive magnetoresistance or OMR ($R(H) > R(H = 0)$) [20]. Kohler was the first who described OMR analytically by

$$\frac{\Delta\rho}{\rho_0} = f\left(\frac{H}{\rho_0}\right) \propto H^2 \tag{2.22}$$

where f is a function that depends on the direction of the current with respect to magnetic field and crystalline axes. Fig. 2.6(b) represents the quadratic behavior of Kohler's rule in Ni-based alloys [49, 50]. In contrast, it is more difficult to express Fe-based alloys in form of Kohler's rule while a linear extrapolation is a better fit [51].

2.2.2 Anisotropic Magnetoresistance

The anisotropic magnetoresistance effect (AMR) is a phenomenon in ferromagnetic materials in which the resistivity depends on the orientation of the magnetization with respect to the direction of the electric current.

It was 1857 that W. Thompson discovered the change in the resistivity of nickel-iron alloys based on relative directions of magnetization and current [48]. It is well known that the effect results from anisotropic scattering of the charge carriers by spin-orbit coupling as suggested by Smit [53] and is a fairly small effect. The largest value of AMR at room temperature so far reported in the literature is 6.5% for the $Ni_{70}Co_{30}$ alloy, which increases to 10% at 77 K [47, 54], therefore, it was used as a reading head in HDD in the late 80's improving the storage density [25, 47].

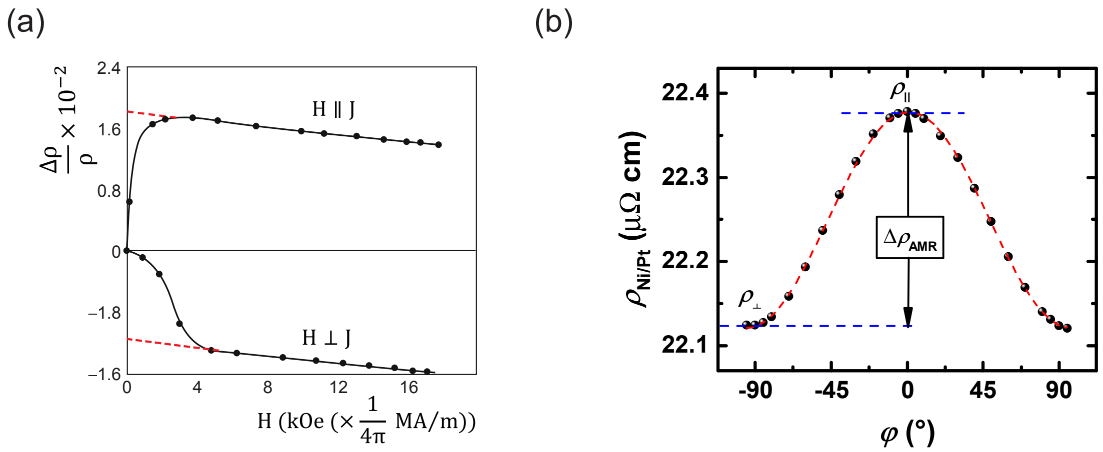

Figure 2.7: (a) Resistivity as a function of an external magnetic field for Ni [52]. (b) Angular dependence of AMR for Pt(5 nm)/Ni(9 nm)/Pt(3 nm) sandwich, measured at constant field of 6 T. The dashed line is a fit according to Eq. 2.23.

Normally the resistivity of a ferromagnet is maximum (minimum) when the current is parallel (perpendicular) to the magnetization direction $\rho_\parallel$ ($\rho_\perp$). Fig. 2.7(a) exhibits the result of AMR obtained for Ni in two geometries, namely, when a magnetic field is applied parallel ($\rho_\parallel$) and perpendicular ($\rho_\perp$) to the direction of the current. At H = 0 there is no difference between two geometries. After applying a magnetic field $\rho_\parallel$ ($\rho_\perp$) increases (decreases) to a maximum (minimum) point which is called $\mathrm{H_c}$ due to a complete reorientation of magnetization along the field. Above $\mathrm{H_c}$, in both geometries ρ decreases monotonically due to spin-disorder MR which is the topic of Sec. 2.2.6. To obtain the strength of AMR effect, both measured curves are extrapolated to zero field as shown by red dashed line in Fig. 2.7(a).

The angular dependence of AMR can be described phenomenologically by a $\cos^2$ behavior

$$\rho_{\mathrm{AMR}}(\varphi) = \rho_\perp + \underbrace{(\rho_\parallel - \rho_\perp)}_{\Delta\rho_{\mathrm{AMR}}} \cos^2\varphi \tag{2.23}$$

where φ is the angle between **M** and **J**. Fig. 2.7(b) shows, as an example, dependence of AMR on the angle between the current direction and the magnetization for Pt(5 nm)/Ni(9 nm)/Pt(3 nm) sandwich, measured at constant external field of 6 T. It is seen that the resistivity is highest (lowest) when the magnetization is parallel (perpendicular) to the direction of current density.

The result of thickness dependence of AMR for Ni/Pt sandwiches is discussed in chapter 4.

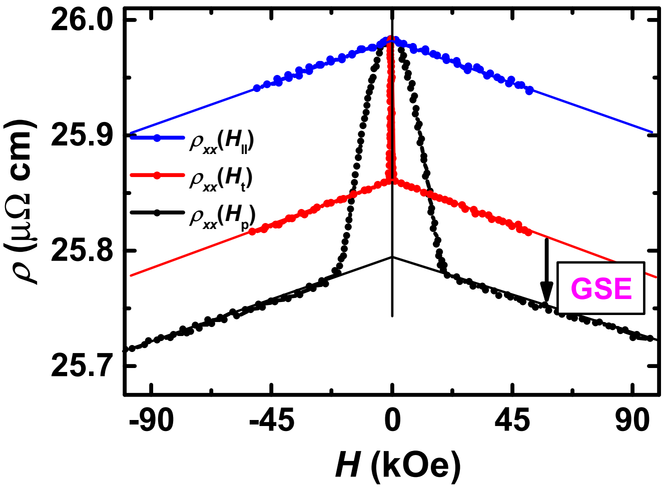

Figure 2.8: Resistivity of 20 nm Co film at room temperature for the three principal directions of the field. $\rho_\mathrm{p} < \rho_\mathrm{t}$ is attributed to the GSE effect which is due to texture of the film. The data are taken from Ref. [55].

2.2.3 Geometrical Size Effect

Generally when the mean free path in the bulk material is comparable to the dimension of the sample, i.e., thin films or wires, there is always extra scattering of electrons by the surface and interfaces, which results in enhancement of the resistivity. Such a specimen is supposed to exhibit a finite size effect.

In 1971, Chen et al. [56] reported for the first time, a size effect while measuring transport properties in polycrystalline and single-crystal Ni thin films in the temperature range of 4 K up to room temperature. They found that the resistivity is smaller when the magnetization oriented along the film normal (polar geometry, ρ_p) than the magnetization directed in the film plane but perpendicular to the current (transverse geometry ρ_t): $\rho_\mathrm{p} < \rho_\mathrm{t}$. It has to be mentioned that in both geometries the magnetization orientation is perpendicular to the current direction. Moreover, when the magnetization is rotated around the current, resistivity showed a similar angle-dependence behavior to the AMR

$$\rho(\theta) = \rho_\mathrm{t} + \underbrace{(\rho_\mathrm{p} - \rho_\mathrm{t})}_{\Delta\rho_\mathrm{GSE}} \cos^2\theta \tag{2.24}$$

with the difference that in this case θ is the angle between magnetization and the film normal. The authors could not explain the effect with the previous theoretical models because of the lack of thickness variation investigation. Therefore the effect was called as Geometrical Size Effect (GSE), which is a misleading interpretation.

Afterwards, Rijks et al. [57] carried out a systematic study of resistivity in both textured and untextured polycrystalline permalloy thin films, with the magnetization vector rotating in the film plane as well as out of the film plane. They found that the op-ratio is considerably larger than ip-ratio, which depends strongly on the degree of texture.

In order to find the relation between GSE and texture of the film, Gil and coworkers [55] have investigated the magnetoresistance of 10 - 200 nm thin polycrystalline Co films in the three principal directions with respect to the current. Similar to the previous studies, they observed that the resisitivity in polar geometry is up to twice larger than transverse field. They explained the effect with an anisotropic effect of the spin-orbit interaction on the $s-d$ scattering of the minority spins due to a film texture, based on Potter's theory [58]. It is shown, additionally, that the size of GSE is independent of temperature. Fig 2.8 from Ref. [55], shows as an example, the GSE effect in 20 nm pure Co at room temperature: $\rho_\mathrm{p} < \rho_\mathrm{t}$.

2.2.4 Anisotropic interface magnetoresistance

Anisotropic Interface magnetoresistance is another effect which is reported in magnetotransport properties of ferromagnets with reduced dimension. It was observed by A. Kobs that the resistivity of Pt/Co/Pt structure depends on magnetization orientation when it rotates in the plane perpendicular to the current direction [10]. Due to the AIMR the resistivity is lower for the magnetization **M** oriented within the film plane (transverse resistivity ρ_t) than for **M** oriented out of plane (polar resistivity ρ_p). This is opposite to the so called geometrical size effect (GSE), explained above, which is a consequence of the texture of the films.

On the other hand, by studying the angular dependence of the resistivity, a $\cos^2$ behavior was obtained for AIMR, similar to the AMR effect, and given by

$$\rho_\mathrm{AIMR}(\theta) = \rho_\mathrm{t} + \underbrace{(\rho_\mathrm{p} - \rho_\mathrm{t})}_{\Delta\rho_\mathrm{AIMR}} \cos^2\theta \tag{2.25}$$

where θ is defined as the angle between magnetization and the film normal. It has to be mentioned that in AIMR the magnetization is always perpendicular to the current, therefore, the AMR can be excluded as a cause for this behavior.

By investigating the thickness dependence of AIMR ratio, a $\Delta\rho_\mathrm{AIMR} \propto 1/t_\mathrm{Co}$ behavior was found for Co/Pt sandwiches revealing the presence of an anisotropic magnetic scattering mechanism of electrons at the interface. Therefore the effect named as Anisotropic Interface Magnetoresistance (AIMR). The AIMR effect could be qualitatively modeled in a fully relativistic description of the magnetotransport where the spin orbit interaction is inherently included [59].

So far, the AIMR effect was observed also in Py/Pt and Co/Pd layered structures experimentally [60, 61].

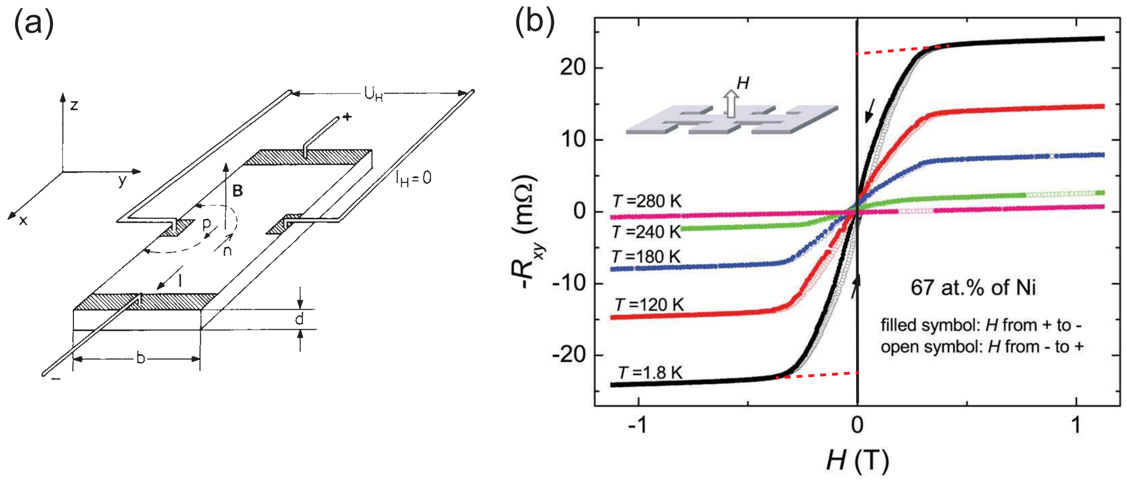

Figure 2.9: (a) The geometry of Hall effect experiment. The current is driven through the slab in x direction and magnetic field is applied in z direction, while U_H is measured from the sides as shown in the sketch [28]. (b) Hall resistance in dependence of magnetic field for difference temperature for $\mathrm{Ni}_{67}\mathrm{Pt}_{33}$ alloys [70].

2.2.5 Normal and Anomalous Hall effect

Nearly 18 years before the discovery of the electron, Edwin Hall observed an effect, that now bears his name and opened a new field in physics and became a source of many future achievements [62].

The geometry of the Hall effect can be understood from Fig. 2.9(a). When an external magnetic field $\mu_0 H$ is applied perpendicular to a conducting material with a current flowing in x direction, the charge carrier will be deflected to the sideways due to the Lorenz force. The buildup of charge carriers at the sides of the conductors will balance the magnetic influence, producing a measurable voltage between the two sides of the conductor. This measurable transverse voltage is given by

$$U_H = -\frac{1}{n_\mathrm{e} e}\frac{I_x \mu_0 H_z}{t} = R_0 \frac{I_x \mu_0 H_z}{t} \tag{2.26}$$

where n_e is the charge carrier density, $R_0 = (n_e e)^{-1}$ is called ordinary Hall coefficient, and t is the sample thickness. For polycrystalline Ni film the values $-R_0^{\mathrm{Ni}} = 5.9\text{-}6.1 \times 10^{-11}\ \mathrm{m}^3/\mathrm{C}$ were reported in literature at room temperature [63–66], whereas for polycrystalline Pt was found smaller: $-R_0^{\mathrm{Pt}} = 1.5\text{-}2.4 \times 10^{-11}\ \mathrm{m}^3/\mathrm{C}$ [67–69].

The anomalous Hall effect (AHE) is another transport phenomena in magnetic materials. In 1981, it was discovered by E. Hall that in ferromagnets the resistivity of the sample in the direction perpendicular to current and magnetic field acquires an additional contribution due to the magnetization of the sample [71]:

$$U_H = (R_0 H_z + R_S M_z)\frac{\mu_0 I_x}{t} \tag{2.27}$$

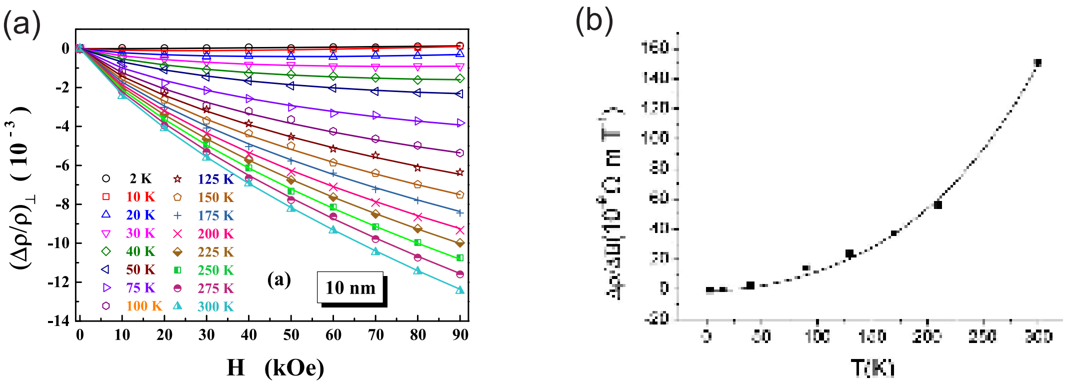

Figure 2.10: (a) The transverse magnetoresistance of 10 nm Ni sample measured at temperature ranging from 2 K to 300 K. At high field the resistivity decreases monotonically with applied field [74]. (b) Temperature dependence of MR slope of 32 nm FePt system. The solid line is the fit according to Eq. 2.31 [75].

while R_S is the anomalous Hall coefficient. R_S is associated with a break of right-left symmetry during spin-orbit scattering in magnetic materials and can be much larger than R_0. It has been established that there is a direct correlation between R_S and longitudinal resistivity as

$$R_S \propto \rho^n \tag{2.28}$$

where n depends on the predominant scattering mechanism: $n = 1$ for skew scattering and $n = 2$ for side jump. Superposition of two effects is usually presented as

$$R_S = a\rho + b\rho^2 \tag{2.29}$$

where a and b are coefficients corresponding to the skew scattering and side jump, respectively. It is assumed that in low-resistivity systems, the dominant mechanism is skew scattering, while it is claimed that in ferromagnets with relatively high resistivity the side jump mechanism is the dominant one [72]. R_S is measured and reported at 300 K for pure Ni in literature as: $-R_S^{\mathrm{Ni}} = 7.9\text{-}12.3 \times 10^{-9}\,\mathrm{m}^3/\mathrm{C}$ [64, 67, 73].
Fig. 2.9(b) shows the dependence of Hall resistance in NiPt with 67% Ni constant at different temperatures [70]. According to their study, dR_{xy}/dH at low fields decreases with increasing temperature.

2.2.6 Spin-disorder Magnetoresistance

The contribution of magnon scattering to the electrical resistivity which provides a linear dependence of the resistance on the applied field can be regarded as spin-disorder magnetoresistance (SMR). In 2002, Raquet et al. showed for 3*d*-metal thin films that the magnon-electron interactions are the source of a linear dependence of the resistivity on an applied field [76]. In high field region which is enough to saturate the magnetization, because of annihilation of magnons the magnetization enhances with the field. As a result of decreasing electron-magnon scattering the resistivity of the system decreases with the field.

Moreover, a temperature dependence of resistivity at high field is proposed by Raquet et al. as

$$\Delta\rho(T,H) \approx \rho(T,H) - \rho(T,0) \propto \frac{\mu_0 HT}{D(T)^2} \ln\left(\frac{\mu_B \mu_0 H}{k_B T}\right) \tag{2.30}$$

where D is the exchange stiffness and from the derivation of this expression, the temperature dependence of the MR slope results as

$$-\left|\frac{\mathrm{d}\rho_{\mathrm{mag}}}{\mathrm{d}H}\right| \propto T(1+2d_1T^2)\ln\frac{T}{T_0} \tag{2.31}$$

where T_0 is a temperature-independent term and d_1 presents the temperature dependent change in the magnonic mass. More details about temperature dependence of resistivity can be found in Ref. [11, 76, 77].

Fig 2.10(a) shows the linear dependence of resistivity for Ni samples at temperature ranging 2 K to 300 K measured by Madduri et al. [74]. According to Eq. 2.31, Mihai et al. measured the MR slope of 32 nm FePt sample vs temperature shown in Fig. 2.10(b) [75].

In chapter 4, the thickness dependence of SMR effect of Ni/Pt systems is presented.

Chapter 3

Sample preparation and experimental setup

The main focus of this work is on magnetotransport properties of Ni/Pt and Co/Pd thin films that are discussed in details in following chapters. Before going through the results, I prefer to describe briefly in this chapter the sample preparation process and the experimental setup have been used within this work. Accordingly, the first section of this chapter outlines methods utilized for sample preparation, namely direct current (DC) magnetron and electron-cyclotron resonance (ECR) sputtering deposition, as well as a short presentation of our preparation chamber. In section 3.2 the experimental setup used for magnetoresistance measurements of the samples will be shortly reviewed. The chapter will be closed by introducing the techniques used to investigate the structural properties of Ni/Pt and Co/Pd layered structures.

3.1 Sample preparation

There are many different ways to deposit materials such as metals, ceramics, and plastics onto a surface (substrate) to form a thin film. Among these techniques, *sputtering* has become one of the most common ways to fabricate thin films.

It was discovered over a hundred years ago and was first reported by Grove [78] in 1852 and independently by Plücker [79] in 1858. As long ago as 1877, sputtering was used to coat mirrors [80].

Sputtering is the ejection of atoms by the bombardment of a solid or liquid target by energetic particles, mostly ions. It results from collisions between the incident energetic particles, and/or resultant recoil atoms, with surface atoms (see Fig. 3.1). The most commonly used incident species are inert gas ions (e.g. Ar^+, Kr^+, Xe^+), but sputtering can also result from the bombardment of other energetic ions, neutrals, electrons and even photons. The ejected atoms then travel some distance until they reach the substrate and start to condense into a film. As more and more atoms reach on the substrate, they begin to bind to each other and forming an atomic layer. One or more layers of such atoms can be created depending on the sputtering time.

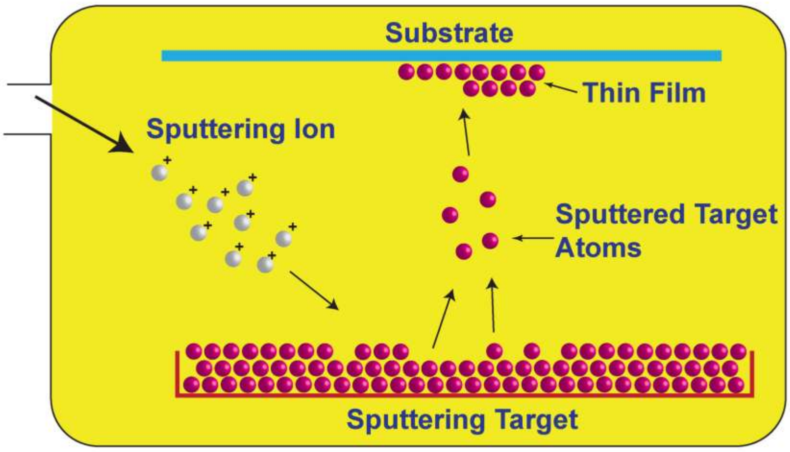

Figure 3.1: A simple illustration of scattering process. In a UHV chamber the sputtering ions (created in a procedure explained below) hit the target atoms and eject them to the substrate.

Besides, the structure of the deposited material can be modified by deposition rate, the substrate temperature, and so on (working pressure, energy of ions, element of ions$\cdots$) [81].

The basic principle explained above can be applied to all types of sputtering deposition methods. In the following only the two sputtering techniques that were utilized in fabricating my samples will be introduced in detail.

3.1.1 Direct current (DC) magnetron sputtering deposition

Magnetron sputtering falls to a group of Physical Vapor Deposition (PVD) techniques, which is utilized for the deposition of a wide range of industrially important coatings [82, 83].

The basic process is as follows. Electrically neutral Ar atoms are introduced into a vacuum chamber. A magnetic field is created via a permanent magnet in front of the target. As a result, the electrons are forced to travel in a spiral way and increase the probability of further ionizing Ar atoms. This tends to generate a stable plasma with high density of ions. By applying a voltage to the target, the Ar^{+}-ions are accelerated away from the target as it is negatively charged. The higher ejection rate, and hence deposition rate, minimizes impurities to form in the thin film, and the increased distance between the plasma and substrate minimizes damage caused by stray electrons and Ar ions. More details about Magnetron sputtering can be found in Ref. [84, 85].

3.1.2 Electron-cyclotron resonance (ECR) sputtering deposition

Electron-cyclotron resonance (ECR) plasma, belongs to the group of Chemical Vapor Deposition (CVD), has been widely used for film deposition [82]. The main points of ECR technique is similar to the magnetron sputtering method. Here, microwaves, which are created by a magnetron, are introduced to the plasma chamber through an antenna. Ar gas is inserted to the chamber. There are permanents magnets in the chamber in order to force electrons to move in circular motion with resonance frequency (the electrons were created by the collision of Ar gas atoms). Once the input microwave frequency matches to the electron cyclotron frequency (ECR condition), the energy of the wave is transferred to the electrons and generates more ionized atoms. The ionized atoms are accelerated with high voltage from the plasma chamber to the target, which is placed face to face to the substrate. Consequently, the target is bombarded by the accelerated ions and causes releasing the target material. One of the advantages of this method is that the working pressure in the UHV chamber is low due to the creation of plasma in a separate chamber (with much higher pressure). More details about ECR can be found in Ref. [86–90] and references therein.

3.1.3 Preparation of Ni/Pt and Co/Pd samples in sputter chamber

In order to investigate the magnetoresistance properties of ferromagnetic thin films, a series of Pt/Ni/Pt samples with different thicknesses of Ni were prepared in our preparation chamber. Furthermore, we have fabricated a series of Pd/Co/Pd samples with varying Co thickness to investigate the influence of aging on the structure and magnetotransport properties.

Fig. 3.2(a) shows the exterior view of our UHV preparation chamber which is base on sputtering deposition as mentioned before with pressure less than 2×10^{-9} mbar. The chamber is equipped with both magnetron and ECR sputtering devices and both processes were combined in the growth of Ni/Pt films. According to the result of Stillrich et al. [91], the perpendicular magnetic anisotropy of Co/Pt layered structures enhances when the seed layer is first deposited by ECR and then is covered by 1 nm magnetron sputtering technique. He explained that the intermixing of the material at the interfaces reduces due to the lower ion energy in the case of magnetron sputtering and provides a smoother surface. Moreover, ECR sputter deposition on substrate results textured films with rather rough interfaces.

Fig. 3.2(b) shows the schematic construction of the samples. Si_3N_4 was used as a substrate with 200 nm thickness to grow the layers on top. As a seed layer 4 nm Pt were deposited with ECR technique. The Ar working pressure for deposition was 5×10^{-4} mbar and the deposition rate of Pt was about 0.08 nm/s, which was calibrated by x-ray reflectometry. As explained above, the growth procedure was

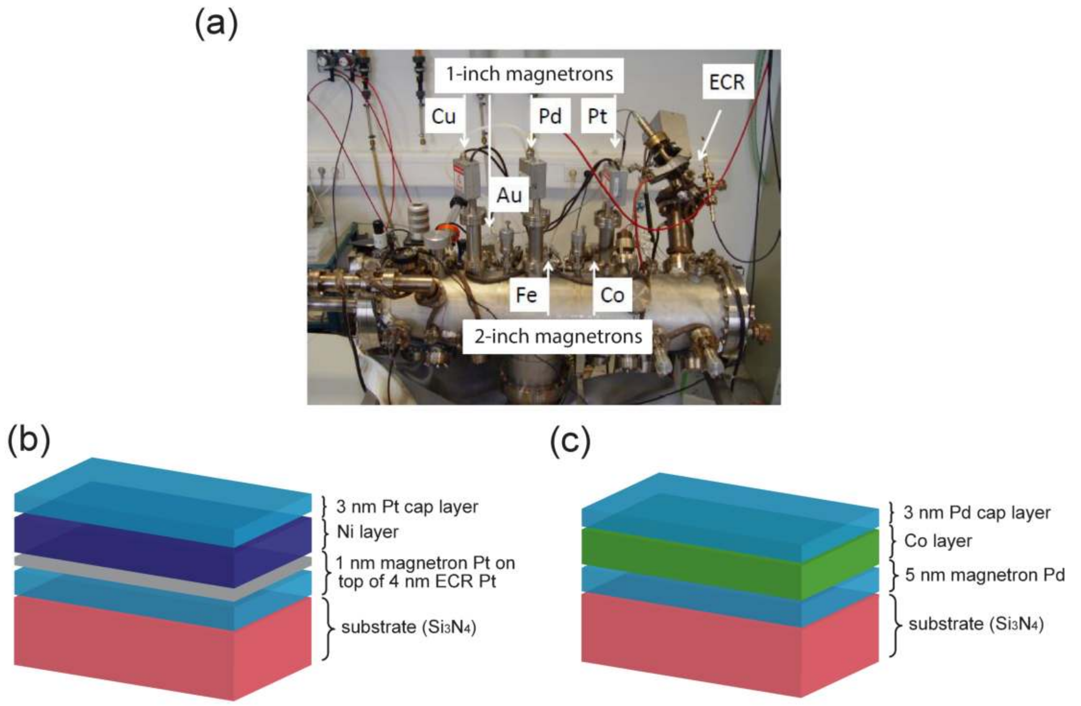

Figure 3.2: (a) A photograph of preparation chamber which has been used to prepare Pd/Co/Pd layer structures. The ECR is equipped with a Pt target. 2-inch targets are used for the ferromagnetic elements (Co, Fe), while 1-inch targets are used for non-ferromagnetic elements (Pt, Pd, Cu, Au) [77]. In order to prepare Pt/Ni/Pt samples one of the ferromagnetic targets is replaced with Ni-target. A schematic view of (a) Ni/Pt and (b) Co/Pd samples construction. The thickness of Ni varies from 1 to 50 nm, while there are only two Co/Pd samples with 2 and 7 nm Co thicknesses.

combined with magnetron sputter deposition. Hence, all the rest layers were created by magnetron sputtering, which consists of 1 nm Pt, Ni layer with various thicknesses from 1 to 50 nm, and 3 nm Pt as a cap layer to protect Ni from contamination. The magnetron chamber is equipped with different magnetron targets like Pt, Ni, Co, and Pd. Besides, the voltage applied between cathode and anode is varied from 250 to 600 V and the current flow is kept constant for each deposition layer.

Tow Pd/Co/Pd samples were fabricated with DC magnetron sputtering deposition, namely 5 nm Pd as a seed layer and 3 nm Pd as a cap layer. One of the samples has 2 nm and the other 7 nm Co in between (see Fig. 3.2(c)).

In the following the experimental setup used to measure magnetoresistance properties of the samples at room temperature as well as low temperatures will be reviewed.

3.2 Magnetoresistance measurements setups

As stated before, the main purpose of this work is to investigate the influence of interface in magnetotransport properties of Ni/Pt layered structures. Moreover, the other part of my thesis is allocated to inquire the variation of magnetoresistance

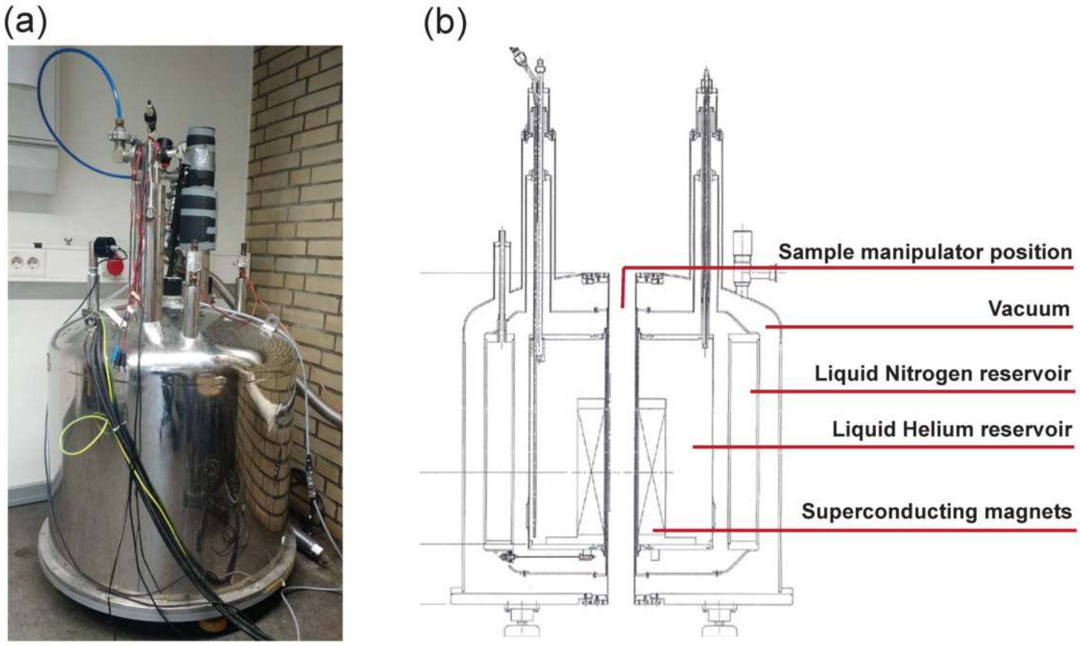

Figure 3.3: (a) A photograph of Warm-bore magnet. (b) A cross-sectional view of the system. The sample manipulator is not shown in the sketch.

properties of Co/Pd thin films through aging. The magnetoresistance measurements through this work were performed by two setups; *Warm-bore magnet* and *Spectromag*, which are explained shortly in the following.

3.2.1 MR measurement setup at room temperature

Fig. 3.3(a) shows a photograph of the experimental setup that was used to measure the MR properties of Pt/Ni/Pt and Pd/Co/Pd sandwiches at room temperature. The system has a superconducting magnet which can provide homogeneous magnetic field up to ±11 T and is called *Warm-bore magnet*[1]. A bore with 6 cm diameter is designed vertically in the middle of cryostat and the magnetic field is produced vertically, too. The magnets were mounted in a liquid helium reservoir surrounded in turn by a liquid nitrogen shield. A vacuum vessel is allocated to isolate the whole system in order to reduce liquid helium consumption (see Fig. 3.3(b)).

The magnetic field can be controlled by the current flow through the superconducting coils.

The sample is positioned in the homogeneous magnetic field utilizing a sample manipulator. With help of the manipulator it is possible to rotate the sample by 180° with a twister wheel assembled on top of it. The sample orientation can be tuned for different rotational planes. In addition to the rotational measurements, the magnetoresistance of the samples have been measured in three generic geometries with field sweep in a range of ±6 T. In this case the field is swept with rate of 0.2 or 0.4 T/min.

---

[1] Oxford instruments B-T environment, project number 37791

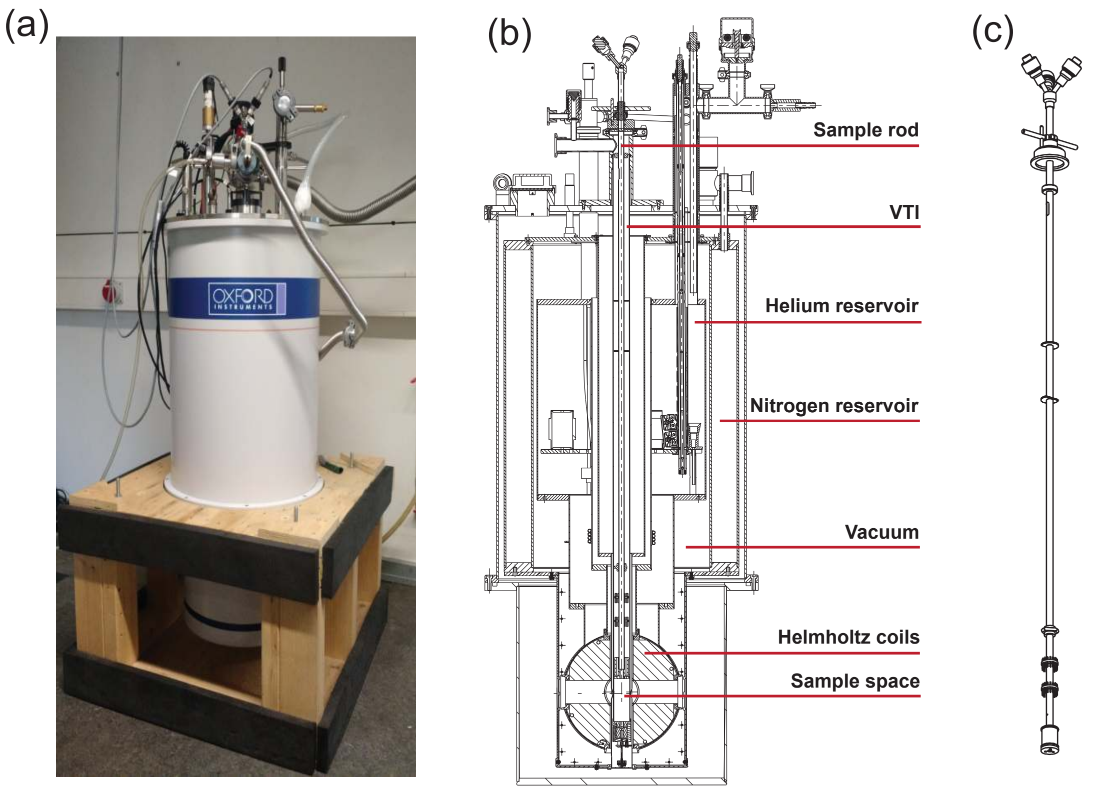

Figure 3.4: (a) Exterior view of Spectromag setup. (b) A cross-sectional view of Spectromag. All important parts are labeled in the sketch. (c) A schematic view of sample rod. The sample is attached to the bottom part with help of sample holder.

Details about the measurement geometries and sample layout are presented in Sec. 4.2.

3.2.2 MR measurement setup with variable temperature

The system that was used to measure the MR properties of the samples at variable temperatures consists of superconducting magnets (Helmholtz coils) that provide homogeneous magnetic field up to ±7 T, horizontally, and is called *Spectromag*[2] (see Fig. 3.4(a)). As shown in Fig. 3.4(b), the spectromag cryostat is shielded with liquid nitrogen reservoir and the coils are situated and welded into a liquid helium reservoir. Both reservoirs are thermally isolated by using materials with low thermal conductivity and also high vacuum chamber with pressure up to 10^{-6} mbar.
A variable temperature insert (VTI) is situated in the middle of cryostat and used to adjust the temperature of the sample from 1.5 to 300 K. This is done by balancing the cooling power of a flow of liquid helium through a needle valve with a heater. The flow can be controlled by an auto needle valve motor while the liquid helium is drawn from the main reservoir. Fig. 3.4(c) shows the sample rod that is designed to bring the sample into the magnetic field and also carry a heater and

---

[2] Oxford instruments, project number 52398

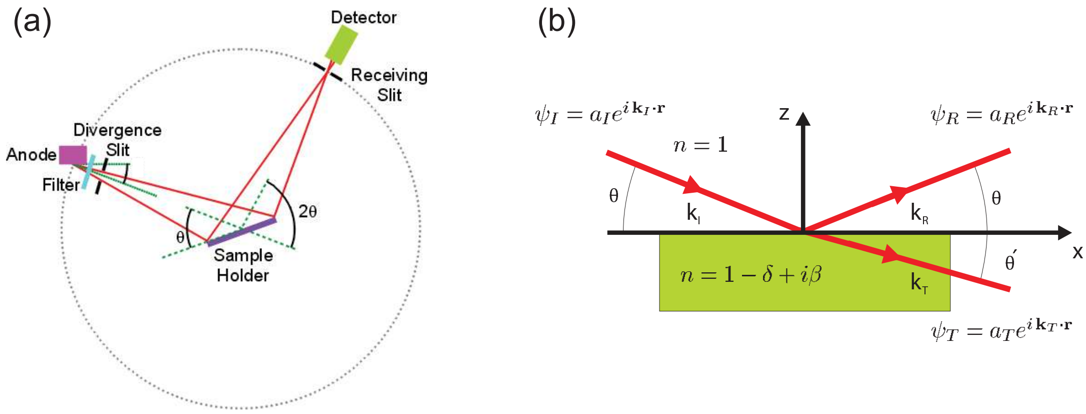

Figure 3.5: (a) A typical setup of XRR experiment. Here Cu is used as anode material, where the Cu Kα line with a wave length of λ =1.5406 Å is utilized. (b) Schematic sketch of refraction and reflection effect occurring at the boundary of two different media that can be described by Snell's law and Fresnel equations.

thermometer. The samples are connected to the end of sample rod with help of two different sample holders which provide the possibility of rotation of the sample in different rotational planes (see Fig. 4.7(d)). Unlike the Warm-bore magnet, here, no mechanical converter is necessary to rotate the sample. As a result, in addition to MR measurements performed by Warmbore setup, the temperature variation of MR measurements can be carried out by Spectromag setup.
A high-precision power supply (IPS)[3] is also designed to produce magnetic field which is proportional to the current flow. The power supply is capable of sourcing and sinking current and it also accurately controls the slew of the current.

3.3 Structure characterization techniques

Since structure and functionality are related properties in any material, the characterization of structural properties is a very relevant issue in thin film investigation. Although there are various technologies for characterization of the magnetic samples, only those concerning x-ray scattering (x-ray reflectivity and x-ray diffraction) as well as transmission electron microscopy were used in this work. There is a number of references dealing with the fundamentals of these experimental techniques, therefore in the following only aspects which are necessary to understand the results will be addressed.

3.3.1 X-ray reflectivity

Since many properties of thin films are thickness dependent, it seems to be essential to determine the thickness of layers with high precision in many technological appli-

---

[3] Oxford instruments

cations. X-ray reflectivity (XRR) is a non-destructive technique which has become a rather common tool in chemistry, physics, and materials science for thickness determination in nanometer range with a precision of a few Å. In addition to thickness determination, this technique is also employed for the determination of density and roughness of films and also multilayers with a high precision.
Fig. 3.5(a) schematically shows a typical experimental setup for reflectivity measurements. This method involves monitoring the intensity of the x-ray beam reflected by a sample at grazing angles. A monochromatic x-ray beam of wavelength λ irradiates a sample at a grazing angle θ and the reflected intensity at an angle θ is recorded by a detector (see Eq. 3.2).
The basic principle of XRR is described as follows. When light changes its direction of propagation at an interface between two materials, it is well known as refraction and reflection effect. The reflection at the surface and interfaces is due to the different electron densities in the different layers (films), which corresponds to different refractive indexes n in the classical optics. For x-ray radiation the complex refraction index of material is slightly less than 1 and given by

$$n = 1 - \delta - i\beta \tag{3.1}$$

Where δ and β represent the dispersion and absorption, respectively. δ is proportional to the product of Thomson scattering length (i.e., the electron radius) and the electron density ρ and it is in the order of 10^{-5}, while β is one order of magnitude smaller [92].
During the transition from a material with refraction index n to another material with refraction index n' the angles of incidence and refraction, respectively, are related through Snell's law

$$n \cos\theta = n' \cos\theta' \tag{3.2}$$

where θ and θ' are measured with respect to the surface (see Fig. 3.5(b)). For incident angles below the critical angle (θ_c), total reflection occurs. By considering cos expansion[4] for $\theta \approx 0$ and set $n = 1$, the critical angle θ_c is given by

$$\theta_c = \sqrt{2\delta} \tag{3.3}$$

The θ_c values can be estimated from the electron densities between 0.1° and 0.4° if Cu Kα is used [93].
For the determination of the reflectivity, a plane x-ray wave at an ideal smooth surface, presented in Fig. 3.5(b), has to be considered. The incident wavevector is $\mathbf{k}_I$, and the amplitude is a_I. Similarly the reflected and the transmitted wavevectors are

---

[4] Cosine expansion $\Rightarrow$ $\cos\theta = 1 - \theta^2/2! + \theta^4/4! - \cdots$

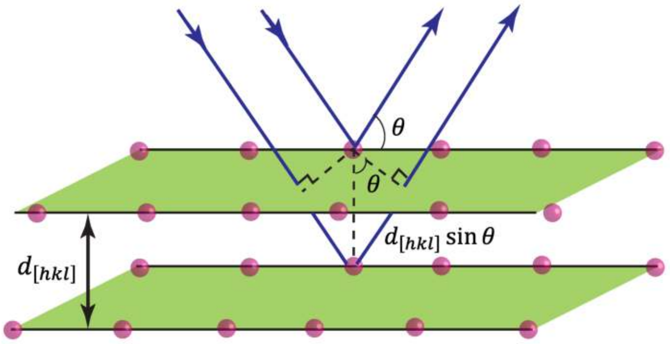

Figure 3.6: Diffraction of x-ray by two atoms in neighboring planes. The path difference is two times $d_{[hkl]} \sin\theta$.

$\mathbf{k}_R$ and $\mathbf{k}_T$, respectively, and the amplitudes are a_R and a_T. Moreover, it is required that the wave and its derivative at the surface and interface are continuous:

$$a_I + a_R = a_T \;\; ; \;\; a_I\mathbf{k}_I + a_R\mathbf{k}_R = a_T\mathbf{k}_T \tag{3.4}$$

From these expressions the Fresnel equations for the reflected and transmitted amplitude are derived as

$$r \equiv \frac{a_R}{a_I} = \frac{\theta - \theta'}{\theta + \theta'} \;\; ; \;\; t \equiv \frac{a_T}{a_I} = \frac{2\theta}{\theta + \theta'} \tag{3.5}$$

Finally the reflected and transmitted intensity can be introduced as

$$R(\theta) = \frac{I_r}{I_i} = |r|^2 \;\; ; \;\; T(\theta) = \frac{I_t}{I_i} = |t|^2 \tag{3.6}$$

As stated above, the incidence angle beyond which total reflection occurs is referred to as the critical angle θ_c and the respective reciprocal lattice vector q_c. Above q_c, due to the interference of x-rays reflected from different interfaces, layers and multilayers on flat substrates give rise to oscillations called Kiessig fringes in the XRR intensity plot [94]. Basically, fringes period depends on layer thickness, while fringes amplitude depends on surface and interface roughness and the relative electron densities of the materials. More details about XRR can be found in Ref. [92, 95, 96] and references therein.

3.3.2 X-ray diffraction

There are multiple X-ray techniques used to study the sample properties, each of which is suitable for different kinds of the structures. Among these methods, x-ray diffraction (XRD) is a powerful and reliable tool in studying a large diversity of micro- and nanoscale objects [96].

Let us consider a crystal which can be described as a lattice of points with translational symmetry as schematically shown in Fig. 3.6. When the incident x-rays are reflected specularly from two neighboring crystal planes with spacing $d_{[hkl]}$ (interplanar spacing), a constructive superposition of the beams occurs whenever the path difference of the reflected beams is an integer of the x-ray wavelength λ. For a given θ (the angle between the incident beam and the surface), the path difference is $2d_{[hkl]}\sin\theta$. This leads to the well known Bragg's law

$$2d_{[hkl]}\sin\theta = n\lambda \tag{3.7}$$

where n is called the order of diffraction and is an integer. From the geometrical point of view, the angle between the diffracted beam and the transmitted beam is always 2θ, which is known as the diffraction angle, and usually measured experimentally.

In order to predict the diffraction direction for any set of planes, the Bragg's law and the interplanar spacing equation (corresponding to the particular crystal) have to be combined. As an example, for a cubic crystal

$$\sin^2\theta = \frac{\lambda^2}{4a^2}(h^2+k^2+l^2) \tag{3.8}$$

where h, k, l are known as Miller indices, a is the edge of the cubic unit cell, and the interplanar spacing equation for a cubic crystal is defined as

$$\frac{1}{d^2} = \frac{h^2+k^2+l^2}{a^2}. \tag{3.9}$$

Therefore, diffraction directions are determined only by the shape and the size of the unit cell [97]. For instance, Ni has a face-centered cubic lattice with $a = 0.352\,\text{nm}$ [98]. In the diffraction pattern no reflections occur for planes with mixed odd and even Miller indices (hkl) like (100), (210), (112), etc. but reflections may appear for planes with solely odd or even Miller indices. The reason behind is explained below. According to equation 3.8 diffracted patterns can be detected for (111) planes at $2\theta = 44.6°$ and for (200) planes at $2\theta = 51.91°$, if λ =1.5406 Å.

Generally, the intensity of a diffracted beam is affected by any change in atomic positions, and hence, atomic positions can be determined by observations of diffracted intensities.

When an x-ray beam encounters an atom, each electron in it scatters part of the radiation coherently in accordance with Thomson's equation. The atomic scattering factor f is a quantity to describe the efficiency of scattering of x-ray at a given atom in a given direction:

$$f = \frac{\text{amplitude of the wave scattered by an atom}}{\text{amplitude of the wave scattered by one electron}} \tag{3.10}$$

Obviously, $f = Z$ for any atom scattered in the forward direction and f decreases with increase in θ. To derive an expression for the intensity of diffracted beam, all the waves scattered by the individual atoms in a unit cell simply have to be added together. The scattering amplitude generated by crystal unit cell is called the structure factor and defined as [97]

$$F_{hkl} = \sum_{1}^{N} f_n e^{2\pi i(hu_n + kv_n + lw_n)} \tag{3.11}$$

where N is the number of atoms and uvw is the coordinate of each atom in a unit cell. The absolute value F, represents the amplitude of the resultant wave in terms of the amplitude of the wave scattered by a single electron.

The intensity of the diffracted beam by all atoms of the unit cell is simply proportional to $|F|^2$, and other factors like Lorentz factor and polarization factor. The intensity of the diffracted beam by the whole crystal can be written as

$$I \propto \frac{VF^2}{V_a^2}\left(\frac{1+\cos^2 2\theta}{2\sin 2\theta}\right) \tag{3.12}$$

where V is the volume of the crystal and V_a is the volume of a unit cell. The trigonometric term presents the Lorenz-polarization factor. More details about the polarization factor can be found in Ref. [93, 97, 99–101] and refrences therein.

As stated above with help of Eq. 3.11, it is possible to predict for which set of planes the diffracted pattern occurs and which one dose not exist. For example, let us consider the structure factor for Ni with fcc lattice. The unit cell of fcc structure contains four atoms, located at (0,0,0), (1/2,1/2,0), (1/2,0,1/2), and (0,1/2,1/2). By substituting these uvw's in 3.11, we have

$$\begin{aligned} F_{fcc} &= fe^{2\pi i(0)} + fe^{2\pi i(h/2+k/2)} + fe^{2\pi i(k/2+l/2)} + fe^{2\pi i(h/2+l/2)} \\ F_{fcc} &= f[1 + e^{\pi i(h+k)} + e^{\pi i(k+l)} + e^{\pi i(h+l)}] \end{aligned}$$

For planes with even or odd Miller indices, the structure factor $F = 4f$, while the forbidden reflections come from mixed (even and odd) Miller indices and clearly $F = 0$. Thus, reflections may occur for such planes as (111), (200), and (220) but not for the planes (100), (210), (112), etc. In the following two chapters the result of XRR and XRD measurements on Pt/Ni/Pt and Pd/Co/Pd will be discussed before representing the magnetotransport findings.

Chapter 4

Investigation of magnetorersistance effects in Pt/Ni/Pt layered structures

The magnetotransport properties of Ni/Pt sandwiches and the causes of the observed effects are discussed in this chapter. First of all, the structural properties of the samples are studied utilizing different techniques such as X-ray reflectivity (XRR), X-ray diffraction (XRD), and high resolution transmission electron microscopy (HRTEM) in order to obtain a proper foundation for the interpretation of the MR effects in Pt/Ni/Pt layered structure (Sec. 4.1). In Sec. 4.2 the geometries of the measurements and the sample layout are introduced. The magnetic anisotropy and the result of thickness dependence of $K_{1,\mathrm{eff}}$ are shown and described in Sec. 4.3.
By studying the magnetoresistance measurements as a function of sweeping magnetic field, it is seen that $\rho_\mathrm{p} < \rho_\mathrm{t}$, which is against the similar result of Co/Pt system. Therefore, the angular dependence of resistivity of Ni/Pt was investigated and led to observation of higher order contributions to the op-AMR effect. This is the main achievement of this work, as it has not been studied or reported in literature so far (sections 4.4 and 4.5).
In sections 4.6 and 4.7, I present the thickness dependence of MR effects consisting of AMR, op-AMR, SMR, and Hall effect constants measured for Ni/Pt system. It has to be mentioned that the results of MR effects in Ni/Pt have been compared step by step with similar Co/Pt structure studied by A. Kobs [10, 11, 102].
Finally, the resistance (resistivity) of Ni/Pt system is investigated in the temperature range of 2 - 300 K.

4.1 Sample characterization

Before introducing the magnetoresistance effects, investigated in Pt/Ni/Pt stacks, I would like to present the structural properties of the samples. As stated in previous chapter, an X-ray diffractometer is used to determine the orientation and also the

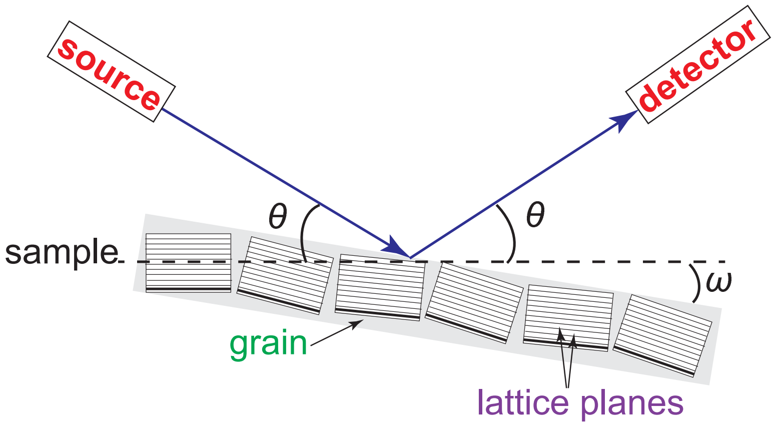

Figure 4.1: Sketch of the XRD measurement. It is possible to varry θ and ω separately in order to fulfill Bragg's law conditions. The figure is obtained from Ref. [11].

structure of crystallites. X-ray reflectivity method is also applied to obtain details about interface roughness and thickness of the layers. To complete the study and for a cross check, Scanning Electron Microscopy (SEM) and Transmission Electron Microscopy (TEM) are used to measure the lateral size of grains and the layers topology. The X-ray measurements have been performed by G. Winkler, and D. Lott in Helmholtz-Zentrum Geesthacht (GZG). The results are discussed in the following sections.

4.1.1 X-ray Diffraction (XRD)

The crystallinity of Ni/Pt samples are analyzed by high angle X-ray diffraction (XRD). Fig. 4.1 shows a schematic sketch of the XRD measurement. In a XRD map a series of θ-measurements are recorded at different ω. It means that for each angle ω, the detector sweeps θ angle and records the intensity which is proportional to the number of X-ray photons of a particular energy. The intensity is expressed in arbitrary units because usually the relative intensities of the peaks are more interesting rather than the absolute intensity. Generally, the recorded diffraction pattern has a background signal, which is subtracted here to obtain smooth peaks.

Fig. 4.2(a) shows a representative diffraction map of Pt/Ni/Pt sandwiches with 50 nm Ni thickness on Si_3N_4 substrate. The pattern consists of two sharp peaks. The intensity is plotted on the ordinate and the measured diffraction angle, 2θ, along the abscissa.

Fig. 4.2(b) displays the integrated intensity $I(2\theta) = \sum_{\omega} I(\omega, 2\theta)$ of the diffraction map shown in Fig. 4.2(a). Two sharp peaks can be seen clearly at $2\theta = 39.6°$ and $2\theta = 44.6°$ which correspond to fcc (111) Pt and fcc (111) Ni, respectively.

It has been pointed out in Sec. 3.3.2, and according to Eq. 3.11, fcc-structure shows reflection peaks only when h, k, and l are even or odd values, therefore, peaks in

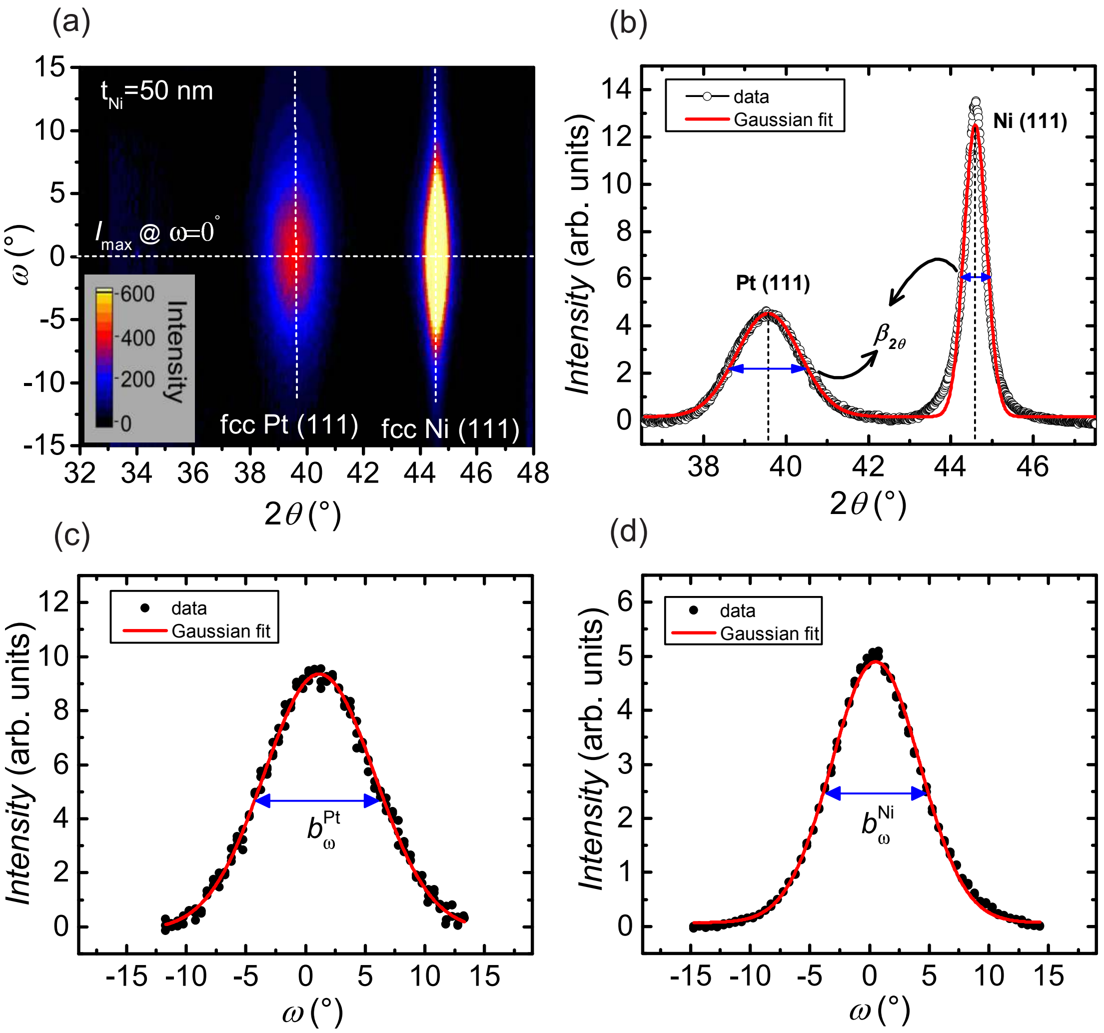

Figure 4.2: (a) Diffraction map $I(\omega, 2\theta)$ of Pt(5 nm)/Ni(50 nm)/Pt(3 nm) sandwich on top of Si_3N_4 substrate. The intensity is color coded according to the given color bar. (b) X-ray diffraction pattern extracted from the map is shown with open circles, while the red line is the Gaussian fit to the data. By determining the position of Pt fcc (111) and Ni fcc (111) peaks it is possible to calculate the lattice parameters of Pt an Ni. (c) and (d) The cross-section $I(\omega)$ at the fixed peak position of $2\theta_{\mathrm{Pt}} = 39.6°$ and $2\theta_{\mathrm{Ni}} = 44.6°$, respectively. The red lines are the Gaussian fit to the data. b_ω is a measure for the texture of the layer.

(111)-direction are expected to occur, as it is observed for all the samples. Furthermore, the peak-position of fcc (111) for bulk Pt and Ni are reported as $2\theta_{\mathrm{Pt}} = 39.8°$ and $2\theta_{\mathrm{Ni}} = 44.6°$. Ni and Pt peaks were observed for the measured samples in the vicinity of bulk positions. Only for the sample with 2 nm Ni thickness there was no peak at Ni position detectable. This is due to less amount of Ni material comparing to Pt.

These peaks correspond to the fcc lattice parameters $a_{\mathrm{Pt}} = 0.392\,\mathrm{nm}$ and $a_{\mathrm{Ni}} = 0.352\,\mathrm{nm}$, respectively [98]. The ratio of integrated intensities, which is the ratio of integrated peak intensities in Fig. 4.2(b), can be achieved from Eq. 3.12

$$\frac{I_{\mathrm{Ni}}}{I_{\mathrm{Pt}}} = \kappa\,\frac{t_{\mathrm{Ni}}}{t_{\mathrm{Pt}}} = 0.165\,\frac{t_{\mathrm{Ni}}}{t_{\mathrm{Pt}}} \tag{4.1}$$

where the structure factor for fcc (111) structure is $F^2 = FF^* = (4f)^2$ (Eq. 3.11) and unit cell volume for cubic crystal is a^3. Moreover, the atomic scattering factors for Ni and Pt are $f_{\mathrm{Ni}} = 20.5$ and $f_{\mathrm{Pt}} = 19.5$, which were taken from references [103, 104]. As an example, for the sample shown in Fig. 4.2, $\kappa = 0.158 \pm 0.003$ is calculated from the ratio of integrated intensities (the area under the peaks). The whole thickness dependence of ratio intensities is shown in Fig. 4.3(b) and is discussed in the results.

Generally, the crystallite size and the presence of strain in crystals can be estimated from the full width at half maximum (FWHM) of an individual peak by Scherrer's formula as follows [104]

$$d_{\mathrm{grain}} = \frac{0.94\lambda}{\beta_{2\theta}\cos\theta} \tag{4.2}$$

here, d_{grain} is the average crystallite size measured in a direction perpendicular to the surface of the specimen, θ is the Bragg angle, and $\beta_{2\theta}$ is the angular width (FWHM) in radians. The equation is commonly used for cubic samples and suitable for Ni/Pt structure and was derived based on assumption of Gaussian line profiles.

Additionally, the distribution of the crystallite orientations in a polycrystalline thin film is not always isotropic. In contrast, it was found in many studies that a certain crystallographic direction [hkl] is preferentially oriented with respect to the sample reference frame. This anisotropy of crystallite orientation is called texture or preferred orientation. Since many physical properties of polycrystals sensitively depend on the texture, it is essential to determine this structural anisotropy.

Fig. 4.2(c) and (d) show the cross-section $I_{2\theta}(\omega)$ of the diffraction map at the peak positions $2\theta_{\mathrm{Pt}} = 39.6°$ and $2\theta_{\mathrm{Ni}} = 44.6°$, respectively. The peaks are fitted to normal distribution function. It is seen that the maximum of the peaks occur around $\omega = 0$. The observation of maximum at $\omega = 0$ together with the peak positions of fcc Pt (111) and Ni (111) (Fig. 4.2(b)) indicate that the crystallites are preferentially

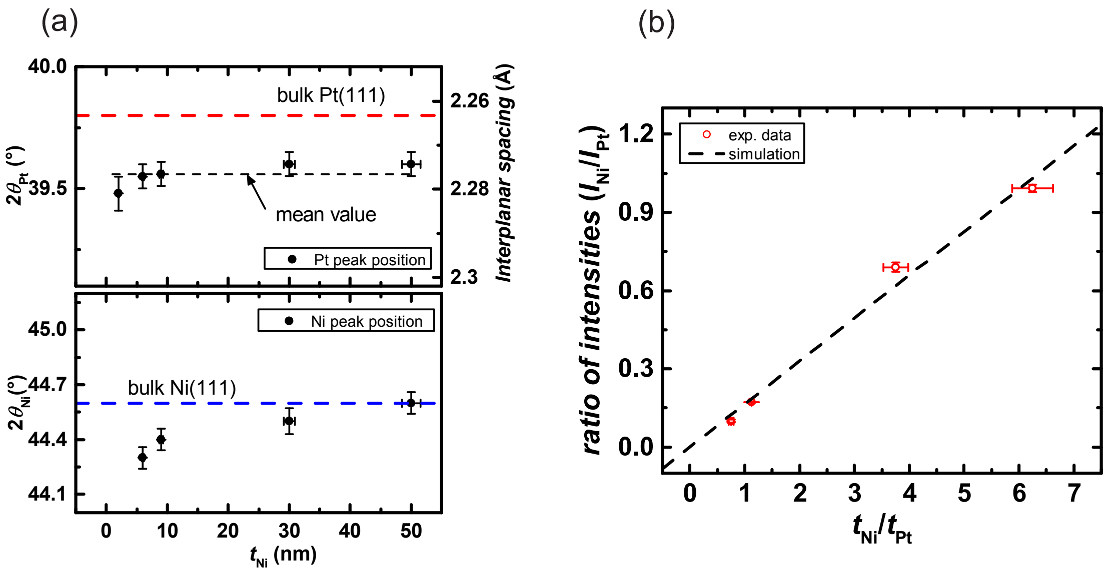

Figure 4.3: (a) Peak position (2θ) of Pt and Ni layer vs t_{Ni}. (b) The ratio of intensities as a function of $t_{\mathrm{Ni}}/t_{\mathrm{Pt}}$ is calculated from XRD pattern. The black dashed line is the calculation according to Eq. 4.1. The experimental data is in good agreement with Eq. 4.1 obtained from the tabulated values for atomic scattering factors of Ni and Pt.

oriented with the (111) lattice planes parallel to the film surface. Therefore, Ni/Pt films exhibit an out-of-plane (111) texture. As a result a quantitative measure for the degree of the texture is obtained from the FWHM of $I(\omega)$. Here in the case of 50 nm Ni thickness sample $b_\omega^{\mathrm{Ni}} = (9 \pm 1)^\circ$ and $b_\omega^{\mathrm{Pt}} = (11 \pm 1)^\circ$ are measured from Fig. 4.2(c) and (d), respectively. Furthermore, the absence of (200) peak is another indication for the (111) texture of the films.

The XRD-map measurement has been done for samples with Ni thickness 6, 30, and 50 nm and linescan measurements ($I(2\theta)$ at $\omega = 0$) has been done for samples with 2, and 9 nm Ni thickness. In the following the peak position, the ratio of intensities, the grain size as well as the texture of the structures are discussed and compared.

Results and discussion of XRD measurements

Fig. 4.3(a) shows the position of the Ni and of the Pt peak in dependence of the Ni thickness. It has to be mentioned that for the samples with $t_{\mathrm{Ni}} \leqslant 9$ nm two peaks were observed at the position of Pt peak. Therefore, the envelope Gaussian fit is used in these cases. Shown in Fig. 4.3(a) the Pt peak position does not change with thickness within the error margin of the experiment. The mean value of $2\theta_{\mathrm{Pt(111)}} = (39.56 \pm 0.05)^\circ$ was found, which corresponds to an interplanar spacing of $d_{\mathrm{Pt}} = (2.276 \pm 0.003)$ Å. The obtained value is about 0.6% larger than the Pt bulk value ($d_{\mathrm{Pt,bulk}} = 2.263$ Å), which means that the Pt seed layer grows slightly strained.

In contrast to Pt, the position of Ni peak changes with Ni thickness. It is observed that by increasing t_{Ni} the position of the peak increases leveling for the two thickest samples (30 and 50 nm Ni thickness) into the bulk value. According to kinematic approximation[1] it is expected that in the case of thickness-independent interplanar spacing d and coherent growth the position of the Ni peak increases with the Ni thickness. Details about coherent model can be found in Ref. [11]. Similar behavior was observed for Co/Pt and Co/Pd [77]. For the two thickest samples the mean value of peak position is determined to $2\theta_{\mathrm{Ni}} = (44.55 \pm 0.03)^{\circ}$, which corresponds to an interplanar spacing of $d_{\mathrm{Ni}} = (2.034 \pm 0.003)$ Å. This value is about 0.1% smaller than the bulk value $d_{\mathrm{Ni,bulk}} = 2.036$ Å. Therefore, it can be concluded that at least parts of the Ni layer exhibit the bulk crystal lattice.

Another interesting information can be extracted from the XRD pattern is the crystallite size in depth. It is seen that the width of the Pt peak is independent of t_{Ni}. Utilizing Scherrer Eq. (4.2) and substituting the FWMH of Pt peak reveals that $d^{\mathrm{Pt}}_{\mathrm{grain}} = (4.8 \pm 0.1)$ nm. This corresponds to the thickness of the Pt seed layer and reveals the dominance of the seed layer in the signal. As a result, it can be concluded that the Pt layers consist of single crystalline phases along the stacking direction [11].

Unlike the grain size of Pt which is almost constant for measured samples as it is expected, the obtained values for Ni grain size are in dependent of thickness. It is found that the width of the Ni peak is almost similar for the two thicker samples (30 and 50 nm Ni thickness) with $\beta^{\mathrm{Ni}}_{2\theta} = (0.62 \pm 0.02)^{\circ}$. According to Scherrer equation and using the mean value of Ni peak position ($2\theta_{\mathrm{Ni}} = (44.55 \pm 0.05)^{\circ}$ for thicker samples) a coherence length of $d^{\mathrm{Ni}}_{\mathrm{grain}} = (15.9 \pm 0.5)$ nm is calculated. This might be due to a loss in long-range crystalline order within the Ni layer at large Ni thicknesses. Additionally, the width of Ni peak for the two thinner samples (6 and 9 nm Ni thickness) are not constant values and it seems that for $t_{\mathrm{Ni}} \leqslant 15$ nm the crystallinity of Ni layer depends on Ni thickness. In this regime the crystallite size is almost $d^{\mathrm{Ni}}_{\mathrm{grain}} = t_{\mathrm{Ni}}$. Therefore, it can be concluded that the Ni layer is also in the single crystalline phase in thicknesses below 15 nm.

As shown in Fig. 4.2, Ni/Pt thin film demonstrates a pronounced out-of-plane (111) texture in general result. While the distribution of the orientation of the grains is well fitted by a Gaussian, a quantitative measure of the degree of texture is the full width at half maximum b_{ω}, which is independent of t_{Ni}. The mean value of $b^{\mathrm{Pt}}_{\omega} = (12 \pm 1)^{\circ}$ and $b^{\mathrm{Ni}}_{\omega} = (10 \pm 1)^{\circ}$ are obtained for the measured samples. It can be concluded from the thickness independence of b_{ω} that the texture is already determined by the growth of the seed layer on the substrate and does not change during Ni growth. Moreover, the comparable values obtained for Ni and Pt reveals that Ni grows very well on top of Pt.

---

[1] The kinematical approximation assumes that contributions from multiple scattering are negligible, it neglects interference between scattered and incident beams, and assumes that the reduction in intensity of the scattered wave inside the crystal lattice (due to extinction and absorption) is small [105].

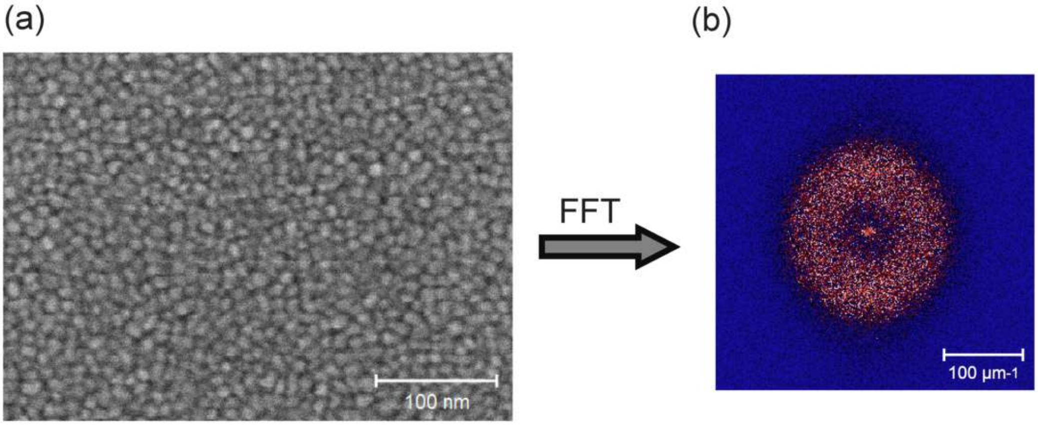

Figure 4.4: (a) Image of Pt/Ni/Pt sandwich with 50 nm Ni thickness taken with scanning electron microscopy (SEM). (b) Fast Fourier transformation pattern from the entire image in (a).

Fig. 4.3(b) displays the ratio of intensities $I_{\mathrm{Ni}}/I_{\mathrm{Pt}}$ for each sample as a function of $t_{\mathrm{Ni}}/t_{\mathrm{Pt}}$. The dashed line presents the calculation according to Eq. 3.12 and 4.1. Obviously, the experimental data are in good agreement with the calculation revealing that the bulk parameter (atomic scattering factors) of Pt and Ni used in the model can perfectly describe the experimental data.

In addition to determination of grain size in depth, SEM has been used to specify the lateral grain size of Ni/Pt layered structures. Fig. 4.4(a) shows a recorded SEM image of the sample with $t_{\mathrm{Ni}} = 50\,\mathrm{nm}$. Using Fourier transformation (see Fig. 4.4(b)), a lateral grain size of $d^{\mathrm{lateral}}_{\mathrm{grain}} = (14 \pm 2)\,\mathrm{nm}$ was found for Pt/Ni(50 nm)/Pt. This is an indication of a structure with columnar growth occurring during the subsequent magnetron sputtering of the Ni and Pt layers.

Transmission Electron Microscopy is another useful tool for investigating the morphology of surface and interfaces of thin films. Therefore, high resolution TEM measurements have been preformed on the samples with $t_{\mathrm{Ni}} = 2$, 9, and 30 nm by Dr. Andrey Chuvilin from CIC nanoGUNE, Spain. Fig. 4.5(a) shows a representative TEM image of the cross section of the sample with 30 nm Ni thickness. In this technique, a delicate destructive sample preparation is required to get a thin slab piece of the sample which is done by Focused Ion Beam (FIB). In order to protect the sample, a layer (Pt+C) has to be deposited on top. Columnar growth of Ni can be recognized as another proof of XRD result.

Moreover, a 2D spectrum of energy profile from Fig. 4.5(a) is shown in Fig. 4.5(b). The colorful map (down part) has the depth coordinate in y-axis and energy coordinate in x-axis. The image to the left and the spectrum on top give information about scales. Appearance of a special peak at particular depth reflects unambiguously the existence of the element at this depth. First of all, it is seen that carbon and gallium are everywhere. The first one is due to the contamination by SEM beam and the protection Pt layer containing 70% carbon, while the latter one is because of the

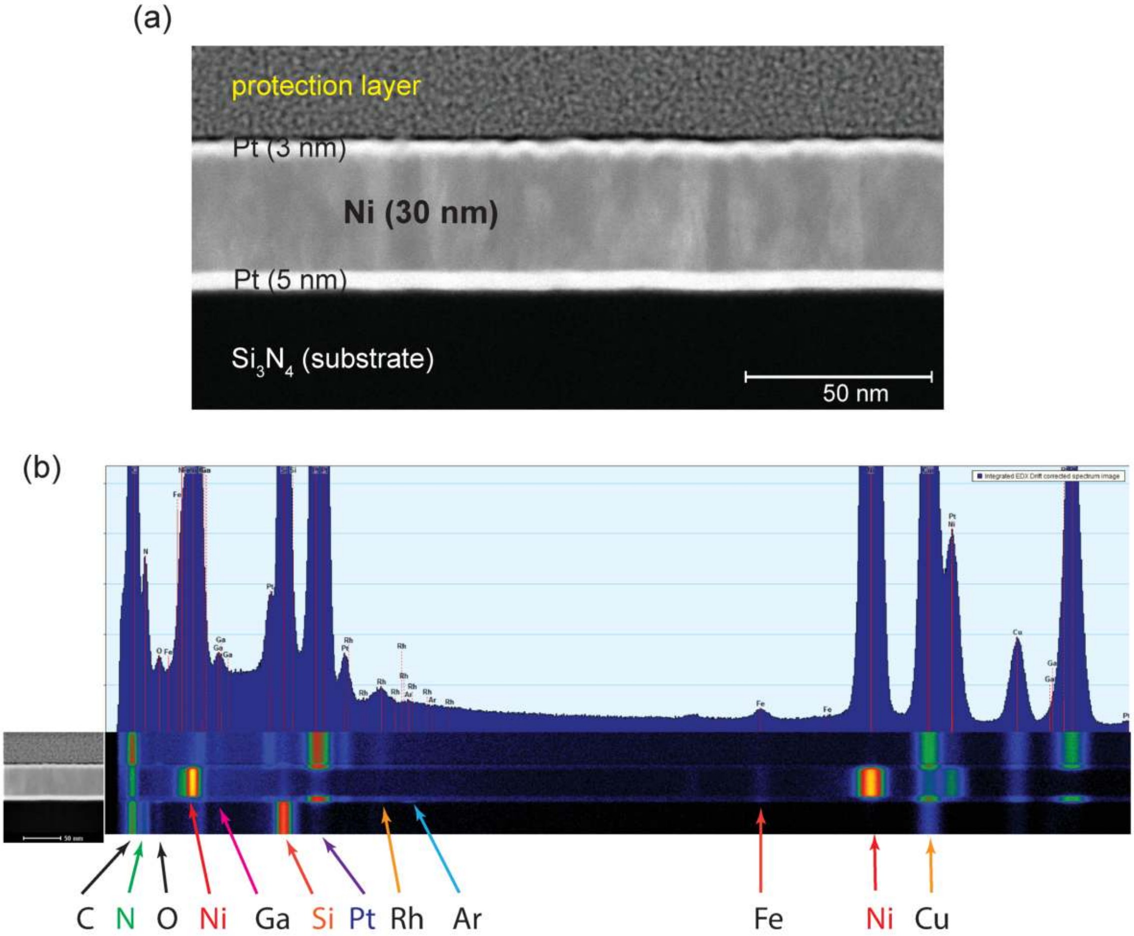

Figure 4.5: (a) Cross-sectional HRTEM image of Pt(5 nm)/Ni(30 nm)/Pt(3 nm) on top of Si_3N_4 as a substrate. The columnar growth of Ni can be seen. (b) A 2D spectrum energy profile obtained from (a).

implantation during FIB milling. Copper is a background signal from the grid and is correlated to the density of material. Existence of argon in the substrate is because of using Ar^+ ion-assisted sputtering with high Ar energies for the Pt seed layer growth. Silicon and nitrogen are in the substrate. Pt and Ni are in the layer that they should be, while weak peak of Pt is also observed in protection layer. A very thin layer of oxygen is detected in the substrate and on top of the sample. Carbon and silicon together with oxygen observed on top of the sample should be due to some organic contamination. The most important result achieved by the HRTEM measurement is that there is no NiO layer observed in the Ni layer.

4.1.2 X-ray Reflectometry (XRR)

In order to obtain information about the interfacial properties of Ni/Pt sandwiches, in this section, I present the experimental results of X-ray reflection measurements. It has to be mentioned that the same setup is used for X-ray reflectometry as XRD

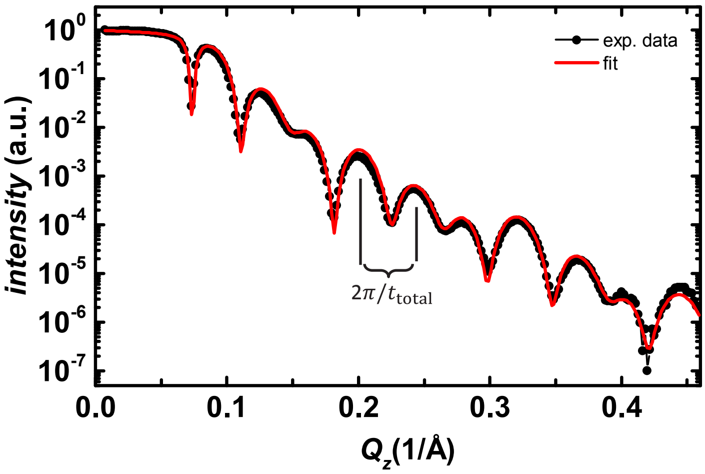

Figure 4.6: The specularly reflected intensity as a function of wave vector for a sample with 6 nm Ni thickness. The red line is the fit to the data.

measurements only with incidence angles less than 10°.

As mentioned in Sec. 3.3.1, the reflection of a single layer on a substrate can be described as the interference of the reflection at two interfaces leading to oscillatory pattern. By solving the Fresnel equations for reflection and transmission including multiple scattering from the two interfaces, the reflectivity can be obtained [106].

In the reciprocal space, incident and reflected wave are described with their wave vectors k_i and k_f, where $|\mathbf{k}| = 2\pi/\lambda$. In our geometry k_i, k_f, and normal to the sample surface lying in the refraction plane. Therefore, the transferred momentum in the case of specular reflectivity is $Q_z = 4\pi \sin\theta/\lambda$, where θ is the angle of incidence/reflection. Beside presenting reflectivity data versus 2θ, it is also common to plot reflectivity data versus transferred momentum, Q_z. The total thickness, t_{total}, of the layers can be determined from the oscillation distance, ΔQ_{z}, by

$$\Delta Q_{\mathrm{z}} = \frac{2\pi}{t_{\mathrm{total}}} \tag{4.3}$$

The reflectivity features of a multilayer system can be described in the same way as for a single layer which means that Fresnel equations for reflection and transmission have to be solved for all interfaces. Fig. 4.6 shows as an example the specular X-ray intensity for sample with $t_{\mathrm{Ni}} = 6\,\mathrm{nm}$ over the Q_z range $0.005\,\text{Å}^{-1} < Q_z < 0.6\,\text{Å}^{-1}$. Using Eq. 4.3 and ΔQ_{z} shown for both periods the total thickness of the stack was determined and this value verifies the nominal total thickness (obtained from used deposition rates) of the sample.

In order to analyze the reflectivity curves different algorithms were developed and used in literature [107, 108]. However, in this work I have used MOTOFIT package which runs in the IGOR Pro[2] environment [109]. Utilizing this model it is possible to determine the width of the roughness/interdiffusion region from the specular reflectivity curve. To fit the data the scattering length density of Ni and Pt has to be known. The real and imaginary part of scattering length density (β and δ) can be calculated for a particular wave length $\lambda = 1.5406\,\text{Å}$ and element from the homepage of the center of X-ray optics database (CXRO)[3]. These parameters are given in table 4.1.

	SLD(δ) (Å^{-2})	iSLD(β) (Å^{-2})
Ni	6.4×10^{-5}	1.3×10^{-6}
Pt	1.4×10^{-4}	1.3×10^{-5}
Si_3N_4	2.9×10^{-5}	4.4×10^{-7}

Table 4.1: Scattering length density of Ni, Pt, and Si_3N_4.

It is seen that the fit model can describe the experimental data very well. Concerning the thickness of Ni and Pt layers the result of the analysis of XRR measurements does not show any dependency on t_{Ni}. An average value of $t_{\text{Pt,seed}} = (49.7 \pm 1.0)\,\text{Å}$ and $t_{\text{Pt,cap}} = (29.9 \pm 1.0)\,\text{Å}$ are deduced from the fit which are in good agreement with nominal Pt thicknesses. The thickness of Ni layer achieved from the fit verifies the nominal thickness within the error margin of the experiment. Furthermore, it should be mentioned that the thickness of individual layer from XRR investigation are similar to the result of TEM measurements.

In addition to the thickness results, roughness/interdiffusion region of interfaces again does not show any significant changes with Ni thickness. From the analysis of the measurements a mean value of $(4 \pm 2)\,\text{Å}$ and $(8 \pm 2)\,\text{Å}$ were found for the width of roughness/interdiffusion region of Pt(seed)-Ni and Ni-Pt(cap), respectively. It can be concluded that the degree of roughness/interdiffusion at the interfaces remain constant, so that their influence on the magnetic properties do not change with thickness.

4.2 Sample layout and measurement geometries

In order to investigate the MR effects of Ni/Pt sandwiches, a series of samples were fabricated simultaneously with reference samples[4] (laterally homogeneous films) with sputtering methods, explained in Sec. 3.1. In the fabrication procedure, we use a shadow mask on top of substrate (Si_3N_4) to make a wire-shape film with dimension of $w \times l = 0.5 \times 6\,\text{mm}^2$. Using wire-shape samples make the calculation of the resistance and subsequently the resistivity from the measured data (voltage) straightforward:

---

[2] https://www.wavemetrics.com

[3] http://henke.lbl.gov/optical_constants/pert_form.html

[4] The reference samples were utilized for the structural characterization.

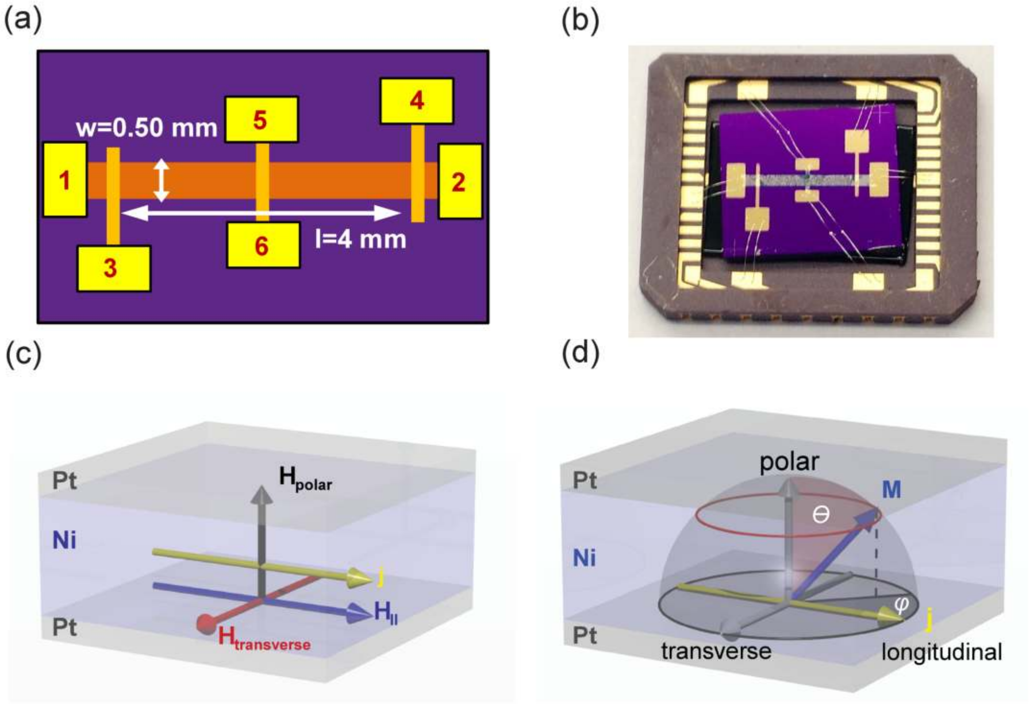

Figure 4.7: (a) Layout of Ni/Pt sample on top of Si_3N_4 with the wire-shaped film and 6 contact pads. The current flows through the sample via contacts 1 & 2. Longitudinal voltage U_x measured between contacts 3 & 4, while transverse voltage U_y is simultaneously recorded between contacts 5 & 6. (b) Photo of sample electrically contacted to the chip carrier. (c) MR measurements were done in these three geometries. *Longitudinal* (ll) geometry is the case when the external magnetic field is applied parallel to the current direction, *transverse* (t) geometry is measured when the magnetic field is applied perpendicular to the current direction in the film plane, and *polar* (p) geometry is defined with the magnetic field parallel to **n** (surface normal). The sketch is from Ref. [11]. (d) The angular dependence of the resistance was probed by rotating the magnetization within two different planes: in-plane rotation $\rho_{\mathrm{xx}}(\varphi, \theta = 90°)$ and out-of-plane rotation $\rho_{\mathrm{xx}}(\varphi = 90°, \theta)$. The sketch is from Ref. [102].

$$R_{xx}(H) = \frac{U_x}{I_x}, \quad \rho_{xx} = R_{xx}\frac{w\ t}{l} \tag{4.4}$$

where t is the film thickness. The electrical resistance of the films was measured at room temperature utilizing a DC four-probe method under an external magnetic field (μ_0H) up to 6 T. In order to apply current and measure simultaneously the longitudinal and transverse voltage, the samples have to be electrically contacted with 6 chrome/gold contact pads as illustrated in Fig. 4.7(a). Moreover, the samples are attached to chip carriers, while the electrical connection between the contacts on the sample and the contacts of chip carrier is provided by aluminum wires with 25 µm thickness, produced by ultrasonic wire bonding. Fig. 4.7(b) shows a prepared sample attached to a chip carrier.

As explained in Sec. 3.2, the MR measurements were carried out at room temperature using a warm-boremagnet setup, which provides a vertical magnetic field with a superconducting magnet. All the current inplane MR measurements in this thesis were performed with two different methods, shown schematically in Fig. 4.7(c) and (d).

Method 1: First of all, the MR of the sample was measured in three different fixed geometries while the magnetic field was swept from -6 T to +6 T. According to Fig. 4.7(c), these three geometries are commonly known as **longitudinal** (ll), when the magnetic field is applied parallel to the current direction, **transverse (t)**, and **polar (p)**, when the magnetic field is applied perpendicular to the current direction in the film plane and out of the film plane, respectively. The sweep rate was set to 0.2 T/min and every 3 s the longitudinal and transverse voltage were being recorded by two nanovoltmeters.

Method 2: In contrast to the first method, the sample is rotated in two different directions while the magnetic field is fixed to the constant value of $\mu_0|\mathrm{H}|= \pm 6\,\mathrm{T}$, which is sufficiently large to saturate the magnetization. The so-called *in-plane* (ip) rotation is related to the angular dependence of resistance with respect to the current direction *in the film plane*. In this case the sample was rotated around **n** between longitudinal and transverse geometries. $\theta = 0$ corresponds to longitudinal geometry. In addition, *out-of-plane* (op) rotation concerns to a rotation of magnetization in the *plane perpendicular to the current* direction while the magnetic field was kept constant (see Fig. 4.7(d)). The rotation axis is the current direction with $\varphi = 0$ denoting the polar geometry. In both cases the sample is rotated in 5-10° steps in the range of $-95° \leq \theta, \varphi \leq +95°$. It is worth mentioning that due to the shorter time-span of rotation measurements comparing to the method 1, the impact of thermal drift is significantly reduced.

4.3 Determination of magnetic anisotropy

In the presence of external magnetic field the total free energy of the system can be written as

$$E/V = K_{1,\mathrm{eff}} \sin^2 \Theta + K_2 \sin^4 \Theta - \mu_0 \ H \ M_\mathrm{S} \cos \Phi \tag{4.5}$$

with the latter term corresponds to the Zeeman energy contribution and the free energy density is applied in second order approximation of anisotropy. Θ is the angle between **M** and the sample normal **n**, while Φ describes the angle between **M** and **H**.

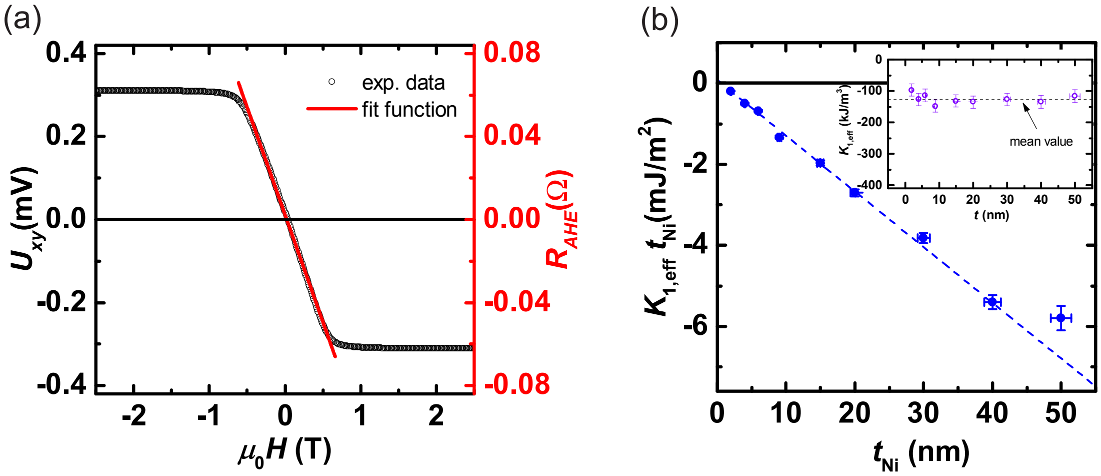

Figure 4.8: (a) Out-of-plane remagnetization measurement of Ni/Pt with $t_{\mathrm{Ni}} = 9\,\mathrm{nm}$. In order to obtain the anisotropy constant the fit (red line) is applied below technical saturation. (b) Variation of effective anisotropy times Ni thickness $K_{1,\mathrm{eff}}\, t_{\mathrm{Ni}}$ versus Ni thickness in Pt/Ni/Pt sandwiches determined at room temperature using AHE. $K_{\mathrm{s}} \approx (0.015 \pm 0.030)\,\mathrm{mJ/m^2}$ and $K_{1\mathrm{V,eff}} \approx (-133 \pm 3)\,\mathrm{kJ/m^3}$ were obtained from the linear fit (dashed line). $K_{1,\mathrm{eff}}$ versus t_{Ni} is given as inset.

In order to determine the anisotropy constants an external magnetic field has to be applied in the direction of hard axis of magnetization. In all of the Ni/Pt structures in this work the easy axis is in-plane and the hard axis is out-of-plane. Therefore, with applying an out-of-plane external field we have the condition $\Theta = \Phi$. By minimizing the total free energy $\partial(E/V)/\partial\Theta$ and using the latter condition, it follows:

$$\begin{aligned} 2K_{1,\mathrm{eff}} \cos\Theta + 4K_2 \cos\Theta \sin^2\Theta &= -\mu_0\ H\ M_{\mathrm{S}} \\ -\left(\frac{2K_{1,\mathrm{eff}}}{M_{\mathrm{S}}} + \frac{4K_2}{M_{\mathrm{S}}}\right) m_\perp + \frac{4K_2}{M_{\mathrm{S}}} m_\perp^3 &= \mu_0\ H(m_\perp) \end{aligned} \tag{4.6}$$

where $m_\perp = M_\perp / M_{\mathrm{S}} = \cos\Theta$ is the component of magnetization in the direction of magnetic field and with the help of Eq. 4.6 the anisotropy constants can be obtainable from the magnetization behavior of the sample.

Fig. 4.8(a) shows the result of $R_{\mathrm{AHE}}(H_{\mathrm{p}})$ measurement for Pt/Ni (9 nm)/Pt. Above technical saturation $R_{xy}(H_{\mathrm{p}})$ curves follow a linear negative slope as a consequence of ordinary Hall effect (see Fig. 4.11). Here, the high field behavior was extrapolated to zero field and the extrapolated curve was subsequently subtracted from $R_{xy}(H_{\mathrm{p}})$ measurement. The remain curve is $M_p(H_{\mathrm{p}})$ ($R_{AHE}(H_{\mathrm{p}})$) which is used to determine anisotropy constant (Fig. 4.8(a)).
Using Eq. 4.6 to fit the data below technical saturation reveals that the obtained values for K_2 changes randomly in the range of 1 - 40 kJ/m^3. Moreover, due to the lack of investigations of anisotropy constants in special systems like Pt/Ni/Pt in

literature, I could hardly compare my results with other studies. For the following analysis I set K_2 to zero to avoid an impact of varying K_2 on $K_{1,\mathrm{eff}}(T, t_{\mathrm{Ni}})$ as a fit parameter. Here, in the case of the sample with $t_{\mathrm{Ni}} = 9\,\mathrm{nm}$ the effective first order anisotropy is determined to be $-148\,\mathrm{kJ/m^3}$ which is one order of magnitude smaller than for similar Co/Pt layered structure studied by A. Kobs [11]. The thickness dependence of $K_{1,\mathrm{eff}}$ is shown as inset in Fig. 4.8(b). It is seen that the anisotropy is almost constant within the error margin of the experiment with the mean value of $K_{1,\mathrm{eff}}^{\mathrm{mean}} = (-126 \pm 20)\,\mathrm{kJ/m^3}$.
Fig. 4.8(b) presents the thickness dependence of $K_{1,\mathrm{eff}}\, t_{\mathrm{Ni}}$ of all samples which is commonly used to disentangle the surface and effective bulk anisotropies according to Eq. 2.14. The dashed line is a linear fit to the data with a negative slope and a positive (almost zero) intercept on y-axis. The slope is an indication of shape anisotropy and magnetocrystalline volume anisotropy ($K_{1\mathrm{V,eff}} = K_{1\mathrm{V}} - \frac{\mu_0}{2} M_{\mathrm{S}}^2 \approx (-133 \pm 3)\,\mathrm{kJ/m^3}$) (see Sec 2.1.4). With the saturation magnetization of Ni bulk at room temperature $M_{\mathrm{S}}^{\mathrm{bulk\ Ni}} = 0.493\,\mathrm{MA/m}$ [98], the shape anisotropy can be calculated as $K_{\mathrm{d}} = -\frac{\mu_0}{2} M_{\mathrm{S}}^2 = -153\,\mathrm{kJ/m^3}$ and consequently the effective first order volume anisotropy is $K_{1\mathrm{V}} = 20\,\mathrm{kJ/m^3}$. In addition, the surface anisotropy from the linear fitting of Fig. 4.8(b) is $K_{\mathrm{s}}^{\mathrm{Ni}} = (0.015 \pm 0.030)\,\mathrm{mJ/m^2}$ which is one order of magnitude smaller than $K_{\mathrm{s}}^{\mathrm{Co}}$ in Co/Pt systems [11, 77] and Co/Pd structure [61, 77]. The measured value for K_{s} are within the span of values reported in literature for Ni-based systems like Ni/Pd multilayers -0.48 - $0.51\,\mathrm{mJ/m^2}$ [31–36, 110]. The effective first order anisotropy calculated for Ni/Pt sandwiches here, is also similar to the Ni/Pd systems investigated by Chafai et. al and den Broeder ($K_{1,\mathrm{eff}} = -125$ to $-140\,\mathrm{kJ/m^3}$) [33, 34] within the error margin of the experiment.

4.4 Dependence of resistivity on sweeping magnetic field

After studying the structural and magnetic properties of Pt/Ni/Pt sandwiches the results of magnetoresistance measurements and corresponding effects will be presented and discussed in this section.

$\rho_{xx}(\mathbf{H})$: First of all, according to the first method explained above, the field sweep of all samples has been measured while the external field is fixed in longitudinal, transverse, and polar geometries with respect to the current direction. Fig. 4.9 presents as an example the magnetoresistance measurement of Pt/Ni(15 nm)/Pt as a function of magnetic field. It has to be mentioned that all the samples exhibit the same qualitative behavior shown in this figure. It can be seen that at high field above technical saturation, where $\mathbf{M}$ is aligned in parallel to the field, the resistivity reduces linearly, for all three geometries, with external magnetic field due to the spin-disorder magnetoresistance effect (SMR) (see Sec. 2.2.6) [9].

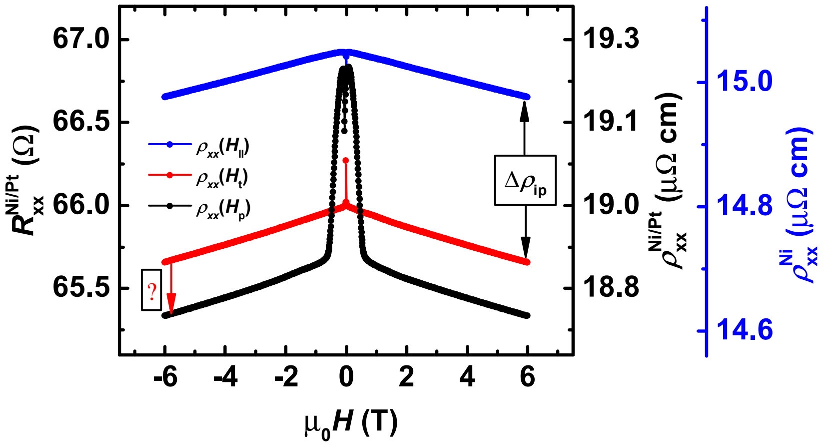

Figure 4.9: Magnetoresistance measurements of Pt(5 nm)/Ni(15 nm)/Pt(3 nm) in longitudinal $H_{||}$, transverse H_t, and polar H_p geometries. $\Delta\rho_{ip}$ is the typical AMR effect. The blue axis show the resistivity of Ni layer after elimination of current shunt through Pt (see Sec. 4.6.1).

For both longitudinal and transverse geometries, a linear decrease of resistivity $\rho_{xx}(\mu_0 H)$ (resistance $R_{xx}(\mu_0 H)$), has been found on increasing the absolute value of external field almost in the entire range of measurement. As we will see below, this behavior is expected for specimens with in-plane easy axis of magnetization. At zero field, a sudden jump of the resistivity happens, which is due to the fact that the magnetization is a multi-domain state with no preferred in-plane direction. Hence, the measured resistance corresponds to an average value of all orientation of the magnetization in the sample plane. In other words, this sudden jump (or fall) is attributed to multi-domain state during switching of the magnetization, leading to an increase or decrease of resistivity.

Applying a field perpendicular to the film surface yields the resistivity in polar geometry. The parabolic behavior observed in polar geometry is due to the coherent rotation of the magnetization into the direction of hard axis ($\mu_0 H < 1\,\mathrm{T}$). This quadratic shape can be well described by AMR and AIMR, in which the resistivity depends on the angle between the magnetization and current [9, 10]. At high fields (above 1 T) the magnetization aligns along the external field, and only the electron-magnon scattering (spin-disorder MR) with negative slope is observed. Notably, the isotropic behavior of ρ_{xx} for all geometries at high field reveals that rotation of the sample in saturation field provides access to AMR and AIMR effects. Therefore, the angular dependence of resistivity on magnetization direction were measured and is the topic of the following section.

In this work, the magnetogalvanic effects investigated in Pt/Ni/Pt structures are compared step by step with the result for Pt/Co/Pt sandwiches, which was studied in detail by A. Kobs [11]. This is due to the fact that the starting point of my study

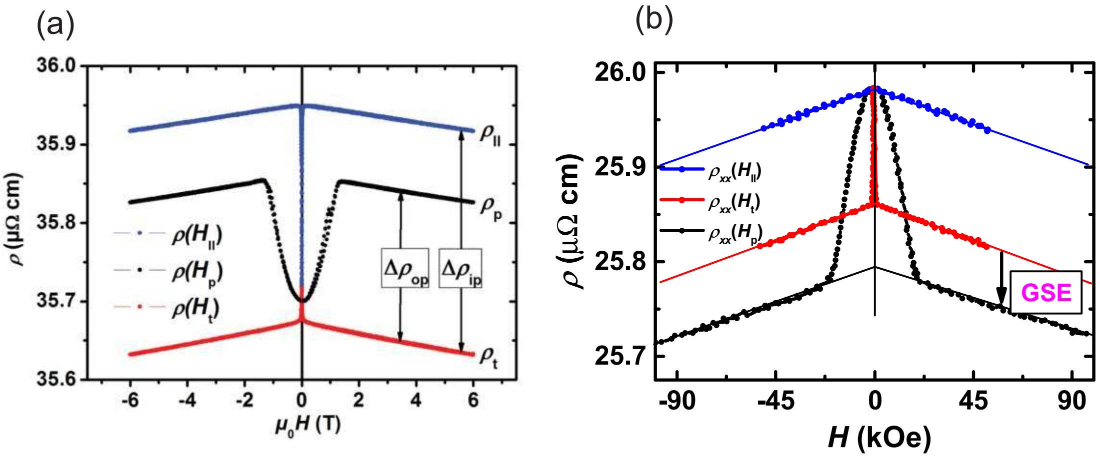

Figure 4.10: (a) The longitudinal resistivity ρ_{xx} of Pt(5 nm)/Co(6 nm)/Pt(3 nm) plotted against magnetic field oriented along the three generic directions (polar, longitudinal, and transverse) with respect to the current direction and film normal [10]. (b) High field magnetoresistance of 20 nm pure Co film at room temperature for the same directions of the field. $\rho_\mathrm{p} < \rho_\mathrm{t}$ is due the texture of the film [55].

is the discovery of Anisotropic Interface Magnetoresistance (AIMR) effect found in Co/Pt sandwiches [10]. As stated briefly in Sec. 2.2.4, the magnetoresistance properties of Co/Pt layered structures was investigated in current in-plane (CIP) geometry at room temperature in our group by A. Kobs. It was found that the resistivity depends on the magnetization direction when it rotates in the plane perpendicular to the current direction. In order to find the origin of this effect, in that study, a series of Pt/Co/Pt samples were fabricated with the same preparation procedure here for Pt/Ni/Pt.

For comparison, Fig. 4.10(a) shows the typical magnetoresistance results measured for a Pt/Co/Pt sample with 6 nm Co thickness from Ref. [10]. The interesting part is that in Ni/Pt sample (Fig. 4.9) the polar resistivity ρ_p is less than the transverse one ρ_t which is obviously opposite to the findings of Co/Pt specimen shown in Fig. 4.10(a). This difference was enough to draw my attention towards investigating in detail the magnetoresistance effects in Ni/Pt sandwiches.

Looking into literature, the geometrical size effect (GSE) can cause a difference between in plane and out of plane resistivity with $\rho_\mathrm{p} < \rho_\mathrm{t}$ as it is observed in Co, Ni, and permalloy [56, 57, 111, 112]. As an example, Gil et al. [55] reported the same performance ($\rho_\mathrm{p} < \rho_\mathrm{t}$) for 20 nm pure Co at 295 K which is shown in Fig. 4.10(b). It was explained in Sec. 2.2.3 that in contrast to its name, GSE is caused by the crystalline texture of the sample.

Similar to the findings of Co/Pt layered structure, the resistivity difference in Ni/Pt stacks between $\rho_\parallel$ and ρ_t ($\Delta\rho_\mathrm{ip}$) can be attributed to the conventional AMR effect which is a bulk effect. On the other hand, as is explained in Ref. [10], the resistivity difference from in-plane to out-of-plane configuration ($\Delta\rho_\mathrm{op}$ in case of Co/Pt) comes

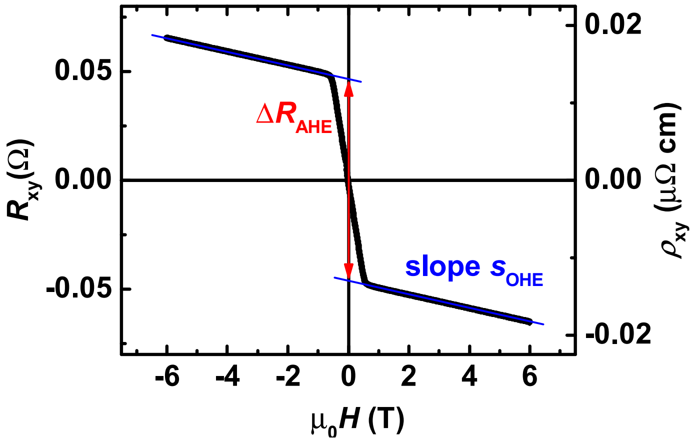

Figure 4.11: Magnetic field dependence of Hall resistance at room temperature for Pt(5 nm)/Ni(15 nm)/Pt(3 nm). The field is applied perpendicular to the film plane. Both Hall constants (R_0 and R_S) have negative values. For 15 nm Ni thickness R_0 =$(-0.046 \pm 0.002) \times 10^{-9}\,\mathrm{m}^3/\mathrm{C}$ and R_S =$(-1.13 \pm 0.06) \times 10^{-9}\,\mathrm{m}^3/\mathrm{C}$ were calculated.

from scattering mechanism at interfaces, therefore, coined Anisotropic Interface MR (AIMR). By comparing figures 4.9 and 4.10, the question arises what is the origin of $\Delta\rho_\mathrm{op} < 0$ in Ni/Pt, is it the presence of GSE effect or the existence of AIMR with negative sign?

In order to find the origin of this effect additional MR measurements according to the second method stated above have been performed and are explained in the following sections (see Sec. 4.5).

$\rho_{xy}(H_p)$: Fig. 4.11 shows $R_{xy}(H_p)$ measurement for Ni/Pt layered structure with 15 nm Ni thickness at room temperature. The magnetic field is applied perpendicular to the film plane which is the direction of hard-axis of magnetization and the curve contains a superposition of anomalous- and ordinary Hall effect. All the samples show the same behavior as Fig. 4.11. At low field ($-0.7\,\mathrm{T} < \mu_0 H < 0.7\,\mathrm{T}$) it is found initially a steep linear rise of the resistance with increasing magnetic field, followed by a second linear behavior having a relatively smaller gradient. The first one is regarded as anomalous Hall effect and the second one is ordinary Hall effect. Therefore, it is possible to calculate Hall constants (R_0 and R_S concerning $\rho_{xy}(H_p)$ measurement.

In Sec. 4.6.3 the behavior of Hall constants versus Ni thickness is discussed.

4.5 Angular dependence of longitudinal resistivity on magnetization direction

The resistivity vs. the magnetization orientation have been investigated according to the second method explained in Sec. 4.2. A constant magnetic field

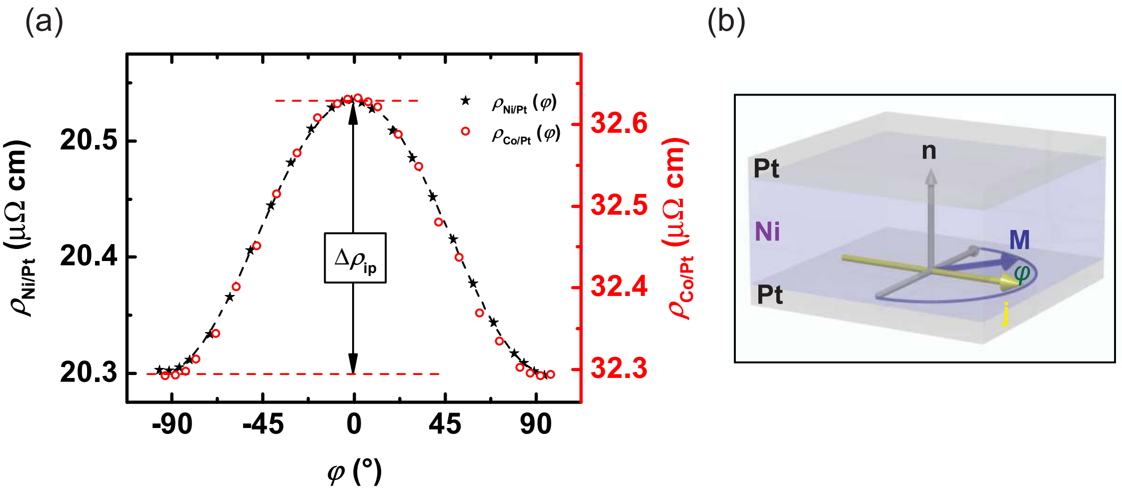

Figure 4.12: (a) Resistivity ρ_{xx} of Ni/Pt sample with 9 nm Ni thickness as a function of angle between magnetization and current direction (black symbols). For comparison the result of Co/Pt sample with the same Co thickness is plotted in the same graph (red symbols). The dashed line is a $\cos^2(\varphi)$ fit. (b) Scheme of in-plane rotation. $\varphi = \pm 90°$ indicates M in transverse geometry while $\varphi = 0°$ in longitudinal direction.

of 6 T (strong enough to saturate the magnetization) is applied along one of the geometries and the sample is rotated at first around the surface normal (ip rotation) and then around current direction (op rotation). In both cases the resistivity is measured as a function of the direction of applied magnetic field which is almost the same as magnetization direction[5]. Mentioned above the isotropic high field behavior of sweep measurement confirms that rotational measurement of resistivity is a consequence of magnetization and not the magnetic field.

In Fig. 4.12(a) the resistivity of Pt(5 nm)/Ni(9 nm)/Pt(3 nm) is plotted (black stars) as a function of angle φ between magnetization and current direction (see scheme in Fig. 4.12(b)). In addition, the in-plane rotation of magnetization of Co/Pt structure with 9 nm Co thickness (similar to Ni/Pt sample) has been plotted on the same graph for comparison (red circles). According to Eq. 2.23, typical $\cos^2$ behavior of magnetization rotation in the film plane is found as we expected for AMR effect. As shown in the plot, the magnitude of AMR effect can be obtained by the amplitude of $\cos^2$ fit. In the case of this sample $\Delta\rho_{\mathrm{ip}}^{\mathrm{Ni}} = (0.236 \pm 0.001)\,\mu\Omega\mathrm{cm}$ is measured for Ni/Pt and $\Delta\rho_{\mathrm{ip}}^{\mathrm{Co}} = (0.340 \pm 0.002)\,\mu\Omega\mathrm{cm}$ is obtained for Co/Pt, which is same order of magnitude.

Rotation of magnetization in the plane perpendicular to the current according to Fig. 4.13(a) was the next step in our measurements. Although a $\cos^2$ symmetry

---

[5] There is a difference between the direction of external magnetic field and magnetization in the case of rotation from easy axes to hard axes, which is discussed and calculated in corresponding section.

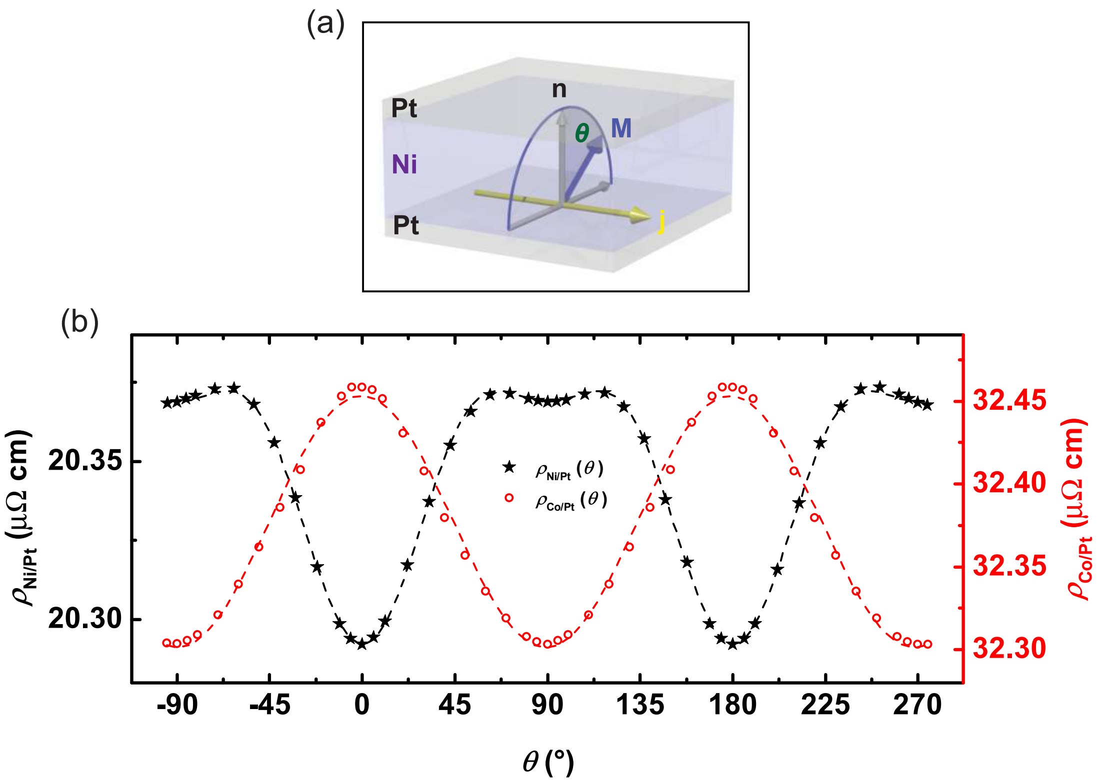

Figure 4.13: (a) Scheme of rotation of magnetization in the plane perpendicular to the current direction. $\theta = \pm 90°$ indicates M in transverse geometry while $\theta = 0°$ in polar direction. (b) Resistivity ρ_{xx} of Ni/Pt sample with 9 nm Ni thickness as a function of θ between magnetization and film normal (black symbols). Out-of-plane rotation of magnetization of similar Co/Pt sample is plotted in red symbols for comparison. Dashed lines are fit functions to the data.

was reported for Co/Pt and also other systems [10, 56, 60, 61, 113], the op rotation of magnetization in Ni/Pt structures shows a completely different behavior. In Fig. 4.13(b), a representative op rotation of a Ni/Pt structure with 9 nm Ni thickness is shown as a function of θ in black symbols. For comparison the result of the same measurement from Co/Pt stack with 9 nm Co thickness is plotted with red symbols as well. In contrast to Co/Pt sandwiches, surprisingly, the $\rho(\theta)$ behavior of Pt/Ni/Pt structures can only be satisfactorily described when considering higher orders in the expansion of MR as

$$\rho(\theta) = \rho_{\mathrm{t}} + \sum_{n} \Delta\rho_{\mathrm{op},2n} \cos^{2n}\theta, \qquad \mathrm{n} \leq 3 \tag{4.7}$$

where θ is the angle between **M** and **n**. Traditionally, AMR has two-fold symmetry. Four-fold symmetry of the AMR, which corresponds to the appearance of an extra higher-order term proportional to $\cos^4$, has been observed first in bulk Fe and Ni single crystals [114–116] and has been reported afterwards for various epitaxial thin films [117–121]. Recently, a four-fold symmetric AMR of single-crystalline Ni(001)

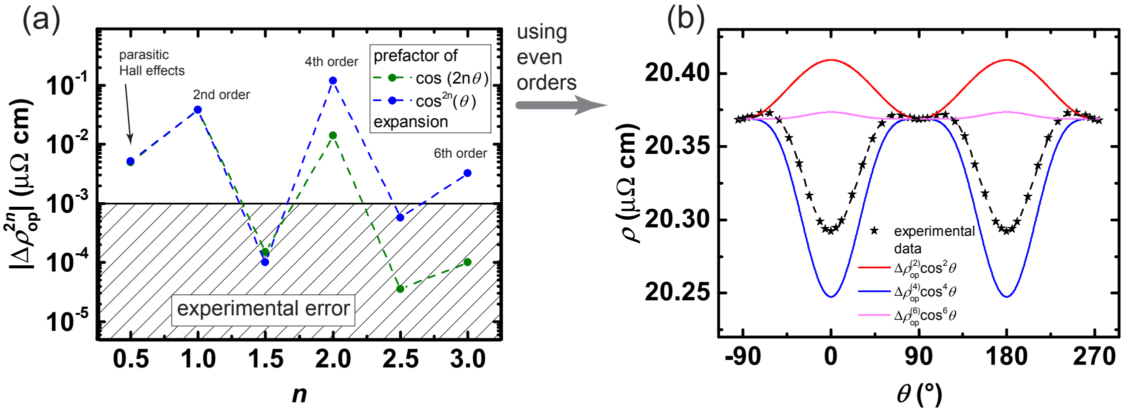

Figure 4.14: (a) Comparing the absolute value of prefactor of $\cos(2n\theta)$ and $\cos^{2n}(\theta)$ in AMR expansion for Pt(5 nm)/Ni(9 nm)/Pt(3 nm) sample. The prefactors of $\cos(2n\theta)$ can be obtained by utilizing Fast Fourier Transform (FFT) algorithm on resistivity data. (b) The significant contributions (only even orders) to the op-AMR have been plotted separately with the experimental data to highlight the role of each contribution.

film is reported by Xiao et al. even at room temperature [12]. From the thickness-dependent measurements, he found that the two-fold and four-fold terms originate from interfaces. As another example, the fourth-order contribution to the AMR has been found in (Ga, Mn)As [122] which is related to the long range ferromagnetic phase at $T < T_C$.

Li et al. have pointed out that the four-fold symmetric AMR of $La_{2/3}Ca_{1/3}MnO_3$ epitaxial films originates from the four-fold symmetry of the lattice [123]. It has to be mentioned that higher order contributions to the op-AMR in polycrystalline structures have not been detected so far. However, the higher order contributions have been observed in this work for all Ni/Pt samples with polycrystalline structure in out-of-plane rotation.

In Eq. 4.7, all the $\cos^{2n}(\theta)$ has the same period (2π) in the expansion. Therefore the coefficients of $\cos^{2n}$ in the fit function may depend on each other. In order to avoid this problem the Fast Fourier Transform (FFT) algorithm has been performed on the resistivity data. Fig. 4.14(a) compares the coefficients of $\cos^{2n}(\theta)$ with $\cos(2n\theta)$ obtained from the fitting with Eq. 4.7 and FFT algorithm, respectively, for Pt(5 nm)/Ni(9 nm)/Pt(3 nm) sample. Due to the imperfect layout of the sample (see Fig. 4.7(b)) the parasitic Hall effect contribution proportional to $\cos(\theta)$ superimposes on the longitudinal resistivity, detected in both expansions and shown in Fig. 4.14(a). The odd contributions (3rd and 5th), Obviously, one order of magnitude smaller than 2nd and 4th orders, thus they may be treated as experimental errors. Using only even coefficients, Fig. 4.14(b) presents the contribution of each order as well as the experimental data of op-AMR measurement (symbols) for Ni/Pt stack with 9 nm Ni thickness. The fourth order contribution, surprisingly, has a negative

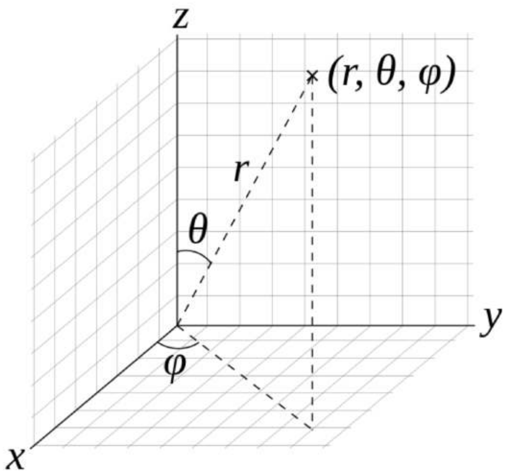

Figure 4.15: Sketch of spherical coordinates with polar angle θ and azimuthal angle φ.

sign and for $t_{\mathrm{Ni}} > 2\,\mathrm{nm}$ it is the dominant coefficient that superimposes the second order, while the sixth order is negligibly small comparing to the other contributions. The second order contribution has a positive value for $t_{\mathrm{Ni}} \leq 30\,\mathrm{nm}$ (see Sec. 4.6). In order to analyze the resistivity behavior, I expand the magnetization dependence of resistivity in spherical coordinates θ and φ is given by

$$\begin{aligned}\rho(\theta,\varphi) =& \rho_{\mathrm{t}} + \underbrace{\Delta\rho_{\mathrm{ip}}^{\mathrm{bulk}}\cos^2\varphi\sin^2\theta + \Delta\rho_{\mathrm{ip}}^{\mathrm{int}}\cos^2\varphi\sin^2\theta +}_{\text{ip-AMR}} \\ &\underbrace{\Delta\rho_{\mathrm{op}}^{\mathrm{bulk}}\cos^2\theta + \Delta\rho_{\mathrm{op}}^{\mathrm{int}}\cos^2\theta}_{\text{2nd order op-AMR}} + \underbrace{\Delta\rho_{\mathrm{op}}^{\mathrm{bulk}}\cos^4\theta + \Delta\rho_{\mathrm{op}}^{\mathrm{int}}\cos^4\theta}_{\text{4th order op-AMR}} + \mathcal{O}(\cos^6)\end{aligned} \tag{4.8}$$

where $\Delta\rho$ coefficients are separated for bulk and interface contributions. In order to find the role of each contribution, it is essential to study the thickness dependence of ip- and op-AMR effects. In the next section the origin of this higher order is studied based on a phenomenological description.

4.5.1 Phenomenological description of angular dependence of resistivity

In order to understand the mechanism related to higher order terms in AMR behavior of Ni/Pt system, it is useful to look at the details of the origin of AMR in ferromagnets. Phenomenologically, AMR shows a twofold symmetry for polycrystalline materials because the magnetocrystalline effect is averaged out. However in single crystals and epitaxial films, it contains higher order terms which reflect the symmetry of the crystals [117]. According to the structural studies on Ni/Pt sandwiches (see Sec. 4.1), the samples are polycrystalline with fcc(111) direction parallel to the film normal in the grains; therefore these (111) out-of-plane textured films can be treated as uniaxial crystal.

Based on the phenomenological expression of Döring [114], the relative change in resistivity for arbitrary current and magnetization directions can be given as

$$\begin{aligned}\frac{\Delta\rho}{\rho_0} = {} & k_1(\alpha_1^2\beta_1^2 + \alpha_2^2\beta_2^2 + \alpha_3^2\beta_3^2 - \frac{1}{3}) \\ & + 2k_2(\alpha_1\alpha_2\beta_1\beta_2 + \alpha_2\alpha_3\beta_2\beta_3 + \alpha_3\alpha_1\beta_3\beta_1) \\ & + k_3(s - \frac{1}{3}) \\ & + k_4(\alpha_1^4\beta_1^2 + \alpha_2^4\beta_2^2 + \alpha_3^4\beta_3^2 + \frac{2}{3}s - \frac{1}{3}) \\ & + 2k_5(\alpha_1\alpha_2\beta_1\beta_2\alpha_3^2 + \alpha_2\alpha_3\beta_2\beta_3\alpha_1^2 + \alpha_3\alpha_1\beta_3\beta_1\alpha_2^2)\end{aligned} \tag{4.9}$$

where $s = \alpha_1^2\alpha_2^2 + \alpha_2^2\alpha_3^2 + \alpha_3^2\alpha_1^2$ and k_i are the magnetoresistance constants. α_i and β_i are the direction cosines of magnetization and current with respect to the cubic axes, respectively.

For our purpose, I adapt Eq. 4.9 to the specific geometry of out-of-plane textured Ni/Pt(111) films using spherical coordinates (see Fig. 4.15) with arbitrary direction of magnetization and current as

$$\begin{aligned} \alpha_1 &= \sin\theta'\cos\varphi' & \beta_1 &= \sin\theta\cos\varphi \\ \alpha_2 &= \sin\theta'\sin\varphi' & \beta_2 &= \sin\theta\sin\varphi \\ \alpha_3 &= \cos\theta' & \beta_3 &= \cos\theta \end{aligned} \tag{4.10}$$

Here z is the direction of film normal and xy plane is the film surface. As the current flows in the film plane, θ should be set as 90°, therefore $\beta_3 = 0$. To sum up the current in the film plane, Eq. 4.9 has to be integrated over φ from 0 to 2π as

$$\begin{aligned}\frac{\Delta\rho}{\rho_0} = & \int_0^{2\pi} [\text{Eq. 4.9}]\ d\varphi \\ = & \pi \Bigg[k_1\left(\sin^2\theta'\cos^2\varphi' + \sin^2\theta'\sin^2\varphi' - \frac{2}{3}\right) \\ & + 2k_3\left(\sin^4\theta'\cos^2\varphi'\sin^2\varphi' + \sin^2\theta'\cos^2\theta'\sin^2\varphi' + \sin^2\theta'\cos^2\theta'\cos^2\varphi' - \frac{1}{3}\right) \\ & + k_4\Bigg(\sin^4\theta'\cos^4\varphi' + \sin^4\theta'\sin^4\varphi' + \frac{4}{3}\sin^4\theta'\cos^2\varphi'\sin^2\varphi' \\ & + \frac{4}{3}\sin^2\theta'\cos^2\theta'\sin^2\varphi' + \frac{4}{3}\sin^2\theta'\cos^2\theta'\cos^2\varphi' - \frac{2}{3}\Bigg)\Bigg]\end{aligned} \tag{4.11}$$

When the magnetization rotates in the film plane (AMR) θ' is 90° and Eq. 4.11 leads to

$$\frac{\Delta\rho}{\rho_0} = C_0 + C_2\cos 2\varphi' + C_4\cos 4\varphi' \tag{4.12}$$

here C_i is a function of k_i and φ' is the angle between magnetization and current direction. Although the fourth order contribution is not observed in Ni/Pt system, Eq. 4.12 is reported and observed in single crystal and epitaxial films in literature quite often [117, 124–126].

On the other hand, when the magnetization is rotated in the plane perpendicular to the current direction (op-AMR), by setting $\varphi' = \pm 90°$, Eq. 4.11 is reduced to

$$\frac{\Delta\rho}{\rho_0} = C_0' + C_2' \cos 2\theta' + C_4' \cos 4\theta' \tag{4.13}$$

here C_0' is the term independent of magnetization direction, $C_2' = -\pi/2\,(k_1 + k_4)$ and $C_4' = -\pi/4\,(k_3 + k_4/6)$ are the prefactors. With ignoring the sixth-order in the experimental data, which is negligibly small comparing to fourth-order, Eq. 4.13 can describe the data very well and is similar to Eq. 4.7 with Fourier transformation. In the following the result of magnetoresistance effects in Ni/Pt samples as a function of Ni thickness is shown and discussed.

4.6 Thickness dependence of MR effects

This section deals with the thickness dependence of MR effects (AMR, op-AMR, SMR, OHE and AHE), which I have investigated in Ni/Pt sandwiches on Si_3N_4 substrate.

4.6.1 Elimination of current shunt through Pt

In order to describe and discuss the MR behavior of Ni in Pt/Ni/Pt sandwiches, it is necessary to find a model that can basically eliminate the Pt-shunt. Moreover, the current that flows through the Pt layers strongly depends on the thickness of Ni layer. By keeping the thickness of Pt layers (5 nm seed and 3 nm cap layer) constant in all samples, it may be practical to consider the system as two parallel resistors. Utilizing the total current $I = I_{\mathrm{Ni}} + I_{\mathrm{Pt}}$ in parallel model, we have

$$\frac{1}{R(t_{\mathrm{Ni}}, \mathbf{M})} = \frac{1}{R_{\mathrm{Ni}}(t_{\mathrm{Ni}}, \mathbf{M})} + \frac{1}{R_{\mathrm{Pt}}} \tag{4.14}$$

where $R(t_{\mathrm{Ni}}, \mathbf{M})$ is the total resistance of the system which is directly obtained from the measurement data according to Eq. 4.4, while $R_{\mathrm{Ni}}(t_{\mathrm{Ni}}, \mathbf{M})$ and R_{Pt} are the pure resistance of Ni and Pt, respectively. Obviously the resistance of Ni depends on the magnetization direction and the thickness of Ni.

On the other hand, it is known since 1901 that the resistivity of a system might be influenced by the reduction of one dimension of the system [127]. Generally if

the thickness of the film is comparable to the mean free path of the electrons in a bulk material, the resistivity increases because of diffusive scattering of electrons at the film surfaces. In 1938, Fuchs introduced a size effect theory for a free electron model based on the Boltzmann transport equation [128]. The theory is developed by Price for ellipsoidal Fermi surfaces [129] and Sondheimer elaborated the Fuchs theory for the explanation of the galvanomagnetic effects [130]. In Fuchs-Sondheimer theory the boundary conditions imposed by the external surfaces are included by the phenomenological specularity parameter p, which describes the fraction of electrons that is scattered elastically at the surface.
On the basis of Fuchs-Sondheimer model, the total film conductivity $\sigma_{m,\mathrm{Ni}}$ of the Ni layer is given by

$$\sigma_{m,\mathrm{Ni}}(t_{\mathrm{Ni}}, p_m, \lambda_{m,\mathrm{Ni\ bulk}}, \sigma_{m,\mathrm{Ni\ bulk}}) = \sigma_{m,\mathrm{Ni\ bulk}} \times \\ \left(1 - \frac{3}{2}\frac{\lambda_{m,\mathrm{Ni\ bulk}}}{t_{\mathrm{Ni}}}(1-p_m)\int_1^\infty dx \frac{(x^{-3}-x^{-5})\left(1-\exp(-\frac{t_{\mathrm{Ni}}}{\lambda_{m,\mathrm{Ni\ bulk}}}x)\right)}{1-p_m\exp(-\frac{t_{\mathrm{Ni}}}{\lambda_{m,\mathrm{Ni\ bulk}}}x)}\right) \tag{4.15}$$

where $\sigma_{m,\mathrm{Ni}} = 1/\rho_{m,\mathrm{Ni}}$ and index $m = t, l, p$ is representative for the magnetization orientation, while $\lambda_{m,\mathrm{Ni\ bulk}}$ is the mean free path of bulk Ni. More details about Fuchs-Sondheimer model can be found in Refs. [11, 77]. In the following the results of combination of Fuchs-Sondheimer model and parallel resistors applied to the experimental data will be discussed.

As the Fuchs-Sondheimer model can be solved only numericaly, it is common to reduce the number of parameters by Eq. 2.19. Here the electron effective density n^* is determined by the normal Hall constant $R_0 = 0.57 \times 10^{-10}$ m^3/C, which I measured according to Fig. 4.11 for the sample with 50 nm Ni thickness. It should be mentioned that the measured Hall constant is similar to $R_0 \simeq 0.6 \times 10^{-10}$ m^3/C obtained by Lavin et al. for bulk Ni at room temperature [64]. With $n^* = 1.1 \times 10^{29}\,\mathrm{m}^{-3}$, we obtain

$$\lambda_{m,\mathrm{Ni\ bulk}} \cdot \rho_{m,\mathrm{Ni\ bulk}} = 555 \times 10^{-18}\ \Omega\mathrm{m}^2 \tag{4.16}$$

where both $\lambda_{m,\mathrm{Ni\ bulk}}$ and $\rho_{m,\mathrm{Ni\ bulk}}$ depend on magnetization direction. It is possible then to eliminate $\lambda_{m,\mathrm{Ni\ bulk}}$ as a variable in fit function 4.15.

Fig. 4.16(a) shows the resistance of the Pt/Ni/Pt structures in transverse field geometry plotted vs Ni thickness. The resistance decreases clearly with increasing Ni thickness, which is known for other ferromagnets' resistance behavior [57, 77, 102, 131]. The red solid line represents the fit according to Eqs. 4.14 and 4.15, which describes the data very well. The parameters obtained from the fit function are summarized in table 4.2.

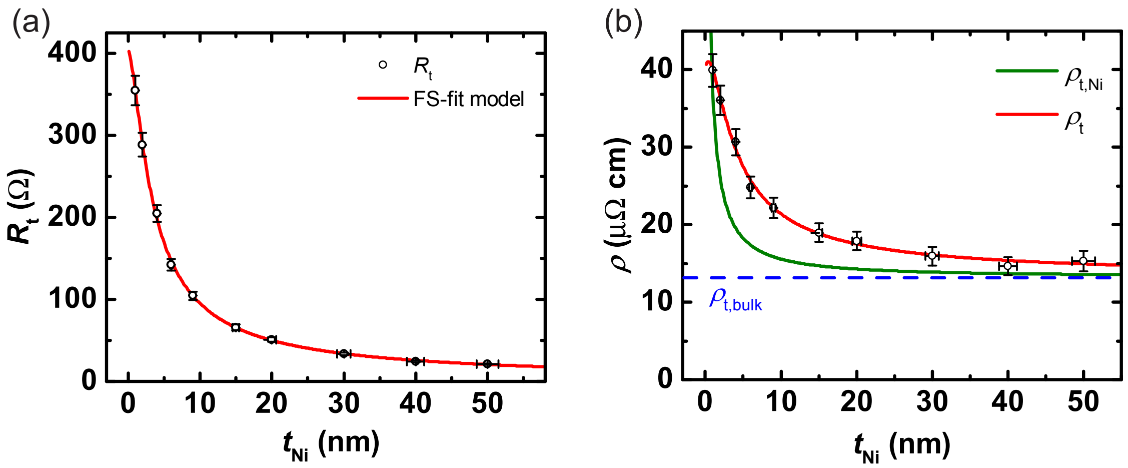

Figure 4.16: (a) Total resistance (transverse) of Ni/Pt layered structures as a function of Ni thickness fitted by Fuchs-Sondheimer model (red line). (b) Indicates the total resistivity of the samples along with the fit calculated from (a). Resistivity of pure Ni is shown as green line which is obtained via Eq. 4.14 and fit parameters.

R_{Pt} (Ω)	ρ_{Pt} (μΩcm)	$\rho_{\mathrm{t,Ni\ bulk}}$ (μΩcm)	p_m
403 ± 7	40.3 ± 0.7	13.1 ± 0.5	≈ 0

Table 4.2: Parameters obtained via combination of Fuchs-Sondheimer and parallel resistors model fitted to experimental data R_{t}.

The calculated resistance for 8 nm Pt in Ni/Pt layered structures (R_{Pt} =(403 ± 7) Ω) is comparable to the Co/Pt samples (R_{Pt} =(385 ± 10) Ω) within the error margin of the measurement [102]. The mean free path of electrons in bulk Ni derived from Eq. 4.16 and the fit parameters is $\lambda_{\mathrm{Ni\ bulk}} = (4.23 \pm 0.20)$ nm. It is less than the lateral grain size (14 ± 2) nm (see Sec. 4.1.1) indicating that the major scattering contributions occur within the grains. Additionally, the specularity parameter p_m obtained from the fit is almost zero, which means nearly all electrons scatter diffusely at the surfaces.

Fig. 4.16(b) shows the total resistivity of samples (black dots) together with fit function (red line) and both of them are calculated from data and fit function in Fig. 4.16(a) ($\rho_{\mathrm{t}} = \frac{w(t_{\mathrm{Ni}}+t_{\mathrm{Pt}})R_{\mathrm{t}}}{l}$). The green line, indicating the resistivity of *pure* Ni, results from the fit parameters and Eq. 4.14, while the blue dashed line shows the resistivity of bulk Ni. Therefore, with the help of the parameters from Table 4.2, it is possible now to calculate the *pure* Ni contributions to the MR effects.

4.6.2 Thickness dependence of AMR and op-AMR

As stated above, in the simple model used to describe the resistivity of the ferromagnetic layer for Ni/Pt structure, I assume the resistance of the system as a parallel circuit. Therefore any changes in MR (i.e., $\Delta\rho_{\mathrm{ip/op}}$), observed on applying external

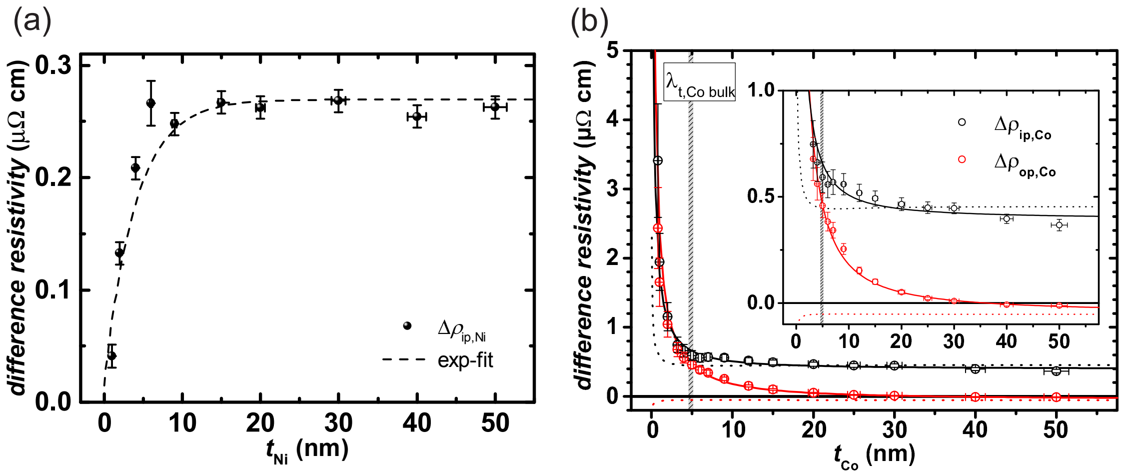

Figure 4.17: (a) The difference resitivity of AMR ($\Delta\rho_{\mathrm{ip,Ni}}$) as a function of Ni thickness. The data is shunt corrected and fitted with exponential model (black dashed line). (b) For comparison $\Delta\rho_{\mathrm{ip/op}}$ of Co/Pt layered structure is displayed from reference [102]. Both AMR and AIMR effects are fitted with FS model (black and red solid lines). The black dashed line is FS model in the absence of interfacial contribution. The inset highlights the results for $t_{\mathrm{Co}} \geq 2\,\mathrm{nm}$.

magnetic field, is due to the change in resistivity of Ni layer. In addition the resistance of Pt layer is assumed to be constant and determined from Fuchs-Sondheimer model (previous section).
In order to determine the difference in resistivity occurring within the Ni layer when changing the magnetization direction, first I calculate the resistivity of the Ni layer for all measured data points (rotation and sweep measurements) via

$$\rho_{\mathrm{Ni}}(t_{\mathrm{Ni}}, \theta, \varphi) = \frac{w \cdot t_{\mathrm{Ni}}}{l} \left(\frac{1}{R(t_{\mathrm{Ni}}, \theta, \varphi)} - \frac{1}{R_{\mathrm{Pt}}} \right)^{-1} \tag{4.17}$$

where $R(t_{\mathrm{Ni}}, \theta, \varphi)$ is attributed to the total resistance of the layers (measured value), $R_{\mathrm{Pt}} = 403\,\Omega$ is obtained from FS model, w and l are, respectively, the width and the length of the wire. To find $\Delta\rho_{\mathrm{ip,Ni}}$ and $\Delta\rho_{\mathrm{op,Ni}}$, the next step is to fit the corresponding rotation data with Eq. 2.23 and 4.8, respectively.

The result of the pure ip-resistivity difference of the Ni layer $\Delta\rho_{\mathrm{ip,Ni}}$ is plotted as a function of Ni layer thickness in Fig. 4.17(a). It is evident that for thicknesses below the mean-free path ($\lambda_{\mathrm{Ni\ bulk}} = (4.23 \pm 0.20)\,\mathrm{nm}$) the AMR rises gradually with t_{Ni} and above $\approx 5\,\mathrm{nm}$ approaches a constant bulk value of $(0.261 \pm 0.007)\,\mu\Omega\mathrm{cm}$. The constant AMR value above 5 nm is consistent with Potter and McGuire whose earlier work indicated no dependence of $\Delta\rho_{\mathrm{ip}}$ on the film thickness in the range of 5 - 200 nm [9]. However, a distinct increase or decrease of the effect has been reported for lower thicknesses in a significant number of literature, so far [77, 102, 132–134]. As an example, Rowan-Robinson et al.

reported a rapid decrease of the AMR ratio and $\Delta\rho_{\mathrm{ip}}$ for Ni films as the film thickness was reduced below 6 nm [133]. They concluded that the loss of AMR is a consequence of enhanced electron-magnon spin-flip scattering in the thinnest films.

In order to describe the AMR behavior I used a phenomenological fit based on exponential law given by

$$\Delta\rho_{\mathrm{ip,Ni}}(t_{\mathrm{Ni}}) = \Delta\rho_{\mathrm{ip,Ni\ bulk}}(1 - \exp(-t_{\mathrm{Ni}}/\xi_{\mathrm{AMR}})) \tag{4.18}$$

where the characteristic length of $\xi_{\mathrm{AMR}} = (4.0 \pm 0.4)\,\mathrm{nm}$ is obtained. The black dashed line on Fig. 4.17(a) indicates the fit to the data. It is seen that the characteristic length is similar to the mean free path determined for the Ni layer. Observing a constant value of AMR for thicknesses above 5 nm is expected due to symmetry reasons when the magnetization is rotated in the film plane. This means that scattering of the electrons at the surfaces plays no role in AMR. However, because of different coordination chemistry at the interfaces, that atoms exhibit comparing to the atoms in Ni layer, it is expected that scattering at the interfaces provides thickness-dependence of $\Delta\rho_{\mathrm{ip}}$.

Moreover, the observed increase of $\Delta\rho_{\mathrm{ip}}$ at low Ni thicknesses may originate from NiPt interdiffusion regions. According to Leroux et al. the resistivity of NiPt alloy at $T = 4\,\mathrm{K}$ follows an inverted parabola (Nordheim's rule) with a maximum at $\approx 45\%$ Ni [135]. As a result it must be expected that the alloyed interface regions provide a higher $\Delta\rho_{\mathrm{ip}}$ compared to the value of Ni layer. Therefore, the NiPt interdiffusion region cannot cause the increase of $\Delta\rho_{\mathrm{ip}}$ at low Ni thicknesses. As the structural properties are also unlikely to be the reason, it might be concluded that increasing of AMR is due to the finite size.

For comparison, the AMR and AIMR (op-AMR) of Co/Pt sandwiches vs Co thickness investigated by A. Kobs, is displayed in Fig. 4.17(b) [102]. It is seen that $\Delta\rho_{\mathrm{ip}}$ decreases with increasing t_{Co} up to 5 nm. The thickness dependence of both effects (shunt corrected) were fitted with FS model reveals that surface contribution plays role in these effects.

Fig. 4.18(a) displays the normalized op-rotation of magnetization for all thicknesses in a polar diagram. All the samples are fitted according to Eq. 4.7. For $t_{\mathrm{Ni}} \leq 4\,\mathrm{nm}$ the second order contribution is positive and larger than the 4th order. Therefore, the behavior of the first two samples ($t_{\mathrm{Ni}} \leq 4\,\mathrm{nm}$) are qualitatively similar to each other and different from the others. This is due to the difference in sign and amplitude of $\Delta\rho_{\mathrm{op,2n}}$ for different thicknesses.

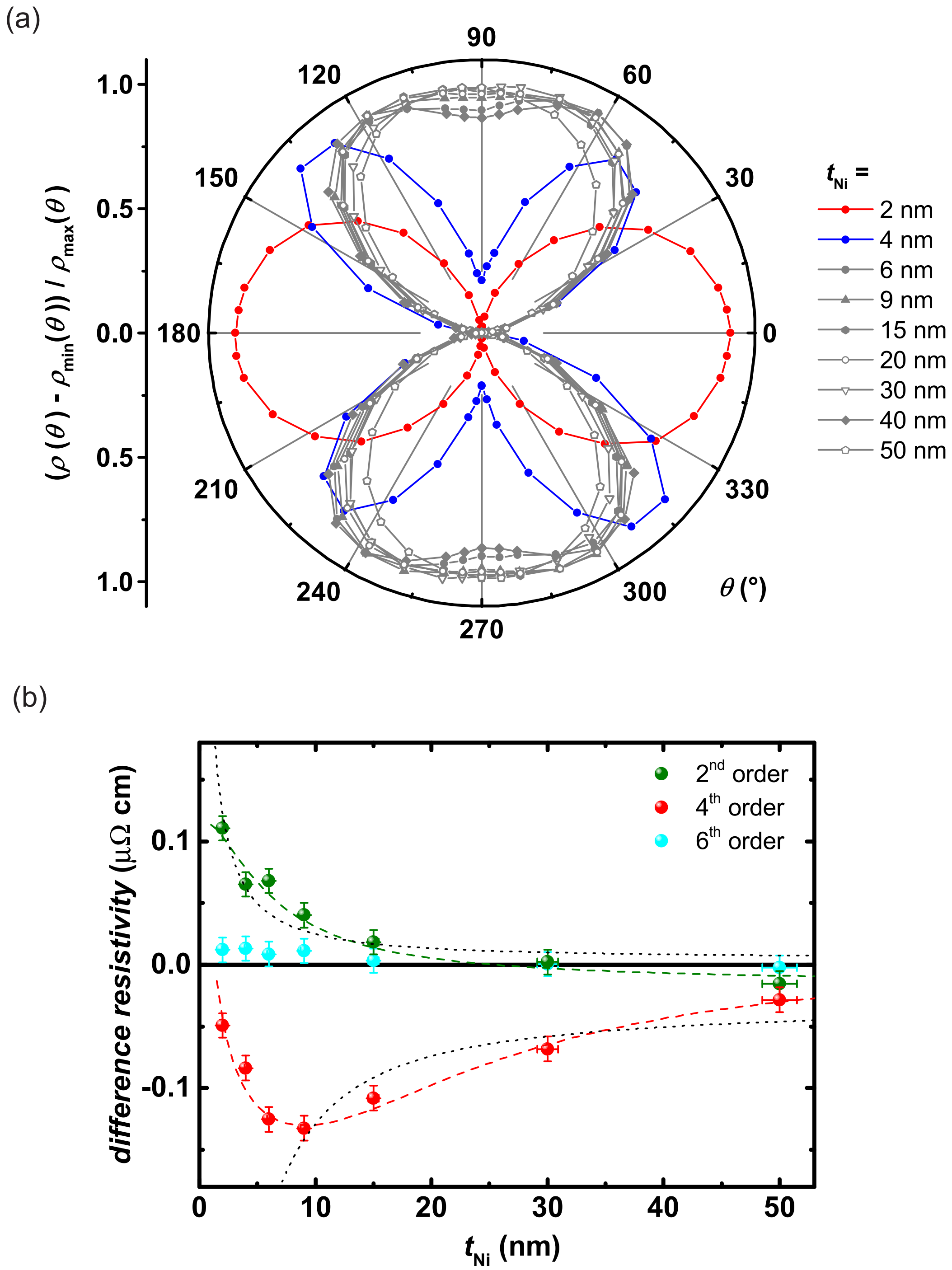

Figure 4.18: (a) Angular dependence of out-of-plane AMR for different thicknesses of Pt/Ni/Pt layered structure in normalized polar diagram. For $t_{\mathrm{Ni}} \leq 4\,\mathrm{nm}$ the second order of $\Delta\rho_{\mathrm{op}}$ is larger than the fourth order contribution. (b) Higher order contributions of $\Delta\rho_{\mathrm{op,Ni}}$ as a function of Ni thickness. The dashed lines (red and green) are the fit results using Eq. 4.19. The black dashed lines are FS model which cannot describe the experimental data. The data is shunt corrected and reflects the resistivity difference of the Ni layer only.

In the following the thickness dependence of $\Delta\rho_{\mathrm{op,2n}}$ is discussed.

Fig. 4.18(b) presents the thickness dependence of higher order contributions to the op-AMR for Pt/Ni/Pt films. It should be recalled that the out-of-plane rotation of magnetization measurements were also corrected for Pt-shunt according to Eq. 4.17. Although the sixth order contribution exists in the whole range of t_{Ni}, it is negligibly small and does not show a significant trend vs Ni thickness. Therefore I consider just the second and fourth orders in the following discussion.

As we can see $\Delta\rho_{\mathrm{op}}^{\mathrm{2nd}}$ decreases gradually and obtains negative values for $t_{\mathrm{Ni}} \gtrsim 30\,\mathrm{nm}$. Qualitatively, $\Delta\rho_{\mathrm{op}}^{\mathrm{2nd}}$ curve shows a $1/t_{\mathrm{Ni}}$ behavior similar to Co/Pt layered structure [102] (see red symbols in Fig. 4.17(b)) and Co/Pd structure [77]. For the whole range of Ni thickness $\Delta\rho_{\mathrm{op,Ni}}^{\mathrm{4th}}$ is a dominant contribution with negative values. The absolute value of fourth order increases with t_{Ni} up to 9 nm and from this point decreases monotonically. It seems that both orders are dominated by interface effect above $t_{\mathrm{Ni}} = 9\,\mathrm{nm}$ because of $1/t_{\mathrm{Ni}}$-behavior. Therefore, the Fuchs-Sondheimer model was used to fit the data, while a difference in specularity parameters Δp_{op} was set as fit parameters. The black dashed lines in Fig. 4.18(b) shows the fit based on FS-model. Clearly the fit cannot describe the data particularly for low thickness due to suppression of both orders in low thicknesses similar to AMR (fitted with exponential model). This point was the motivation to use an exponential term in Fuchs-Sondheimer model. The green and red dashed lines in Fig. 4.18(b) present the phenomenological model given by

$$\Delta\rho_{\mathrm{op,Ni}}^{\mathrm{2n}}(t_{\mathrm{Ni}}) = (1 - \exp(-t_{\mathrm{Ni}}/\xi_{\mathrm{AIMR}})) \times \text{FS model} \tag{4.19}$$

where ξ is again the characteristic length and $\Delta\rho_{\mathrm{op,Ni}}(t_{\mathrm{Ni}})$ in FS model is defined as

$$\Delta\rho_{\mathrm{op,Ni}}(t_{\mathrm{Ni}}) = \rho_{\mathrm{p,Ni}}(t_{\mathrm{Ni}}, p_{\mathrm{p}}, \lambda_{\mathrm{p,Ni\ bulk}}) - \rho_{\mathrm{t,Ni}}(t_{\mathrm{Ni}}, p_{\mathrm{t}}, \lambda_{\mathrm{t,Ni\ bulk}}) \tag{4.20}$$

Here an anisotropy in the interfacial specularity parameter $\Delta p_{\mathrm{op}} = p_{\mathrm{t}} - p_{\mathrm{p}}$ is taken as a fit parameter.
The fit parameters obtained from the applied model are summarized in table 4.3.

	Δp_{op}	$\Delta\rho_{\mathrm{op,bulk}}$ (µΩcm)	ξ_{AIMR} (nm)
2nd order	(0.019 ± 0.007)	(-0.017 ± 0.008)	(4.1 ± 2.1)
4th order	(-0.12 ± 0.04)	(-0.735 ± 0.070)	(5.3 ± 1.0)

Table 4.3: The fit parameters to the op-AMR obtained from phenomenological model according to Eq. 4.19.

This model can describe both orders better than FS-model. Similar to AMR, the characteristic lengths obtained for both orders are in the range of mean free path

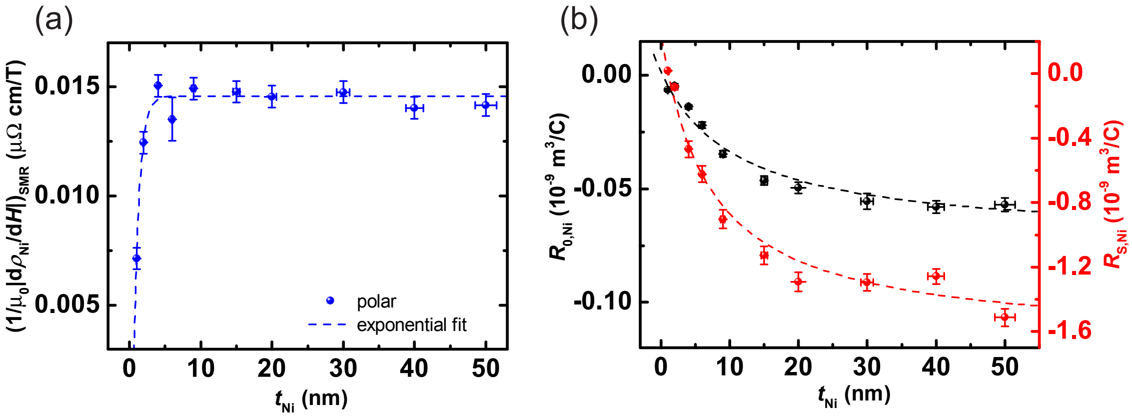

Figure 4.19: (a) Thickness dependence of the shunt corrected spin disorder magnetoresistance (SMR) effect obtained from the polar MR sweep measurements. The dashed line is an exponential fit to the data. (b) Thickness dependence of ordinary and anomalous Hall constants calculated from R_{xy} of Pt/Ni/Pt system. The dashed lines are $1/t_{\mathrm{Ni}}$ fit to the data.

of bulk Ni ($\lambda_{\mathrm{Ni\ bulk}} = (4.23 \pm 0.20)\,\mathrm{nm}$). The difference in the specularity parameters for magnetization orientations transverse and polar confirms the existence of interface contribution in both orders (AIMR), while the suppression of both contributions at low thicknesses reveals the presence of finite size effects (similar to AMR). Moreover, the non-vanishing $\Delta\rho_{\mathrm{op}}^{\mathrm{2n}}$ at high thicknesses reveals that the so-called geometrical size effect (bulk effect) superimposes the AIMR. I should recall that GSE is a crystalline AMR contribution that is a consequence of the texture of the films (see Sec. 2.2.3).

4.6.3 Thickness dependence of SMR, OHE and AHE constants

In this section the results of magnetoresistance effects obtained from longitudinal and transverse field sweep measurements are presented. In order to disentangle ρ_{xx} of Ni layer from Ni/Pt layered structure, Eq. 4.17 was applied on the longitudinal sweep measurements. With the simple parallel model (Eq. 4.17) it is impossible to subtract Pt resistance from the the total resistance of the films in transverse sweep measurements (R_{xy}). Therefore, the results (Hall constants) related to R_{xy} are not shunt corrected.

As stated in Sec. 4.4, all Ni/Pt stacks show similar longitudinal field sweep behavior in high field as the one showed in Fig. 4.9 for all three generic geometries ($\mathrm{H}_{\|}$, H_{t} and H_{p}). The strength of spin-disorder MR effect (SMR) can be determined from the slope of high field resistivity $\frac{1}{\mu_0}\left|\mathrm{d}\rho_{\mathrm{Ni}}/\mathrm{d}H\right|_{\mathrm{SMR}}$, which is almost the same in all geometries.

Fig. 4.19(a) displays the SMR effect as a function of Ni thickness. Qualitatively, SMR presents similar behavior as AMR (Fig. 4.17). It means that SMR increases with increasing t_{Ni} up to $t_{\mathrm{Ni}} = 4\,\mathrm{nm}$ while for thicknesses above 4 nm it exhibits a constant value of $\frac{1}{\mu_0}\left|\mathrm{d}\rho_{\mathrm{Ni}}/\mathrm{d}H\right|_{\mathrm{SMR}} = (0.014 \pm 0.001)\,\mu\Omega\mathrm{cm}$. Similar to the AMR the thickness dependence of the SMR can be phenomenologically described by an exponential law as

$$\frac{1}{\mu_0}\left|\mathrm{d}\rho_{\mathrm{Ni}}/\mathrm{d}H\right|_{\mathrm{SMR}}(t_{\mathrm{Ni}}) = \frac{1}{\mu_0}\left|\mathrm{d}\rho_{\mathrm{Ni,bulk}}/\mathrm{d}H\right|_{\mathrm{SMR}}\left(1 - \exp\left(-t_{\mathrm{Ni}}/\xi_{\mathrm{SMR}}\right)\right) \tag{4.21}$$

where ξ_{SMR} is the characteristic length and is about $(0.76 \pm 0.13)\,\mathrm{nm}$, which is smaller than for the AMR. Raquet et al. reported in their publication that SMR is almost thickness-independent for Fe, Co, and Ni epitaxial thin films in the range of 7 to 80 nm [76]. This is consistent with the result found for Ni/Pt above 4 nm. Moreover, the structural changes cannot be a reason for the thickness dependence of the SMR as structural variations were not observed in Ni/Pt system and according to Raquet et al. cannot influence SMR significantly [76]. Therefore, the thickness dependence of the SMR might be caused by suppression of electron-magnon scattering at low Ni thicknesses.

Besides SMR effect, Fig. 4.19(b) also presents the ordinary and the anomalous Hall constants versus Ni thickness. It was explained in Sec. 4.4 that R_0 and R_S are calculated from R_{xy} measurement according to the following equations.

$$\begin{aligned} R_0 &= t_{\mathrm{Ni}} \cdot s_{\mathrm{OHE}} \\ R_S &= \frac{\Delta R_{\mathrm{AHE}} \cdot t_{\mathrm{Ni}}}{2\mu_0 M_S} \end{aligned} \tag{4.22}$$

where t is the Ni thickness of the sample and $\mu_0 M_{\mathrm{S}} = 0.62\,\mathrm{T}$ is provided from Ref. [98]. For all thicknesses R_0 (black symbol) is negative, which is also the case for pure Ni and Pt (electron-type) [67]. The ordinary Hall constant decreases slightly with increasing t_{Ni} and merges into a constant value of $R_{0,\mathrm{Ni\ bulk}} = (-0.055 \pm 0.003) \times 10^{-9}\,\mathrm{m}^3/\mathrm{C}$ for thicknesses above 20 nm. This is one order of magnitude larger than for Pt ($R_{0,\mathrm{Pt\ bulk}} \approx -0.06 \times 10^{-10}\,\mathrm{m}^3/\mathrm{C}$). An increase of OHE constant with decreasing Ni thickness in the range of $t_{\mathrm{Ni}} < 20\,\mathrm{nm}$ has been reported by Reimer, Ghosh, Wedler [136–139].

On the other hand $R_S(t_{\mathrm{Ni}})$ shows a similar behavior versus t_{Ni} as the ordinary Hall constant and is a negative value for all thicknesses. Here, for $t_{\mathrm{Ni}} \geq 20\,\mathrm{nm}$ AHE follows the constant value of $\approx (-1.45 \pm 0.05) \times 10^{-9}\,\mathrm{m}^3/\mathrm{C}$. This behavior can be attributed to the thickness-dependent current shunt through Pt layers. It was reported also by Gerber et al. that the AHE of Ni films in the thickness range of 5 - 100 nm increases significantly with decreasing the thickness [72, 140, 141].

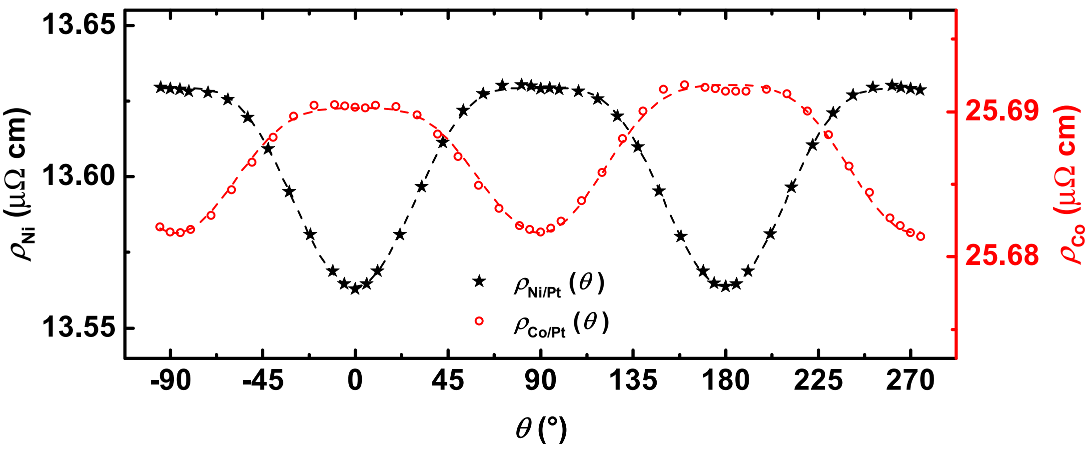

Figure 4.20: Comparing the angular dependence of resistivity of Pt(5 nm)/Ni(30 nm)/Pt(3 nm) (black symbols) with Pt(5 nm)/Co(30 nm)/Pt(3 nm) (red symbols). Both data sets are corrected for the current shunt through Pt. Higher order contributions exist in Co/Pt as well but they are one order of magnitude smaller than Ni/Pt.

In the following section investigation of higher order contributions to the op-AMR in other systems like Co/Pt and Ni/Pd are presented.

4.7 Higher order contributions in $\rho(\theta)$ for Co/Pt and Ni/Pd

In the previous section, I presented the thickness dependence of magnetoresistance effects for pure Ni in Ni/Pt structure and the result were discussed. Importantly, I observed for the first time the higher order contributions to the op-AMR in Pt/Ni/Pt layered structure. Moreover, Ni/Pt results were compared with Co/Pt sandwiches studied by A. Kobs [11]. Finding higher order contributions of $\rho(\theta)$ in Ni/Pt was the main reason, which draw my attention to search for higher orders in Co/Pt samples as well.

As we can see in Fig. 4.17(b), the thickness dependence of AIMR calculated for pure Co shows that $\Delta\rho_{\mathrm{op}}$ is almost zero around $t_{\mathrm{Co}} = 35$ nm. In the thickness range around 35 nm, due to the suppression of second order, it is more likely to detect higher order contributions to AIMR in Co/Pt, if there are any. Therefore, I have chosen a Co/Pt sample with 30 nm Co thickness to have a comprehensive study of possible higher orders.

Fig. 4.20 presents the angular dependence of op-AMR for both Ni/Pt (black symbols) and Co/Pt (red symbols) with thickness of 30 nm of the ferromagnet. Appar-

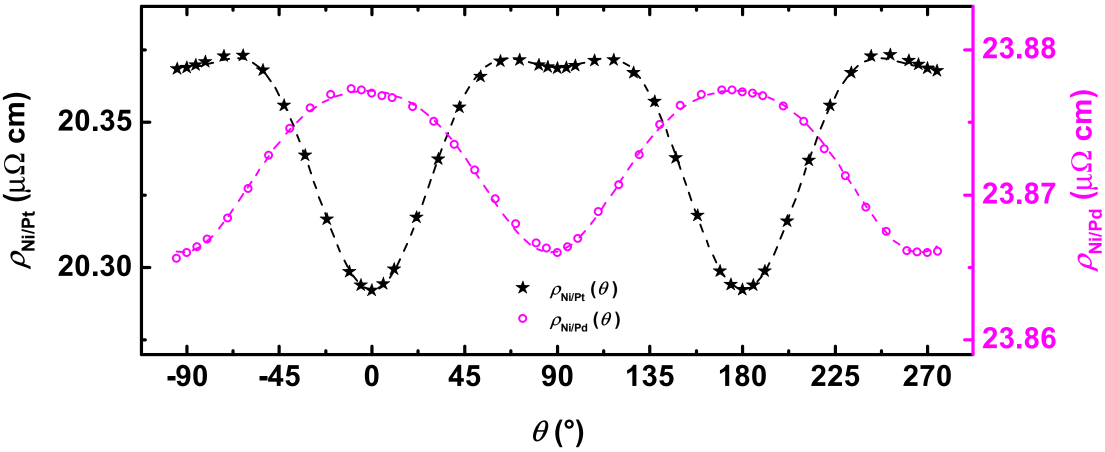

Figure 4.21: Comparison between the angular dependence of resistivity of Pt(5 nm)/Ni(9 nm)/Pt(3 nm) (black symbols) and Pd(5 nm)/Ni(9 nm)/Pd(3 nm) (pink symbols) for out of plane rotation of magnetization. The dashed lines are fits to the data. The second and fourth order contributions to the op-AMR in Ni/Pd exist but they are significantly smaller than similar contribution for Ni/Pt.

ently the trace of higher order contributions in Co/Pt resistivity is detectable at the first glance. The dashed line is the fit to the data according to Eq. 4.7.
The fit parameter on Co/Pt shows that $\Delta\rho^{4\mathrm{th}}_{\mathrm{op,Co}} = -0.008\,\mu\Omega\mathrm{cm}$ which is one order of magnitude smaller than $\Delta\rho^{4\mathrm{th}}_{\mathrm{op,Ni}} = -0.068\,\mu\Omega\mathrm{cm}$ for the Ni/Pt sample. However the fourth order contribution in both cases has a negative sign.
On the other hand, comparing the second order contribution in Ni/Pt and Co/Pt reveals that $\Delta\rho^{2\mathrm{nd}}_{\mathrm{op,Co}}$ is one order of magnitude larger than the second order contribution in nickel. Therefore, the higher order contributions to the AIMR effect in Pt/Co/Pt are generally overcompensated by the dominant second order contributions and are difficult to detect experimentally.

	$\Delta\rho^{2\mathrm{nd}}_{\mathrm{op}}$ (μΩcm)	$\Delta\rho^{4\mathrm{th}}_{\mathrm{op}}$ (μΩcm)	$\Delta\rho^{4\mathrm{th}}_{\mathrm{op}}/\Delta\rho^{2\mathrm{nd}}_{\mathrm{op}}$
Ni(30 nm)/Pt	0.002	−0.068	≈ 34
Co(30 nm)/Pt	0.018	−0.008	≈ 0.4
Ni(9 nm)/Pt	0.038	−0.113	≈ 3
Ni(9 nm)/Pd	0.017	−0.006	≈ 0.3

Table 4.4: Comparing higher order contributions to the op-AMR in Ni/Pt, Co/Pt, and Ni/Pd layered structures.

Finding higher order contribution to the op-AMR in Co/Pt samples leads to the question if the element (ferromagnet; Ni or Co) or the stacking of iso-electronic materials is the driving force for the prominent role of higher orders in the interfacial AMR. In order to answer this question study of the other iso-electronic system like

Ni/Pd was preformed. One Pd(5 nm)/Ni(9 nm)/Pd(3 nm) sample was sputtered and prepared with the same procedure as Ni/Pt specimens on Si_3N_4 substrate.

Fig. 4.21 shows the result of op-AMR measurement of Ni/Pd (pink symbols) and Ni/Pt (black symbols) with 9 nm Ni layer. Even though the angular dependence shows different trend, higher orders, obviously, exist in Ni/Pd sandwich. Comparing the results, both $\Delta\rho_{\mathrm{op}}^{\mathrm{2nd}}$ and $\Delta\rho_{\mathrm{op}}^{\mathrm{4th}}$ are significantly smaller in Ni/Pd than in Ni/Pt. This can be attributed to the difference in atomic number (Z) of Pd and Pt, since spin-orbit interaction (SOI) is proportional to Z^4 (see Eq. 2.4). In a related work it was found by Lee et al. that $\Delta\rho_{\mathrm{op}}$ is smaller for Co/Pd than Co/Pt layered structures [61]. The measured values of higher order contributions to the op-AMR in Ni/Pt, Co/Pt, and Ni/Pd are listed in Tab. 4.4. From the obtained values for $\left|\Delta\rho_{\mathrm{op}}^{\mathrm{4th}}/\Delta\rho_{\mathrm{op}}^{\mathrm{2nd}}\right|$ it is concluded that the iso-electronic stacking plays a prominent role of higher orders in the interfacial AMR.

In the following section, I study the temperature dependence of resistiviy of Ni/Pt thin films in the temperature range of 2 - 300 K.

4.8 Temperature dependence of ρ(M,H) in Ni/Pt layered structures

The relatively low Curie temperature of Ni of ≈ 630 K allows us to study nickel in a wide range of temperature, in comparison to other ferromagnetic materials like Co and Fe [142]. As we have seen in chapter 2, the main sources of the temperature dependence of the resistivity in 3d transition metals are scattering of conduction s-electrons at phonons and their interaction with the magnetic spin system (spin-disorder resistivity). Based on Matthiessen's rule, the electrical resistivity has contributions from static disorder, i.e. the residual resistivity (ρ_{st}), the electron-phonon scattering (ρ_{ph}), and the spin-disorder resistivity (ρ_{mag}) (see Eq. 2.20). In order to determine the individual contributions in Pt/Ni/Pt sandwiches, the resistivity was measured while the temperature was swept from 4.2 - 300 K. All the temperature dependence experiments of the following section have been performed in the Spectromag setup (see Sec. 3.2.2).

In the following, first the result of the temperature dependence of resistivity at zero field and, second, the temperature dependence of the magnetotransport properties found in Ni/Pt are discussed.

4.8.1 Temperature dependence of zero-field resistivity

Fig. 4.22 shows the temperature dependence of resitivity for Pt/Ni/Pt layered structure with $t_{\mathrm{Ni}} = 6$ and 50 nm, which is measured without external field. Clearly, both samples display similar behaviors, namely from about 50 K on the resisitivity increases monotonically with temperature up to 300 K. The residual resistivity ratio

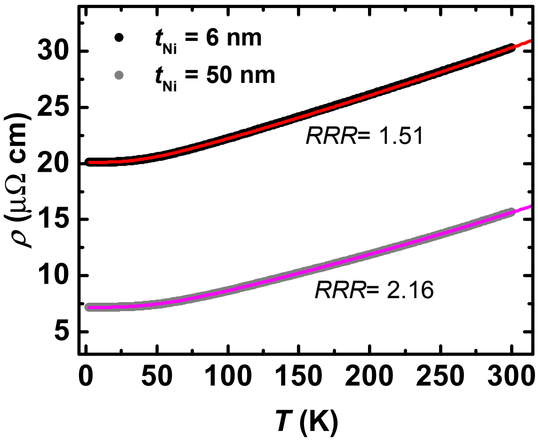

Figure 4.22: Temperature dependence of the resistivity for Pt/Ni/Pt layered structure with $t_{\mathrm{Ni}} = 6$ and 50 nm. The red and pink lines are fits to the data according to Eq. 4.24, 4.25, and 4.26.

(RRR) which is defined as the ratio of resistivity of a material at room temperature and at liquid Helium temperature:

$$RRR = \frac{\rho_{\mathrm{T=295\ K}}}{\rho_{\mathrm{T=4.2\ K}}} \tag{4.23}$$

is calculated as $RRR = 1.51$ for $t_{\mathrm{Ni}} = 6$ nm and $RRR = 2.16$ for $t_{\mathrm{Ni}} = 50$ nm, shown in Fig. 4.22. The RRR value for a single material depends on the amount of impurities and other crystallographic defects [143]. Since resistivity usually increases as defect increases, a large RRR is associated with a pure sample. Comparing RRR of Ni/Pt with Co/Pt sandwiches ($1.28 \leq RRR_{\mathrm{Co/Pt}} \leq 1.50$) [11] shows that the obtained value for $RRR_{\mathrm{Ni/Pt}}$ is almost similar to Co/Pt samples. This indicates that the structural disorder in both sandwiches is similar.

The red and pink solid lines are the fit function to the data. In the following I introduce the applied model. In order to obtain a suitable model, first it has to be mentioned that the system consists of two parallel resistance as

$$R(t_{\mathrm{Ni}}, T) = \left(\frac{1}{R_{\mathrm{Ni}}(t_{\mathrm{Ni}}, T)} + \frac{1}{R_{\mathrm{Pt}}(T)}\right)^{-1} \tag{4.24}$$

Mentioned before (Sec. 2.2), the resistance of Ni and Pt can be described separately according to Matthiessen's rule as follows

$$R_{\mathrm{Pt}}(T) = R_{\mathrm{st,Pt}} + \underbrace{\widetilde{A}_{\mathrm{el\text{-}ph,Pt}} \left(\frac{T}{\Theta_{\mathrm{D,Pt}}}\right)^{n_{\mathrm{Pt}}} \int_0^{\Theta_{\mathrm{D,Pt}}/T} \frac{x^{n_{\mathrm{Pt}}} dx}{(e^x - 1)(1 - e^{-x})}}_{R_{\mathrm{ph,Pt}}(T)}, \ n_{\mathrm{Pt}} = 3.7 \tag{4.25}$$

$$R_{\mathrm{Ni}}(T) = R_{\mathrm{st,Ni}} + \underbrace{\widetilde{\alpha}_{\mathrm{Ni}} T^2}_{R_{\mathrm{mag,Ni}}(T)} + \underbrace{\widetilde{A}_{\text{el-ph,Ni}} \left(\frac{T}{\Theta_{\mathrm{D,Ni}}}\right)^{n_{\mathrm{Ni}}} \int_0^{\Theta_{\mathrm{D,Ni}}/T} \frac{x^{n_{\mathrm{Ni}}}\,dx}{(e^x-1)(1-e^{-x})}}_{R_{\mathrm{ph,Ni}}(T)}, \quad n_{\mathrm{Ni}} = 3.1 \tag{4.26}$$

Here for the phonon contribution, I use the constants $n_{\mathrm{Ni}} = 3.1$ and $n_{\mathrm{Pt}} = 3.7$ which were found for bulk Ni and Pt [144]. In addition, for the Debye temperatures of Ni and Pt the bulk values $\Theta_{\mathrm{D,Ni}} = 390\,\mathrm{K}$ and $\Theta_{\mathrm{D,Pt}} = 225\,\mathrm{K}$ are applied [144]. To further reduce the number of fit parameters the resistance of Pt at room temperature, determined in Sec. 4.6.1 ($R_{\mathrm{Pt}}(T = 295\,\mathrm{K}) = (403 \pm 7)\,\Omega$) was used. Clearly, the model describes the experimental data very well.

The results of applying the fit to the measured $R(T)$ according to Eqs. 4.24, 4.25 and 4.26 are given in Tab. 4.5.

t_{Ni} (nm)	$\rho_{\mathrm{st,Pt}}$ (µΩcm)	$A_{\text{el-ph,Pt}}$ (µΩcm)	$\rho_{\mathrm{st,Ni}}$ (µΩcm)	$A_{\text{el-ph,Ni}}$ (µΩcm)	α_{Ni} (µΩcm/K^2)
6	27.9 ± 2	26.1 ± 2	14.6 ± 2	14.2 ± 1	$(0.4 \pm 0.2) \times 10^{-4}$
50	28.0 ± 2	25.9 ± 2	6.4 ± 2	15.0 ± 1	$(0.3 \pm 0.2) \times 10^{-4}$

Table 4.5: The intrinsic parameters, obtained by the fitting procedure of $R(T)$ curves for Pt/Ni/Pt with $t_{\mathrm{Ni}} = 6$ and 50 nm.

The intrinsic values have been calculated from the fit parameters according to $\rho_{\mathrm{st},i} = R_{\mathrm{st},i} \cdot \frac{w \cdot t_i}{l}$, $A_{\mathrm{ph},i} = \widetilde{A}_{\mathrm{ph},i} \cdot \frac{w \cdot t_i}{l}$, and $\alpha_{\mathrm{Ni}} = \widetilde{\alpha}_{\mathrm{Ni}} \cdot \frac{w \cdot t_i}{l}$, where l and w are the dimensions of the sample and t_i is the layer thickness. The results found for Pt-parameters, $\rho_{\mathrm{st,Pt}}$ and $A_{\text{el-ph,Pt}}$, are nearly the same for both samples within the error margin of the experiment, which means that there is no dependency on t_{Ni} observed. This is expected since the Pt layers (seed and cap layer) have the same thickness in both samples. In contrast to the results of Pt layer, the residual resistivity of the Ni layer $\rho_{\mathrm{st,Ni}}$ increases with decreasing Ni thickness by a factor of two, while the obtained values of $A_{\text{el-ph,Ni}}$ and α_{Ni} for both samples are almost similar.

Additionally, the temperature-dependent part of the resistivity $\rho_{\mathrm{ph,Pt}}(T)$ and $\rho_{\mathrm{ph,Ni}}(T) + \rho_{\mathrm{mag,Ni}}(T)$ for $t_{\mathrm{Ni}} = 50\,\mathrm{nm}$ are calculated and shown in Fig. 4.23. For comparison the experimental results for bulk Pt and Ni reported by White and Woods [144] are plotted as well. Utilizing Eq. 4.25 in Fig. 4.23(a) for bulk Pt (black line) the fit parameter $A_{\text{el-ph,Pt}} = 22\,\mu\Omega\mathrm{cm}$ was obtained, which is smaller than the calculated value for $t_{\mathrm{Pt}} = 8\,\mathrm{nm}$ (see Tab. 4.5). Similar to the result of Pt, $\rho_{\mathrm{ph,Ni}}(T) + \rho_{\mathrm{mag,Ni}}(T)$ of bulk Ni is fitted according to Eq. 4.26. The fit parameters $A_{\text{el-ph,Ni}} = 8.6\,\mu\Omega\mathrm{cm}$ and $\alpha_{\mathrm{Ni}} = 0.5 \times 10^{-4}\,\mu\Omega\mathrm{cm/K^2}$ are obtained. Decreasing

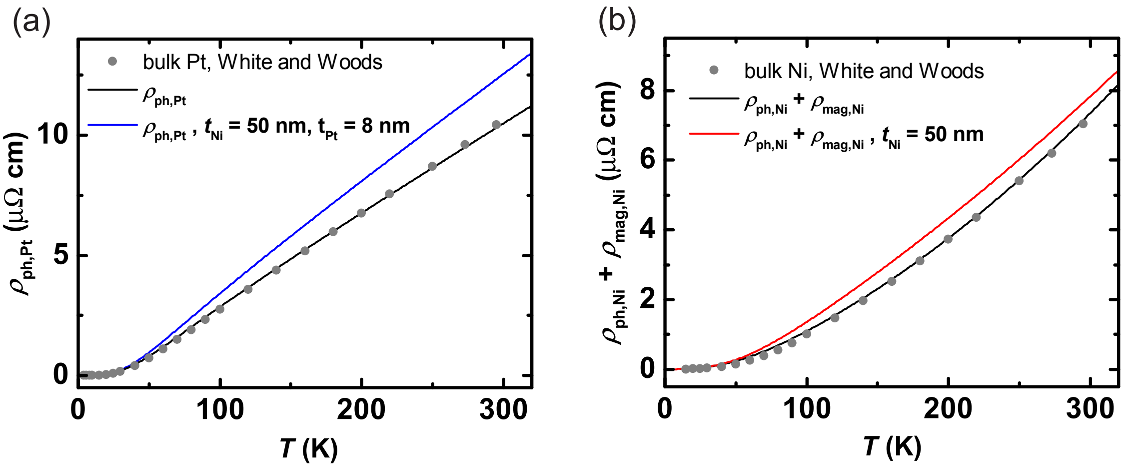

Figure 4.23: Temperature-dependent part of the resistivity (a) $\rho_{\mathrm{ph,Pt}}(T)$ and (b) $\rho_{\mathrm{ph,Ni}}(T) + \rho_{\mathrm{mag,Ni}}(T)$ calculated for $t_{\mathrm{Ni}} = 50\,\mathrm{nm}$ according to Eqs. 4.25 and 4.26. The experimental results of White and Woods [144] for bulk Pt and Ni are shown for comparison.

of $A_{\text{el-ph}}$ with increasing Ni layer thickness is in accordance with the observations of Kim et al. [145]. They explained this enhancement of electron-phonon constant with the presence of additional surface phonon modes which is decaying fast into the bulk material. The reported values of α_{Ni} for bulk Ni are smaller than the measured value for Pt/Ni/Pt sandwiches and are in the range of $0.09 - 0.16 \times 10^{-4}\,\mu\Omega\mathrm{cm/K}^2$ [74, 146–148].

In Ref. [11] the temperature dependence of resistivity has been investigated and discussed for three Pt/Co/Pt sandwiches with $t_{\mathrm{Co}} = 2$, 6 and 20 nm. Comparing the result of Ni/Pt with Co/Pt layered structure shows that the Pt-parameters are in good agreement with each other revealing that Pt layers in both systems grow similarly. In addition, $\rho_{\mathrm{st,Co}}$ decreases with increasing t_{Co} similar to the result of Ni/Pt, although the obtained value for Ni/Pt is much smaller than for Co/Pt with similar ferromagnet thickness.

4.8.2 Temperature dependence of resistivity on applied field

In order to investigate the higher order contribution to the op-AMR found in Ni/Pt sandwiches below the room temperature, I measured the magnetoresistance curves of the sample with $t_{\mathrm{Ni}} = 50\,\mathrm{nm}$ in temperature range of $4.2 < T < 300$ K. Fig. 4.24(a) displays the sweep measurements of Pt(5 nm)/Ni(50 nm)/Pt(3 nm) sandwich at $T = 4.2\,\mathrm{K}$ revealing the same hierarchy $\rho_{\mathrm{p}} < \rho_{\mathrm{t}} < \rho_{\parallel}$ than at room temperature (Fig. 4.9). However, above technical saturation, instead of a linear decrease of the resistivity with increasing the absolute value of the applied field, the resistivity is almost constant in all three geometries. This isotropic behavior is typical for the SMR effect.

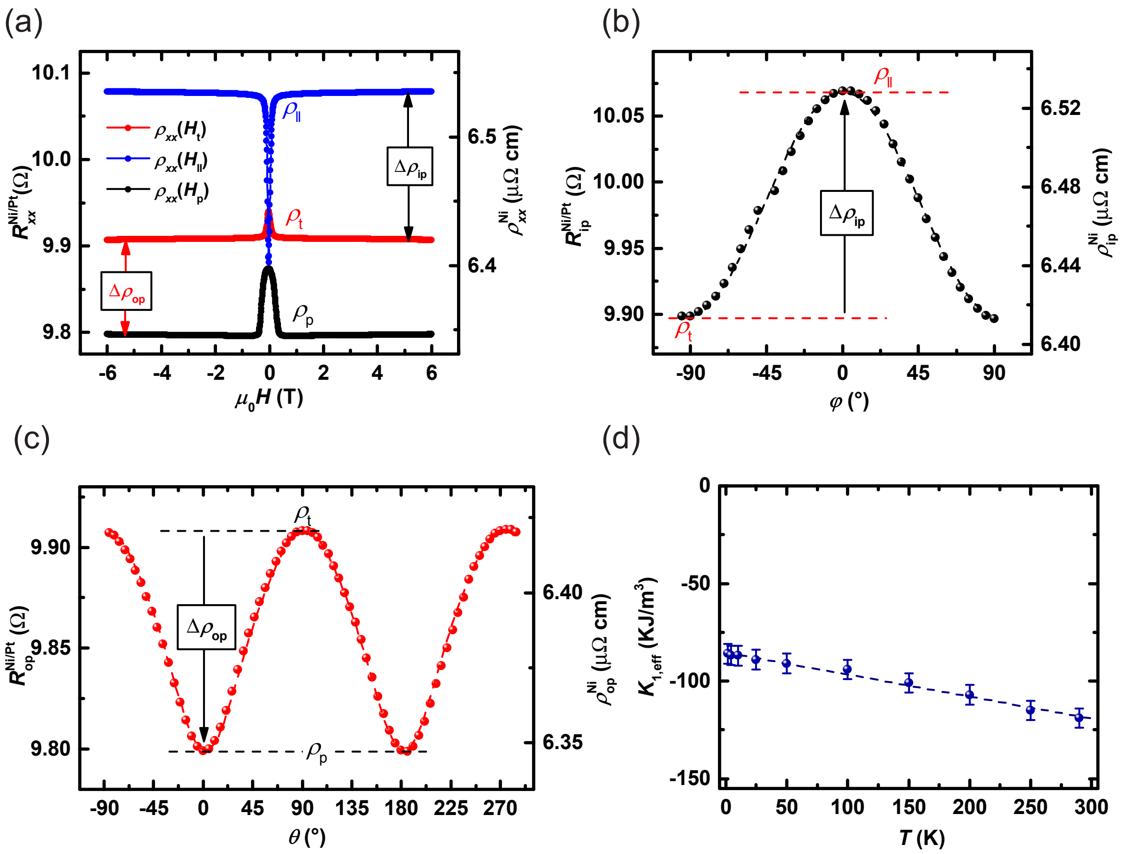

Figure 4.24: Magnetoresistance measurement of Pt(5 nm)/Ni(50 nm)/Pt(3 nm). (a) Typical field sweep measurements, (b) and (c) in- and out-of-plane rotation of magnetization measurements at $T = 4.2\,\mathrm{K}$. The dashed lines are fits to the data according to Eq. 4.7. (d) Temperature dependence of the effective first order anisotropy constant $K_{1,\mathrm{eff}}$ for the same sample.

Fig. 4.24(b) and (c) present the dependence of the resistivity with respect to the orientation of magnetization measured for the same sample at $T = 4.2\,\mathrm{K}$. The in-plane rotation of magnetization shows a $\cos^2$ behavior, while the higher order contribution to the out-of-plane curve is observed according to Eq. 4.7, similar to the room temperature results. It reveals that higher order contributions to the op-AMR exist at low temperatures as well.

Moreover, the anisotropy constant of the same sample was determined from $\rho_{xy}(H_\mathrm{p})$ curves according to the procedure explained in Sec. 4.3. As the second order contribution to the anisotropy constant K_2 does not change with temperature within the error margins of the experiment, similar to the investigation at room temperature I set K_2 to zero. Fig. 4.24(d) shows the effective first order anisotropy constant $K_{1,\mathrm{eff}}$ in dependence of temperature for the sample with 50 nm Ni thickness. It is seen that $K_{1,\mathrm{eff}}(T)$ decreases linearly with temperature. In the temperature range investigated the anisotropy constant decreases by about $33\,\mathrm{kJ/m^3}$. Simi-

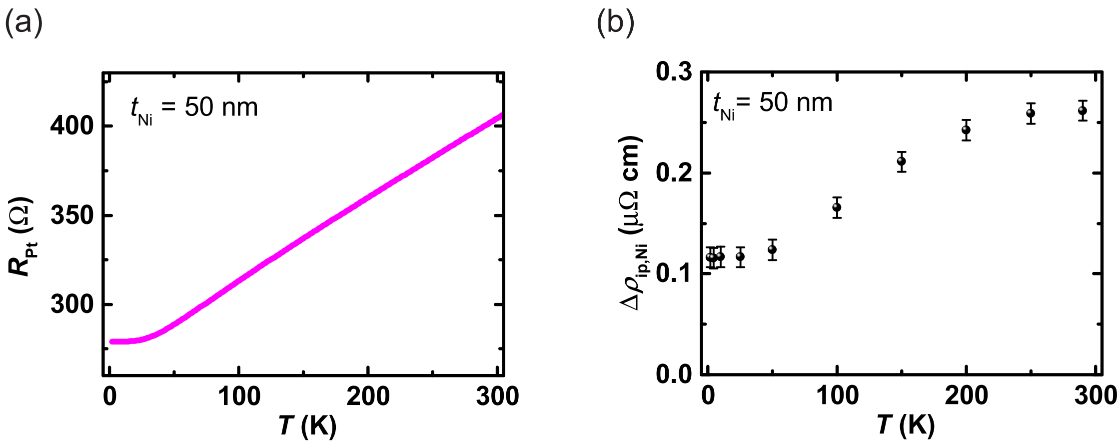

Figure 4.25: (a) Temperature dependence of Pt resistance according to Eq. 4.25 by using the parameters listed in Tab. 4.5 for 50 nm Ni thickness sample. (b) $\Delta\rho_{\mathrm{ip,Ni}}$ measured for the same sample as a function of temperature. The data is corrected for Pt shunt.

lar behavior was also observed by Co/Pt with 20 nm Co thickness with 80 kJ/m^3 decreasing with increasing the temperature from liquid He to room temperature [11].

The temperature dependence of AMR, op-AMR, and SMR effects are presented in the following.

4.8.3 Temperature dependence of AMR, op-AMR, and SMR effects

Before presenting the result of the temperature dependence of MR effects, I explain briefly the elimination of current shunt through Pt. Fig. 4.25(a) shows the resistance of Pt layer (8 nm in total) as a function of temperature according to Eq. 4.25. In this calculation I use the parameters from Tab. 4.5 for the sample with $t_{\mathrm{Ni}} = 50\,\mathrm{nm}$. With the calculated $R_{\mathrm{Pt}}(T)$ curve and substituting it in the Eq. 4.17, it is possible to correct all the measured data points for the Pt shunt.

Fig. 4.25(b) shows the shunt-corrected values of $\Delta\rho_{\mathrm{ip,Ni}}$ as a function of temperature for 50 nm Ni thickness sample. Qualitatively, $\Delta\rho_{\mathrm{ip,Ni}}$ shows no perceptible change under 50 K, while above this point it increases by a factor of ≈ 2.5 up to the room temperature. This means that the scattering of electrons by phonons and magnons leads to a significant contribution to the AMR in Ni/Pt sandwiches.
In contrast to the result of Ni/Pt structure, $\Delta\rho_{\mathrm{ip,Co}}$ in Co/Pt sandwiches shows only 10 - 15 % change in the temperature range of $4.2 < T < 300$ K considered for $t_{\mathrm{Co}} = 2$, 6, and 20 nm. This relatively small temperature dependence of the AMR has been attributed to the scattering at non-spherical defects, since this causes a lower scattering anisotropy compared to the scattering at spherical defects [11]. It

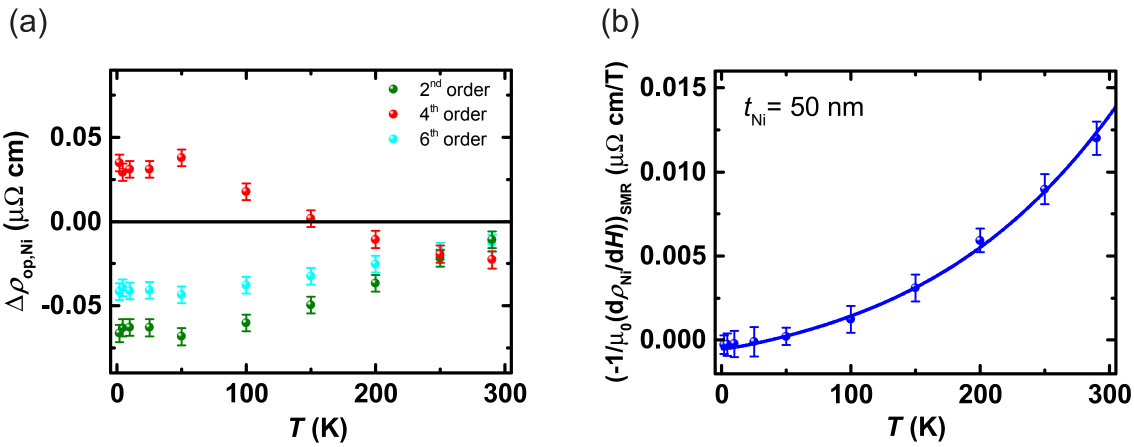

Figure 4.26: (a) $\Delta\rho_{\mathrm{op,Ni}}$ is plotted vs temperature for Pt(5 nm)/Ni(50 nm)/Pt(3 nm) sandwich, while the data is corrected for Pt shunt. Clearly, higher order contributions to the op-AMR exist in the whole range of temperature. (b) Temperature dependence of spin-disorder MR for the same sample. The solid line is the fit function according to Raquet model (Eq. 2.31) [76].

can be concluded here that the scattering at phonons and magnons in Ni/Pt has a dominant role than the scattering at the static defects.

Fig. 4.26(a) presents the difference resistivities $\Delta\rho_{\mathrm{op,Ni}}$ versus temperature for sample with 50 nm Ni thickness. Notably, all contributions exist in the whole range of temperature, while 2nd and 6th order contributions have negative values. For $T \leq 50\,\mathrm{K}$, I find $\left|\Delta\rho^{2\mathrm{n}}_{\mathrm{op,Ni}}\right|$ to be almost constant and above 50 K all prefactors decrease slightly up to the room temperature. Quantitatively, the 4th and 6th order contributions change by a factor of ≈ 2.5 in the whole range of temperature compared to the values at room temperature, while the second order changes by a factor of ≈ 5. It is worth to mention that the 6th order contribution plays a significant role in the temperature below RT.

Since the temperature dependence of higher order contributions to the op-AMR in Ni/Pt layered structure is not investigated so far, I cannot compare my results with other studies. I should also mention that the changes in $\Delta\rho_{\mathrm{op,CoPt}}$ (second order) are only in the range of 10 - 15 % revealing that they are basically governed by the scattering of the electrons at static defects, i.e., the Co/Pt interfaces [11].

In addition, the slope of high field MR measurements is studied for $2 < T < 300$ K. Fig. 4.26(b) shows the behavior of the slope of high field MR measurements as a function of temperature. It is assumed by Raquet et al. that in the case of ferromagnets, the temperature dependence of $-\frac{\mathrm{d}\rho_{\mathrm{mag}}}{\mathrm{d}H}$ follows the expression (see Sec. 2.2.6)

$$-\frac{\mathrm{d}\rho_{\mathrm{mag}}}{\mathrm{d}H} = AT(1+2d_1T^2)\ln\frac{T}{T_0} \tag{4.27}$$

where A is a constant depending on $s-d$ interaction, while $d_1 = D_1/D_0$ is determined by the ratio of the mass renormalization coefficient D_1 and the zero-temperature stiffness of the spin wave D_0 [76]. Qualitatively, the fit describes the data very well. In order to compare the result of the fit function to other works, I set T_0 to 1. The fit provides the coefficients $A = (3.7 \pm 0.4)\,\mathrm{p\Omega cm\ /KT}$ and $d_1 = (6.4 \pm 1.4) \times 10^{-6}\,\mathrm{K}^2$. The value of A was found by Raquet et al. in the range of 3 - 4 pΩcm /KT for thick Co films [76]. Moreover, the similar prefactor ($A = (3.1 \pm 0.4)\,\mathrm{p\Omega cm\ /KT}$) was obtained for Co/Pt sandwiches by A. Kobs [11]. On the other hand, the calculated parameter d_1 in the literature is in the range of 1 - 2 $\times 10^{-6}\,\mathrm{K}^2$ for Ni and $\mathrm{Ni}_{0.985}\mathrm{O}_{0.015}$, respectively, which is less than our result in this work [73, 76]. This difference may be a consequence of different range of temperature in the measurement (from 200 to 450 K).

Finally, it is worth mentioning that in order to have a complete overview to the temperature dependence of magnetoresistance effects in Ni/Pt films it is better to measure also a sample with intermediate thickness (e.g. $t_{\mathrm{Ni}} = 9\,\mathrm{nm}$) and compare the data. Here, because of time limitation only the temperature dependence of one sample were measured and discussed.

4.9 Conclusion

In this chapter the magnetoresistance of Pt/Ni/Pt layered structure fabricated by means of sputtering techniques was investigated in the temperature range of $4.2 \leq T \leq 295\,\mathrm{K}$. Previous studies on Pt/Co/Pt sandwiches showed that resistivity behaves as $\rho(\varphi, \theta) = \rho_\mathrm{t} + \Delta\rho_\mathrm{ip} \cos^2 \varphi \sin^2 \theta + \Delta\rho_\mathrm{op} \cos^2 \theta$ where φ/θ is the angle between magnetization and current direction/film normal. While $\Delta\rho_\mathrm{ip}$ is caused by the conventional AMR (bulk effect) a $\Delta\rho_\mathrm{op} \propto 1/t$ behavior was found for Co/Pt system revealing that $\Delta\rho_\mathrm{op}$ originates at the Co/Pt interfaces (anisotropic interface magnetoresistance (AIMR)). In contrast to Co/Pt, the MR measurements in Ni/Pt reveals that the resistivity is larger when the magnetization oriented perpendicular to the current in the film plane (ρ_t) than out of the film plane (ρ_p): $\Delta\rho_\mathrm{op} < 0$. Utilizing a constant magnetic field of 6 T, rotation of the magnetization in the plane perpendicular to the current direction for Ni/Pt presents a completely different behavior to the Co/Pt system. It was observed that $\rho(\theta)$ behavior can be described with considering higher orders in the expansion of the MR: $\rho(\theta) = \rho_\mathrm{t} + \sum_n \Delta\rho_{\mathrm{op},2n} \cos^{2n} \theta$ with $n \leqslant 3$. This was the key result of this chapter.

The thickness dependence of $R_{xx}(t_\mathrm{Ni})$ shows a $1/t_\mathrm{Ni}$ behavior that can be described with phenomenological Fuchs-Sondheimer model with the specularity parameter $p \approx 0$. This indicates that the interface scattering is completely diffusive. In addition to this result, with the fit parameter from the model it is possible to calculate the resistance of Pt layer (8 nm) $R_\mathrm{Pt} = (403 \pm 7)\,\Omega$ which enables us to eliminate current shunt through the Pt layer from the MR data. As a result, the pure thickness dependence of $\Delta\rho_\mathrm{ip,Ni}$ arising from the Ni layer increases with t_Ni for thicknesses below $t_\mathrm{Ni} \approx \lambda_\mathrm{bulk}$ revealing the presence of a finite size effect. $\lambda_\mathrm{bulk} = (4.23 \pm 0.20)\,\mathrm{nm}$ is the bulk mean free path of the electrons within the Ni layer. At higher thicknesses the AMR remains constant as we expected for a bulk effect.

Besides AMR effect, the thickness dependence of higher order contributions to the op-AMR for pure Ni layer of Ni/Pt sandwiches was investigated. As the sixth order contribution does not show a significant trend vs Ni thickness and it is negligibly small, we consider just second and forth orders. $\Delta\rho_\mathrm{op}^\mathrm{2nd}$ is a positive value for $t_\mathrm{Ni} < 30\,\mathrm{nm}$ while the fourth order is a dominant contribution and negative for all thicknesses. Utilizing a phenomenological model to fit both contributions we concluded from $1/t_\mathrm{Ni}$-behavior for $t_\mathrm{Ni} > 9\,\mathrm{nm}$ that both contributions originate from interfaces. However, the suppression of both effects at lower thicknesses is an indication of finite size effects. In addition, at large Ni thicknesses $\Delta\rho_\mathrm{op,2n}$ is overcompensated by the texture induced geometrical size effect (GSE).

The interpretation of the MR effects is based on a detailed investigation of the structural and magnetic properties of the samples. The crystal structure of the sample is polycrystalline with a (111) out-of-plane texture and a lateral grain size of $(14 \pm 2)\,\mathrm{nm}$ that was initiated during the growth of Pt seed layer. It was observed from XRR measurements that the interface roughness/interdiffusion zone is in the range of 2-3 MLs. The coherence length of $d_\mathrm{grain}^\mathrm{Ni} = (15.9 \pm 0.5)\,\mathrm{nm}$ (for $t_\mathrm{Ni} < 30\,\mathrm{nm}$)

and $d_{\mathrm{grain}}^{\mathrm{Pt}} = (4.8 \pm 0.1)\,\mathrm{nm}$ (for all samples) obtained from XRD suggest single crystalline phases along the stacking direction, while at large Ni layer thicknesses certain degree of structural disorder was observed. The orientation of (111) lattice planes of the crystallites is the pronounced texture of the film with the average tilting of $\approx (11 \pm 1)^\circ$ respect to the film normal also obtained from XRD. Concerning the magnetic anisotropy of the samples, a linear characteristic of the effective first order anisotropy constant $K_{1,\mathrm{eff}} \cdot t_{\mathrm{Ni}}(t_{\mathrm{Ni}})$ was found with $K_{1\mathrm{V,eff}} \approx (-133 \pm 3)\,\mathrm{kJ/m^3}$ and $K_{\mathrm{s}} \approx (0.015 \pm 0.030)\,\mathrm{mJ/m^2}$.

The temperature variation ($4.2 \leq T \leq 295\,\mathrm{K}$) also shows that the AMR and op-AMR change with temperature strongly. The higher order contributions to the op-AMR exist in the whole range of temperature. Moreover, it was found for Pt/Ni(50 nm)/Pt that the higher contributions are larger at low temperature than RT. It might be concluded that the scattering at the phonons and magnons governs the scattering at the static defects.

Chapter 5

Impact of aging process on the magnetotransport properties of Pd/Co/Pd layered structure

The stability of magnetic thin films is an important issue for their industrial application in data storage media. Since the late 80s Co/Pd systems with perpendicular magnetic anisotropy (PMA) are studied similar to Co/Pt stackings, making them promising candidates for perpendicular data storage media [149–151]. However, it took until 2010 that aging processes in Co/Pd were observed and reported. The first observation of aging in Co/Pd was made by Rosenblatt et al. [152]. They found that the resistivity of Co/Pd multilayer increases over a few months after preparation, which was attributed to oxidation or roughening of the surface. Moreover, another investigation on Pd/Co/Pd trilayer with perpendicular magnetic anisotropy studied by Li et al. showed a drastic time-dependent decrease of saturation magnetization and coersivity for $t_{\mathrm{Co}} < 1\,\mathrm{nm}$ [17]. It was suggested that the effect arises from the absorption of gaseous elements (for example, hydrogen). Other mechanisms were put forward to explain the aging process in Co/Pd like gradual intermixing and formation of interfacial CoPd alloys [153, 154], while sophisticated studies about structural changes over time are missing so far.

The thickness dependence of the MR effects (AMR, AIMR, and SMR) of Pd/Co/Pd thin films were studied at room temperature by G. Winkler in our group [77]. In contrast to Ni/Pt, the finding results in Co/Pd were similar (qualitatively) to Co/Pt thin film studied by A. Kobs [10, 11]. Furthermore, it was found that the strength of the MR effects show significant changes over time. Fig. 5.1 presents as an example for the temporal resistivity change $\Delta\rho_{\mathrm{xx}}$ of Pd(5 nm)/t_{Co}/Pd(3 nm) for two time intervals from Ref. [77]. Clearly, the resistivity shows a drastic change for all thicknesses especially in the first 6 months. In order to systematically study the aging phenomenon the magnetotransport is repeatedly measured for Co/Pd within 600 days. The tranport investigations were accompanied by X-ray reflectivity measurements in order to trace back the underlying structural changes.

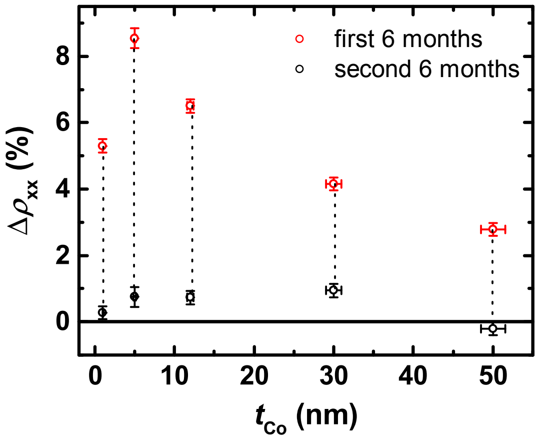

Figure 5.1: Changes in resistivity $\Delta\rho_{\mathrm{xx}}$ of Pd(5 nm)/t_{Co}/Pd(3 nm) for two time intervals of 6 months. Red symbols present $\Delta\rho_{\mathrm{xx}}$ for the fist 6 months and the black symbols for the second 6 months after preparation. The plot is from Ref. [77].

In the first part of this chapter (Sec. 5.1) the magnetoresistance measurements are briefly explained and for comparison the MR curves are shown for different dates after preparation. The XRR measurements and their changes over 600 days are presented in Sec. 5.2. Finally, the influence of aging on magnetoresistance effects are investigated and discussed.

5.1 Sample preparation and magnetoresistance measurements

In order to follow the aging process of Co/Pd system, we prepared two samples with Co thicknesses of 2 and 7 nm via sputtering techniques on Si_3N_4 as a substrate. As seed and cap layer, 5 and 3 nm Pd are used respectively. More details about sample preparation and sputtering techniques can be found in Sec. 3.1.

At certain dates after preparation the magnetoresistance measurements in current inplane (CIP) geometry were repeatedly performed. The first measurement was done 6 hours after preparation while the last one was 600 days after that. In addition, the structural properties (XRR measurements) were investigated at the same time at Helmholtz-Zentrum Geesthacht (HZG). Details about the geometry of MR measurements (sweep and rotations) can be found in Sec. 4.2.

Fig. 5.2 presents as an example the MR measurements of the prepared Co/Pd samples at different times after preparation. The trace of aging can be seen clearly on both samples over time. As expected, the in-plane and out-of-plane rotations of magnetization with respect to the current direction follow $\cos^2$ behavior, which are typical for AMR and AIMR effects in Co/Pd layered structure.

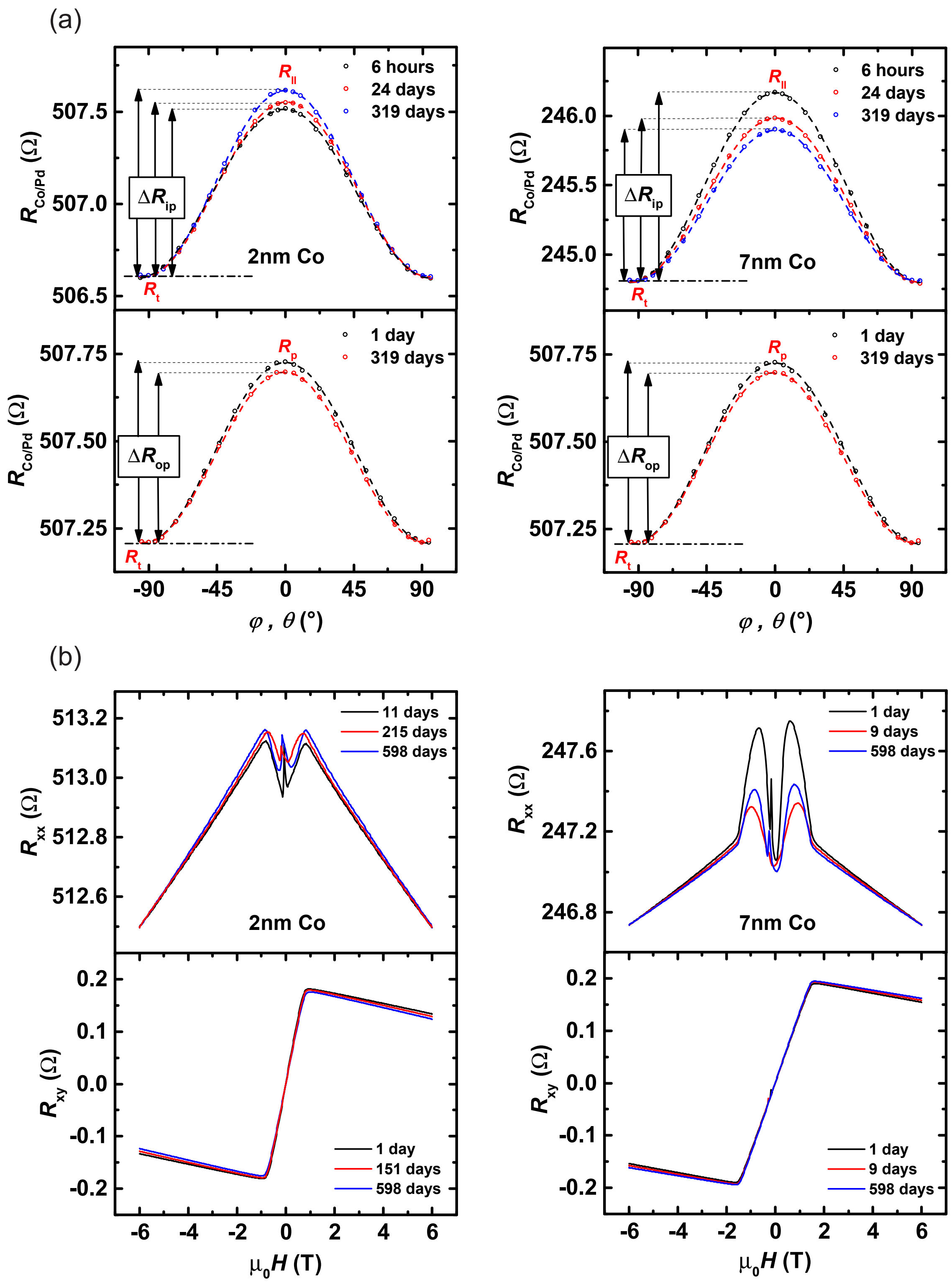

Figure 5.2: Magnetoresistance curves for Pd(5 nm)/Co(2 nm)/Pd(3 nm) and Pd(5 nm)/Co(7 nm)/Pd(3 nm). (a) Resistance as a function of the in-plane and out-of-plane angle (φ, θ) measured in a saturation field of 6 T. The dashed lines are $\cos^2$ fits. (b) Typical field dependence of resistance measured in polar geometry for both samples at certain dates after preparation. The changes in spin-disorder MR are obtained from the longitudinal measurements $R_{xx}(H_\mathrm{p})$, while the aging in magnetic anisotropy and Hall constants are determined via the transverse measurements $R_{xy}(H_\mathrm{p})$.

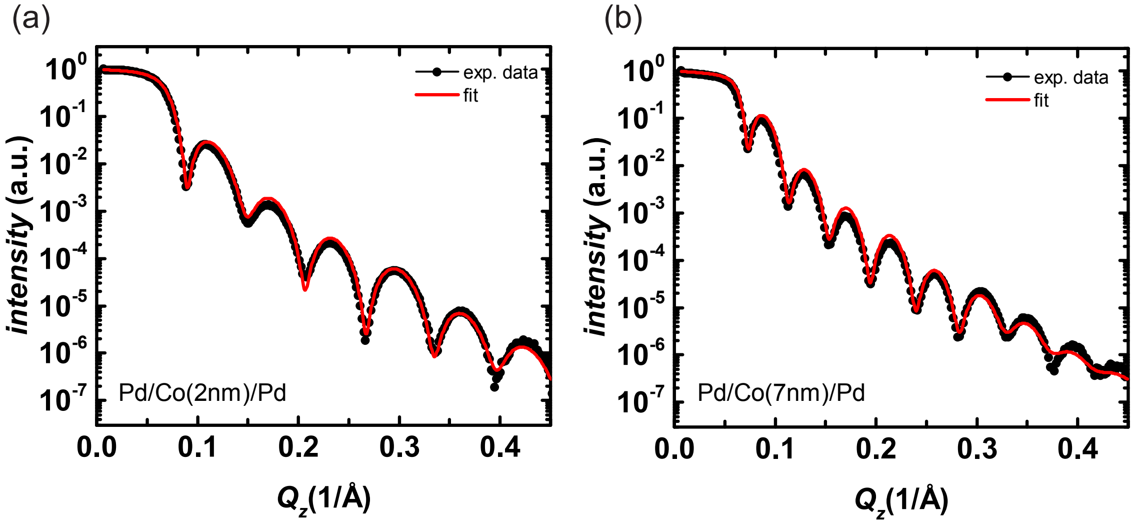

Figure 5.3: X-ray reflectrometry of Pd(5 nm)/Co(2 nm)/Pd(3 nm) and Pd(5 nm)/Co(7 nm)/Pd(3 nm) on Si_3N_4 substrate (black symbols) measured 1 day after preparation. The red solid lines are fits to the curves utilizing Paratt's recursive formalism.

It is possible to investigate the resistivity $\rho_{\mathrm{Co/Pd}}$, $\Delta\rho_{\mathrm{AMR}}$, and $\Delta\rho_{\mathrm{AIMR}}$ as a function of time from rotational measurement (Fig. 5.2(a)).
Additionally, the longitudinal and transverse field sweep measurements for both Co thicknesses are shown in Fig. 5.2(b). In order to study the time-dependence of magnetic anisotropy $K_{1,\mathrm{eff}}$, OHE, and AHE effects the sweep measurements in polar geometry were preformed.
The following section deals with introducing the XRR measurements done for the samples.

5.2 Structural properties of Pd/Co/Pd sandwich

Fig. 5.3 shows an exemplary result of XRR data for Co/Pd samples with $t_{\mathrm{Co}} = 2$ and 7 nm, measured one day after preparation. The red solid lines are the fits based on Paratt's recursive formalism. The IGOR Pro[1] software with Motofit package was used to apply the fit. More details about the fit function were explained in Sec. 4.1.2.

Here, the fit parameters were thickness and roughness of the layers, while the scattering length density (SLD) of each layer was fixed. The real and imaginary parts of scattering length density (dispersion and absorption) for Co and Pd are obtained from Center of X-ray Optics database (CXRO)[2]. These parameters are given in table 5.1.

---

[1] https://www.wavemetrics.com

[2] http://henke.lbl.gov/optical_constants/pert_form.html

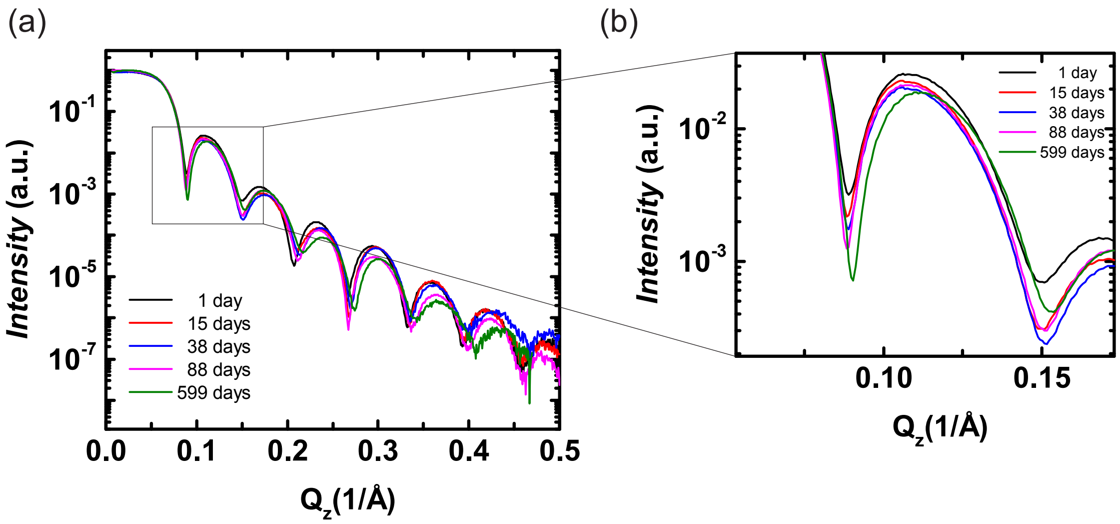

Figure 5.4: (a) XRR measurements of Pd(5 nm)/Co(2 nm)/Pd(3 nm) thin film measured for 5 different times after preparation. (b) A zoom-in to the first oscillation shown in (a).

	SLD(δ) (Å^{-2})	iSLD(β) (Å^{-2})
Co	6.3×10^{-5}	9.2×10^{-6}
Pd	8.9×10^{-5}	7.7×10^{-6}
Si_3N_4	2.9×10^{-5}	4.4×10^{-7}

Table 5.1: Scattering length density of Co, Pd, and Si_3N_4.

As we see, the data can be described very well with a three-layer model. According to Eq. 4.3 the total thickness of each stack can be calculated from ΔQ_z between the maxima of a period. Here the total thickness of 100.9 Å and 149.6 Å are obtained for Fig. 5.3(a) and (b) respectively, revealing 0.9 % and 0.4 % difference from the nominal thickness, which is within the resolution of the experiment. These values verify the deposition rates for the sample preparation.

Within the time span of 600 days, the XRR measurements on Co/Pd samples with $t_{\mathrm{Co}} = 2$ and 7 nm show visible changes. This is shown as an example for 2 nm Co thickness in Fig. 5.4(a), while Fig. 5.4(b) displays an enlarged representation of one oscillation of (a). Clearly the amplitude of this oscillation changes with time. Moreover, a weak difference in damping of the curve is detectable for the oscillations, which reflects changes of the roughness and interdiffusion region at the interfaces. In order to have a quantitative description of these changes over a time span of 600 days, the result of the fit parameters have to be plotted and discussed. This is done in the following section after presenting the results for the MR effects.

5.3 Influence of aging on resistivity, AMR, and AIMR effects in Co/Pd layered structure

In this section, I present the aging process of the magnetoresistance effects of two Co/Pd samples in a time span of 600 days. Fig. 5.5 displays the time-dependence of resistance, magnetic anisotropy, AMR, and AIMR effects for 2 nm (black symbols) and 7 nm (red symbols) Co thickness samples.

First of all the result of R_{xx} (ρ_{xx}) is discussed[3]. It is seen that both samples behave differently. The resistance increases sharply in the first 60-90 days and from this point R_{xx} of the sample with 2 nm Co decreases slightly while the resistance of the thicker sample levels out to a constant value. I have to mention that the thinner sample is more sensitive to the amount of Pd (80% of the film) comparing to the thicker sample with $\approx 50\%$ Pd. Hence, the aging process in these two Co/Pd samples arises not only from the interfaces but also from the bulk.

Qualitatively, at least two mechanisms can be suggested for the changes in resistance. Intermixing and formation of interfacial CoPd alloys results in increasing R_{xx} in the first phase (60-90 days), while decreasing the resistance in thinner sample can be attributed to the absorption of gaseous elements (hydrogen) during exposure to the air. The latter is reported frequently for Co/Pd system in literature [17, 18, 155].

The main composition of the air are N_2 and O_2. Li et al. showed that N_2 can not change the magnetic properties of Co/Pd multilayers [17]. Moreover, Pd is commonly used as a material for prevention of oxidation [156–158]. Therefore, O_2 can be ruled out as well. Although it is reported that CO and NO have influences on magnetic anisotropy of the Co thin films [159], it is hardly possible to argue that they might be able to penetrate into Co layer through the Pd capping layer due to their very large atomic radius for penetration through Pd [17].

Furthermore, it is well known that Pd can absorb a large amount of H [18] and this is used in the industry to purify H [160, 161]. It is observed that the susceptibility χ of Pd decreases with increasing H concentration. This is due to the gradual filling of $4d$ band holes by electrons coming from H [162, 163]. Wen et al. reported that due to the absorption of H in Co/Pd multilayers, the saturation magnetization and the coercivity demonstrate a drastic decrease [17, 155].

The results for the aging of AMR and AIMR are shown in Fig. 5.5. The ΔR_{AMR} ($\Delta\rho_{\mathrm{AMR}}$) of both samples follow a completely opposite behavior while the ΔR_{AIMR} ($\Delta\rho_{\mathrm{AIMR}}$) behavior is much more complicated. It is found that the most changes occur already in the first ≈ 100 days in both effects.

Additionally, the magnetic anisotropy $K_{1,\mathrm{eff}}$ of the samples is determined from transverse sweep measurement R_{xy} according to Sec. 4.3. Fig. 5.5(c) demonstrates that the magnetic anisotropy in both samples do not change significantly over time.

---

[3] For the sake of completeness it is mentioned that the resistivity of Co/Pd samples are calculated according to Eq. 4.4 with the total thickness of the film.

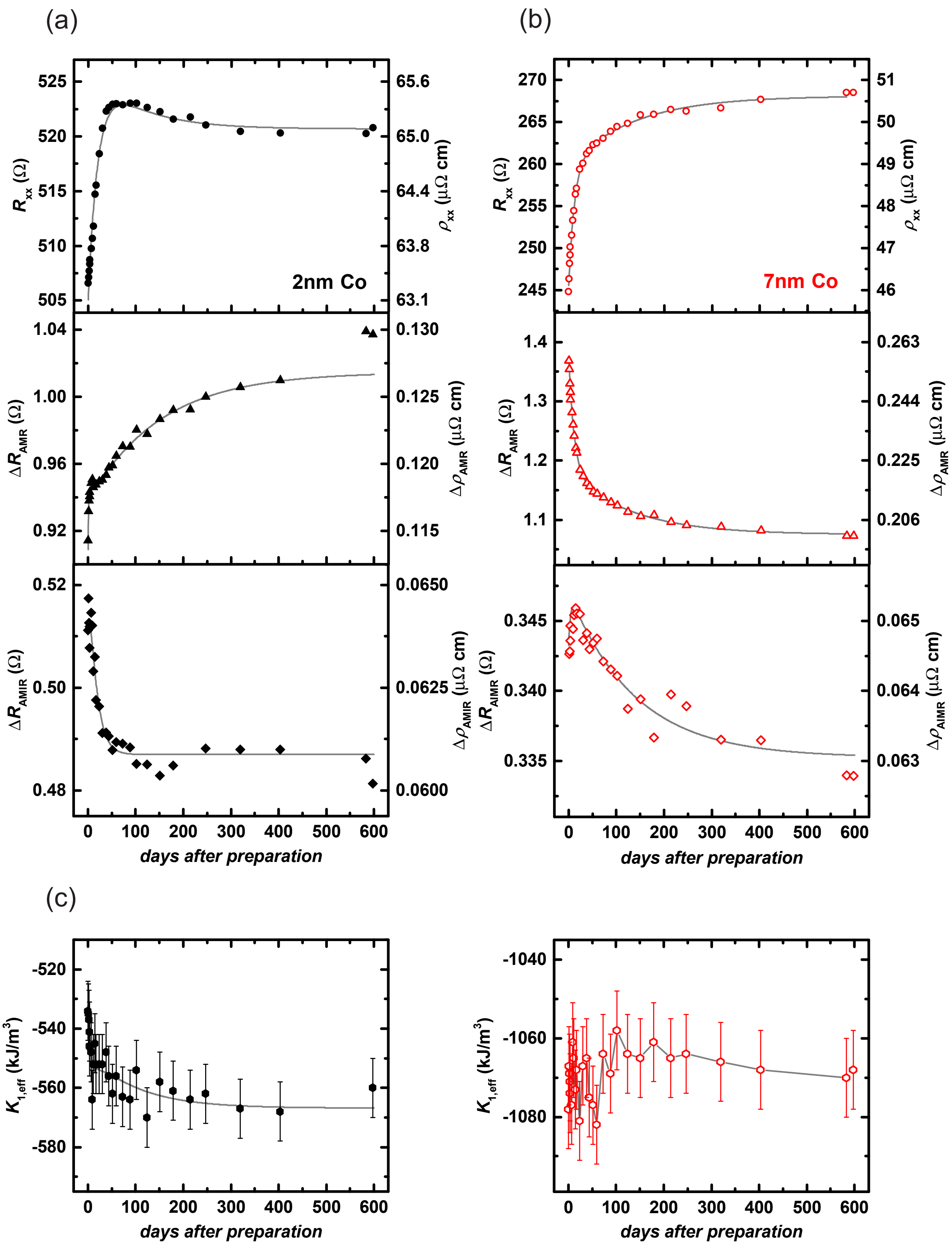

Figure 5.5: (a) and (b) Changes of resistance/resistivity, ΔR_{AMR}, and ΔR_{AIMR} of Co/Pd with 2 and 7 nm Co thickness as a function of time. (c) Changes of the magnetic anisotropy $K_{1,\mathrm{eff}}$ of the same samples as a function of time. The solid lines are guides to the eyes.

In the case of the thinner sample, $K_{1,\mathrm{eff}}$ changes are about 6%, while for the thicker sample it is only 2%. As I stated at the beginning of this chapter, the aging process of magnetic properties of Co/Pd thin films were not found or studied in details before 2010. This might be due to the small changes of magnetic anisotropy in Co/Pd, where the aging process sets in. In contrast to our findings (no change in M_S and almost constant $K_{1,\mathrm{eff}}$), however, it is reported recently that aging also influences the magnetization saturation and magnetic anisotropy of Co/Pd system [17, 164]. Mentioned before, Li et al. observed a decrease in the saturation magnetization of Co/Pd system, which was strongly related to the Co layer thickness. During exposure of the samples to the air, M_S drops 10%, 50%, and 90% for t_Co = 6, 5, and 3 Å, respectively, over time span of 13 days [17]. Therefore, in the case of t_Co = 2 nm (my thinner sample) it was not expected to observe a drastic change in saturation magnetization and magnetic anisotropy over time. In another investigation of changes in magnetic properties of Co/Pd multilayers by Munbodh et al., it was reported that M_S and K_eff decrease upon exposing the samples to 1 atm of H_2 at room temperature [164]. In this case, clearly, a drastic changes in magnetic properties is more probable comparing to exposure of the samples to the air.

5.4 Influence of aging on Hall constants in Co/Pd layered structure

This section deals with the other MR effects obtained from sweep measurements in Pd/Co/Pd samples over time. Fig. 5.6 shows the result of aging for Hall constants and for both samples separately. It is worth mentioning that the Hall constants are calculated according to Eq. 4.22 with the total thickness of the film.

Obviously, there is a significant difference between the results for the two samples. The changes in the thicker sample show a sharp increase or decrease in Hall constants during the first 60 days since preparation and then follow a relatively stable behavior, while the thinner sample experiences a complicated behavior.

Although both samples demonstrate different behavior, the ordinary Hall constant changes about 10% for both samples while the values for anomalous Hall constants change only 2.5% over 600 days. It is reported that the polarity of AHE in Co/Pd system changes over time [152, 153]. As an example, Winer et al. demonstrated recently that the reversal of AHE polarity is due to intermixing and formation of CoPd alloys at the interfaces of Co/Pd multilayers [153]. Notably, in the case of our samples the reversal of AHE polarity was not observed.

For the sake of completeness the aging process in SMR effect for both samples is shown in appendix.

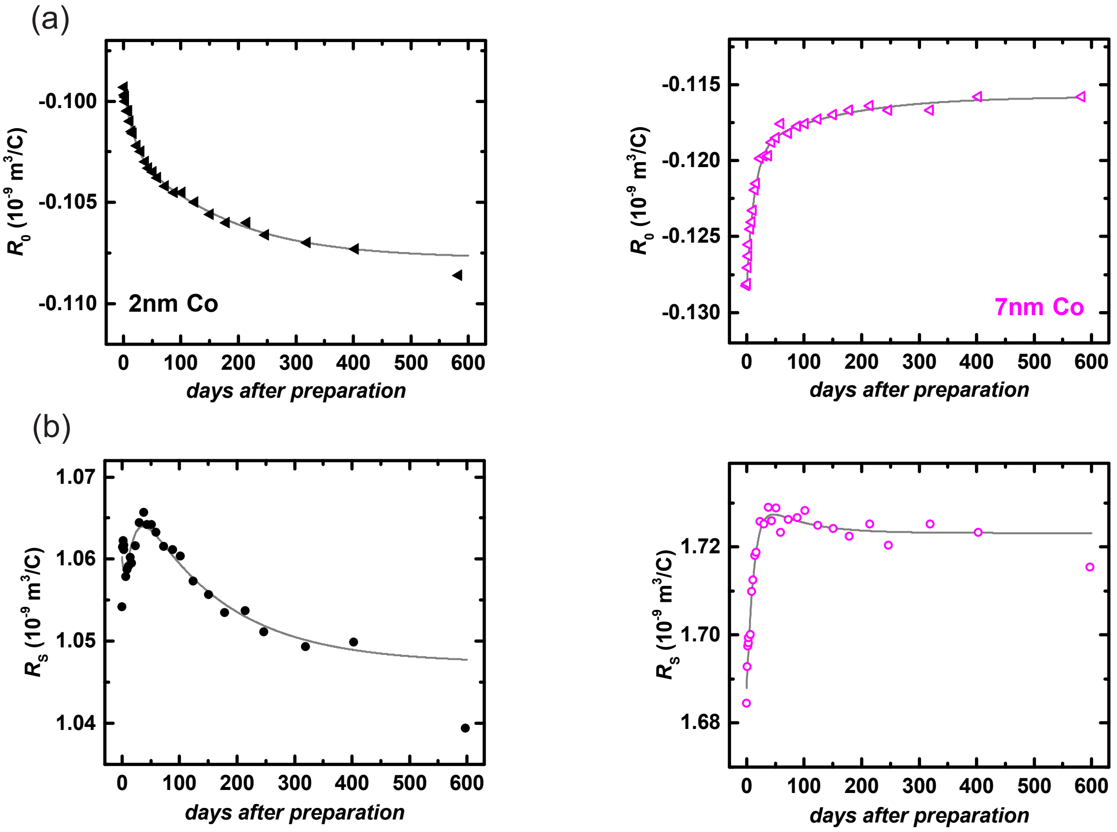

Figure 5.6: (a) Ordinary Hall constant (OHE) and (b) anomalous Hall constant (AHE) are shown for Pd/Co/Pd sandwiches with $t_{\mathrm{Co}} = 2$ and 7 nm as a function of time elapsed after preparation. The solid lines are guides to the eyes.

5.5 Time-dependence of XRR fit parameters for Co/Pd structure

As stated in Sec. 5.2, in order to evaluate the XRR measurements roughness/interdiffusion region of each interface and the thickness of the layers were set as fit parameters.

Fig. 5.7 presents as an example the changes of roughness/interdiffusion region for Pd/Co(7 nm)/Pd as a function of time since preparation. It has to be mentioned that the result for $t_{\mathrm{Co}} = 2$ nm is similar to the thicker sample. In the case of our trilayer Co/Pd sandwiches there are four interfaces/surfaces. It is seen that the maximum values are obtained for Co-Pd interface which is less than 1 nm. In the first month, a fluctuating behavior can be observed for the extension of the roughness/interdiffusion region of all interfaces which is less than 1 Å. Afterwards, all the trends follow almost constant values and do not show any aging. The average values of 9 Å, 7 Å, 7 Å, and 5 Å are calculated from the fit parameters for Co-Pd, Pd-air, Pd-Co, and substrate-Pd interfaces respectively.

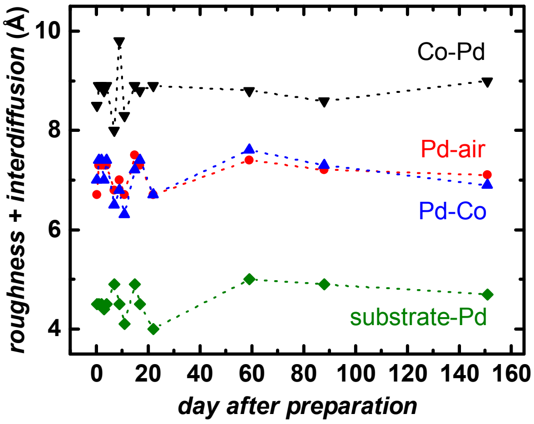

Figure 5.7: Changes of roughness/interdiffusion region for Pd/Co(7 nm)/Pd layered structure as a function of time elapsed after preparation.

Moreover, the changes in the thickness of each layer from the utilized model as a function of time do not show any special trend. Similar to the result of roughness/interdiffusion region, the thickness shows fluctuations over the first month and then the thickness graph (which is not presented here) of each layer remains fairly static.

Although the changes in the structural measurement illustrated in Fig. 5.4 occur undoubtedly over a time span of 600 days, it is hardly possible to describe quantitatively the structure of Co/Pd system by using the applied model. It seems that an alternative model to describe the structural changes of Co/Pd system is needed.

5.6 Conclusion and outlook

In this chapter the aging process on magnetoresistance effects of Pd/Co/Pd layered structure was investigated. For this purpose, two Pd(5 nm)/Co/Pd(3 nm) samples with 2 and 7 nm Co thicknesses were fabricated by means of sputtering techniques. The MR effects and structural properties (X-ray reflectometry) were measured simultaneously at room temperature over 600 days.

The changes in resistivity, AMR, and AIMR effects were obtained as a function of time from in-plane and out-of-plane rotation of magnetization with respect to the current direction. Different behavior of both samples might be influenced by the relative amount of Co to Pd in these samples (80% Pd in thinner sample vs 53% in thicker one). Additionally, the changes in the resistivity indicated that at least two mechanisms are responsible for the aging procedure in Co/Pd. The enhancement of resistivity in the first 90 days is attributed to intermixing and formation of CoPd alloys at the interfaces while slight decrease of resistivity after 90 days is due to the absorption of H.
Besides, the magnetic anisotropy of the samples did not show significant variation over time (2-6%). This may be the reason of lack of aging study in Co/Pd system from 1990 till 2010. The time-dependence of Hall constants of Co/Pd were also determined from field sweep measurements. Again different behavior of both samples were observed, which make them more complicated to explain the mechanisms behind.

In order to understand and clarify the origin of aging effect in Co/Pd layered structure, XRR measurements were performed. The goal was to find a correlation between the evolution of magnetoresistance effects and structural properties over a period of several months.
It was observed qualitatively that the structural measurements show aging over time. In order to describe the aging process quantitatively a fit model based on Paratt's recursive formalism was applied with roughness and thickness as fit parameters. Unfortunately the outcome of the fitting does not show any significant variation of the fit parameters over time that can explain the evolution occurring in MR properties.
The next step might be focusing on the scattering length densities, in a way that the thickness and roughness of each layer are set as fixed values while the SLD of Pd layer is assumed as fit parameters. Using this procedure it might be possible to detect H in Pd layer or to visualize at least the time-dependence of H penetration. For further studies, it is also interesting to fabricate a similar Co/Pd sample and trace the magnetic properties before and after putting the sample in hydrogen atmosphere in order to hydrogenate the sample. Then might be possible to distinguish between the H absorption and the intermixing mechanism.

Appendix

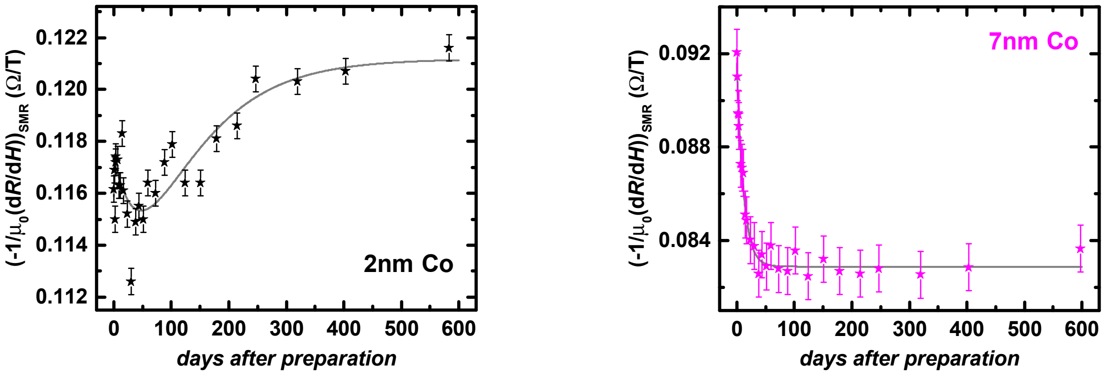

Figure 1: Changes in spin-disorder magnetoresistance (SMR) for both Pd/Co/Pd samples as a function of time elapsed after preparation.

The strength of spin-disorder MR was determined from the slope of high field R_{xx} (see Fig. 5.2). The figure above shows the result of changes of SMR for 2 and 7 nm Co thicknesses samples over time. Again both samples follow different behavior. Here, the changes in SMR effect for thicker sample is about 10% vs 6% for the thinner one. In order to explain the influence of aging on SMR effect in Co/Pd system one has to understand completely the mechanisms related to the changes in resistance and other MR effects.

Bibliography

[1] J. Stöhr and H. Siegmann, *Magnetism: From Fundamentals to Nanoscale Dynamics*, Springer Series in Solid State Sciences, (Springer, 2006).

[2] J. D. Livingston, *Driving force: The natural magic of magnets*, (Harvard University Press, 1996).

[3] J. Lenz and S. Edelstein, "Magnetic sensors and their applications", *IEEE Sensors journal* **6**, 631 (2006).

[4] J. E. Lenz, "A review of magnetic sensors", *Proceedings of the IEEE* **78**, 973 (1990).

[5] P. Ripka, "Security applications of magnetic sensors", *Journal of Physics: Conference Series* **450**, 012001 (2013).

[6] M. Usher, *Sensors and transducers*, (MacMillan Press Ltd., London, England, 1985).

[7] N. A. Spaldin, *Magnetic materials: Fundamentals and Applications*, (Cambridge University Press, 2010).

[8] P. Ripka, "Sensors based on bulk soft magnetic materials: Advances and challenges", *Journal of Magnetism and Magnetic Materials* **320**, 2466 (2008).

[9] T. McGuire and R. Potter, "Anisotropic magnetoresistance in ferromagnetic 3d alloys", *IEEE Transactions on Magnnetics* **11**, 1018 (1975).

[10] A. Kobs, S. Hesse, W. Kreuzpaintner, G. Winkler, D. Lott, P. Weinberger, A. Schreyer, and H. P. Oepen, "Anisotropic interface magnetoresistance in Pt/Co/Pt sandwiches", *Physical Review Letters* **106** (2011).

[11] A. Kobs, *Magnetogalvanic effects in ferromagnets of reduced dimensions*, Ph.D. thesis, Hamburg University (2013).

[12] X. Xiao, J. X. Li, Z. Ding, and Y. Z. Wu, "Four-fold symmetric anisotropic magnetoresistance of single-crystalline Ni(001) film", *Journal of Applied Physics* **118**, 203905 (2015).

[13] P. Sparks, N. Stern, D. Snowden, B. Kappus, J. Checkelsky, S. Harberger, A. Fusello, and J. Eckert, “Stripe domains and magnetoresistance in thermally deposited nickel films”, *Journal of Magnetism and Magnetic Materials* **272**, E1339 (2004).

[14] S. D. Choi, H. W. Joo, S. S. Lee, D. G. Hwang, J. H. Choi, K. A. Lee, S. Kim, and S. Bae, “Partial magnetization reversal in a perpendicular exchange-biased [Pd/Co]/FeMn film through laser annealing”, *Journal of Applied Physics* **101**, 09E519 (2007).

[15] S. Mohanan and U. Herr, “Optimization of magnetic properties of Co/ Pd multilayers by applying a large persistent biaxial stress”, *Journal of Applied Physics* **102**, 093903 (2007).

[16] S. Choi, S. Kim, H. Joo, K. Lee, S. Lee, and D. Hwang, “Effect of remanent magnetization on exchange biasing in [Pd/Co]× 5/FeMn films”, *Journal of Magnetism and Magnetic Materials* **310**, 2304 (2007).

[17] L. Li, F. Wen, F. Zhang, Y. Lü, Y. Lu, Z. Liu, B. Xu, D. Yu, J. He, and Y. Tian, “Drastic time-dependent decrease in the saturation magnetization observed in Pd/Co/Pd trilayers with perpendicular anisotropy”, *Journal of Applied Physics* **107**, 123912 (2010).

[18] S. Okamoto, O. Kitakami, and Y. Shimada, “Enhancement of magnetic anisotropy of hydrogenated Pd/Co/Pd trilayers”, *Journal of magnetism and magnetic materials* **239**, 313 (2002).

[19] C. Wang, F. Wen, F. Zhang, Y. Lü, J. Xiang, W. Lü, and C. Hao, “Aging dependent anomalous Hall effect in Pd(50 Å)/Co(5 Å)/Pd(54 Å)/Co(5 Å)/Pd(50 Å) multilayer with perpendicular anisotropy”, *Thin Solid Films* **545**, 485 (2013).

[20] R. O’Handley, *Modern Magnetic Materials: Principles and Applications*, (Wiley, 1999).

[21] S. Chikazumi and C. D. Graham, *Physics of Ferromagnetism - International Series of Monographs on Physics 94*, (Oxford University Press, 1997).

[22] A. Aharoni, *Introduction to the Theory of Ferromagnetism - International Series of Monographs on Physics 109*, (Oxford University Press, 1996).

[23] R. M. Bozorth, *Ferromagnetism*, (Wiley VCH, 1993).

[24] J. Coey, *Magnetism and Magnetic Materials*, (Cambridge University Press, 2010).

[25] M. Getzlaff, *Fundamentals of Magnetism*, (Springer Berlin Heidelberg, 2007).

[26] J. Hofmann, A. Paskin, K. Tauer, and R. Weiss, “Analysis of ferromagnetic and antiferro-magnetic second-order transitions”, *Journal of Physics and Chemistry of Solids* **1**, 45 (1956).

[27] S. Blundell, *Magnetism in Condensed Matter - Oxford Master Series in Condensed Matter Physics*, (Oxford University Press, 2001).

[28] H. Ibach and H. Lüth, *Solid State Physics: An Introduction to Principles of Material Science*, (Springer Verlag, 2009).

[29] L. Néel, “Anisotropie magnétique superficielle et surstructures d’orientation”, *Journal de Physique et le Radium* **15**, 225 (1954).

[30] U. Gradmann and J. Müller, “Flat ferromagnetic, epitaxial 48Ni/52Fe(111) films of few atomic layers”, *Physica Status Solidi B* **27**, 313 (1968).

[31] U. Gradmann, R. Bergholz, E. Bergter, U. Gradmann, R. Bergholz, and E. Bergter, “Magnetic surface anisotropies of clean Ni”, *IEEE Transactions on Magnetics* **20**, 1840 (1984).

[32] U. Gradmann, “Magnetic surface anisotropies”, *Journal of Magnetism and Magnetic Materials* **54**, 733 (1986).

[33] F. den Broeder, W. Hoving, and P. Bloemen, “Magnetic anisotropy of multilayers”, *Journal of Magnetism and Magnetic Materials* **93**, 562 (1991).

[34] K. Chafai, H. Salhi, H. Lassri, Z. Yamkane, M. Lassri, M. Abid, E. Hlil, and R. Krishnan, “Magnetic studies in evaporated Ni/Pd multilayers”, *Journal of Magnetism and Magnetic Materials* **323**, 596 (2011).

[35] J.-R. Jeong and S.-C. Shin, “Room-temperature perpendicular magnetic anisotropy in Ni/Pd (111) multilayers”, *Applied Physics Letters* **75**, 3174 (1999).

[36] M. T. Johnson, P. J. H. Bloemen, F. J. A. den Broeder, and J. J. de Vries, “Magnetic anisotropy in metallic multilayers”, *Reports on Progress in Physics* **59**, 1409 (1996).

[37] T. Kingetsu, “Molecular-beam-epitaxial growth and magnetic properties of (111)Pt/Co/Ag, Pt/Co, and Ag/Co/Pt superlattices”, *Journal of Applied Physics* **76**, 4267 (1994).

[38] J. Osborn, “Demagnetizing factors of the general ellipsoid”, *Physical review* **67**, 351 (1945).

[39] D.-X. Chen, J. A. Brug, and R. B. Goldfarb, “Demagnetizing factors for cylinders”, *IEEE Transactions on Magnetics* **27**, 3601 (1991).

[40] P. Drude, “On the electron theory of metals”, *Annals of Physics* **1**, 566 (1900).

[41] J. M. Ziman, *Electrons and phonons: the theory of transport phenomena in solids*, (Oxford university press, 1960).

[42] J. S. Dugdale, *The electrical properties of metals and alloys - The structures and properties of solids 5*, (Edward Arnold Publishers, 1977).

[43] A. Bid, A. Bora, and A. K. Raychaudhuri, “Temperature dependence of the resistance of metallic nanowires of diameter $\geqslant$ 15 nm: Applicability of Bloch-Grüneisen theorem”, *Physical Review B* **74** (2006).

[44] D. Feng and G. Jin, *Introduction to condensed matter physics 1*, (World Scientific, 2005).

[45] B. Coles, “Spin-disorder effects in the electrical resistivities of metals and alloys”, *Advances in Physics* **7**, 40 (1958).

[46] N. Mott, “Electrons in transition metals”, *Advances in Physics* **13**, 325 (1964).

[47] U. Mizutani, *Introduction to the Electron Theory of Metals*, (Cambridge University Press, 2001).

[48] W. Thomson, “On the electro-dynamic qualities of metals: Effects of magnetization on the electric conductivity of nickel and of iron”, *Proceedings of the Royal Society of London* **8**, 546 (1856).

[49] J. W. F. Dorleijn and A. R. Miedema, “The Magnetic Resistance Anisotropy in Nickel and Iron Based Alloys”, *AIP Conference Proceedings* **34**, 50 (1976).

[50] I. Campbell and A. Fert, “Transport properties of ferromagnets”, *Ferromagnetic materials* **3**, 747 (1982).

[51] P. Rossiter, *The Electrical Resistivity of Metals and Alloys*, Cambridge Solid State Science Series, (Cambridge University Press, 1991).

[52] E. Englert, “Ferromagnetismus und elektrische Eigenschaften VI. Mitteilung: Longitudinale und transversale ferromagnetische Widerstandsänderung”, *Annalen der Physik* **406**, 589 (1932).

[53] J. Smit, “Magnetoresistance of ferromagnetic metals and alloys at low temperatures”, *Physica* **17**, 612 (1951).

[54] U. Hartmann, *Magnetic Multilayers and Giant Magnetoresistance 37*, (Springer Series in Surface Science, 2000).

[55] W. Gil, D. Görlitz, M. Horisberger, and J. Kötzler, "Magnetoresistance anisotropy of polycrystalline cobalt films: Geometrical-size and domain effects", *Physical Review B* **72**, 134401 (2005).

[56] T. T. Chen and V. A. Marsocci, "Transverse magnetoresistivity anisotropy measurements and the geometrical size effect in nickel thin films", *Journal of Applied Physics* **43**, 1554 (1972).

[57] T. G. S. M. Rijks, S. K. J. Lenczowski, R. Coehoorn, and W. J. M. de Jonge, "In-plane and out-of-plane anisotropic magnetoresistance in $Ni_{80}Fe_{20}$ thin films", *Physical Review B* **56**, 362 (1997).

[58] R. Potter, "Magnetoresistance anisotropy in ferromagnetic NiCu alloys", *Physical review B* **10**, 4626 (1974).

[59] A. Kobs, S. Hesse, H. Oepen, and P. Weinberger, "Anisotropic interface magnetoresistances in Pt(111)/Co_n /Pt(111)", *Philosophical Magazine* **92**, 2835 (2012).

[60] Y. M. Lu, J. W. Cai, S. Y. Huang, D. Qu, B. F. Miao, and C. L. Chien, "Hybrid magnetoresistance in the proximity of a ferromagnet", *Physical Review B* **87** (2013).

[61] J.-C. Lee, C.-H. Hsieh, C.-C. Chang, L.-W. Huang, L.-K. Lin, and S.-F. Lee, "Comparison of anistropic interface magnetoresistance in Co/Pt and Co/Pd multilayers", *Journal of Applied Physics* **113**, 17C714 (2013).

[62] E. H. Hall, "On a new action of the magnet on electric currents", *American Journal of Mathematics* **2**, 287 (1879).

[63] E. M. Pugh, "Band model for hall effect, magnetization, and resistivity of magnetic metals", *Physical Review* **97**, 647 (1955).

[64] J. M. Lavine, "Extraordinary Hall-effect measurements on Ni, some Ni alloys, and ferrites", *Physical Review* **123**, 1273 (1961).

[65] S. Foner and E. M. Pugh, "Hall effects of the cobalt nickel alloys and of Armco iron", *Physical Review* **91**, 20 (1953).

[66] S. D. Roy and A. Subrahmanyam, "Hall Effect, Magnetic Resistivity, and Magnetic Susceptibility of Nickel and Nickel-Copper Alloys", *Physical Review* **177**, 1133 (1969).

[67] C. M. Hurd, *The Hall Effect in Metals and Alloys - The International Cryogenics Monograph Series*, (Plenum Press, 1972).

[68] J.-P. Jan, "Galvamomagnetic and thermomagnetic effects in metals", *Solid State Physics* **5**, 1 (1957).

[69] O. A. Panchenko, P. P. Lutsishin, and Y. G. Ptushinskiǐ, "Galvanomagnetic effects in thin films of some transition metals", *Soviet Physics JETP* **29**, 76 (1969).

[70] T. Golod, A. Rydh, and V. M. Krasnov, "Anomalous Hall effect in NiPt thin films", *Journal of Applied Physics* **110**, 033909 (2011).

[71] E. Hall, "XXIX. On a new action of the magnet on electric currents", *Philosophical Magazine and Journal of Science* **9**, 225 (1880).

[72] A. Gerber, A. Milner, L. Goldshmit, M. Karpovski, B. Lemke, H.-U. Habermeier, and A. Sulpice, "Effect of surface scattering on the extraordinary Hall coefficient in ferromagnetic films", *Physical Review B* **65**, 054426 (2002).

[73] S. A. Boye, P. Lazor, and R. Ahuja, "Magnetoresistance and Hall-effect measurements of Ni thin films", *Journal of Applied Physics* **97**, 083902 (2005).

[74] P. P. Madduri and S. Kaul, "Magnon-induced interband spin-flip scattering contribution to resistivity and magnetoresistance in a nanocrystalline itinerant-electron ferromagnet: Effect of crystallite size", *Physical Review B* **95**, 184402 (2017).

[75] A. Mihai, J. Attané, A. Marty, P. Warin, and Y. Samson, "Electron-magnon diffusion and magnetization reversal detection in FePt thin films", *Physical Review B* **77**, 060401 (2008).

[76] B. Raquet, M. Viret, E. Sondergard, O. Cespedes, and R. Mamy, "Electron-magnon scattering and magnetic resistivity in 3d ferromagnets", *Physical Review B* **66** (2002).

[77] G. Winkler, *Korrelation zwischen strukturellen und magnetogalvanischen Eigenschaften von Pt/Co/Pt- und Pd/Co/Pd-Schichtsystemen*, Ph.D. thesis, Hamburg University (2015).

[78] W. R. Grove, "On the electro-chemical polarity of gases", *Philosophical Transactions of the Royal Society of London* **142**, 87 (1852).

[79] J. Plücker, "Über die Einwirkung des Magneten auf die elektrischen Entladungen in verdünnten Gasen", *Annalen der physik* **103**, 88 (1858).

[80] R. Behrisch and K. Wittmaack, *Sputtering by particle bombardment III: characteristics of sputtered particles, technical applications - Topics in applied physics*, (Springer Verlag, 1991).

[81] T. Motohiro, Y. Taga, and K. Nakajima, "Study of angular factors in sputter-deposition using the ion beam method", *Surface Science* **118**, 66 (1982).

[82] K. Wasa, *Handbook of Sputter Deposition Technology: Fundamentals and Applications for Functional Thin Films, Nano-Materials and MEMS*, (William Andrew, 2012).

[83] S. Swann, "Magnetron sputtering", *Physics in technology* **19**, 67 (1988).

[84] R. Behrisch, *Sputtering by Particle Bombardment I: Physical Sputtering of Single-Element Solids*, (Springer Berlin Heidelberg, 1981).

[85] P. Kelly and R. Arnell, "Magnetron sputtering: a review of recent developments and applications", *Vacuum* **56**, 159 (2000).

[86] T. Ono, C. Takahashi, and S. Matsuo, "Electron cyclotron resonance plasma deposition technique using raw material supply by sputtering", *Japanese Journal of Applied Physics* **23**, L534 (1984).

[87] M. Francombe and J. Vossen, *Plasma Sources for Thin Film Deposition and Etching - Physics of thin films: advances in research and development*, (Academic Press, 1994).

[88] M. Wellhöfer, M. Weissenborn, R. Anton, S. Pütter, and H. P. Oepen, "Morphology and magnetic properties of ECR ion beam sputtered Co/Pt films", *Journal of Magnetism and Magnetic Materials* **292**, 345 (2005).

[89] E. D. McClanahan and N. Laegreid, *Production of thin films by controlled deposition of sputtered material*, (Springer, Berlin, Heidelberg, 1991).

[90] R. Anton, T. Wiegner, W. Naumann, M. Liebmann, C. Klein, and C. Bradley, "Design and performance of a versatile, cost-effective microwave electron cyclotron resonance plasma source for surface and thin film processing", *Review of Scientific Instruments* **71**, 1177 (2000).

[91] H. Stillrich, C. Menk, R. Frömter, and H. P. Oepen, "Magnetic anisotropy and spin reorientation in Co/Pt multilayers: Influence of preparation", *Journal of Magnetism and Magnetic Materials* **322**, 1353 (2010).

[92] J. Als-Nielsen and D. McMorrow, *Elements of Modern X-ray Physics*, (Wiley, 2011).

[93] M. Birkholz, *Thin Film Analysis by X-Ray Scattering*, (Wiley, 2006).

[94] H. Kiessig, "Interferenz von Röntgenstrahlen an dünnen Schichten", *Annalen der Physik* **402**, 769 (1931).

[95] J. Daillant and A. Gibaud, "X-ray and neutron reflectivity", *Lecture Notes in Physics Monographs* (1999).

[96] A. Benediktovich, I. Feranchuk, and A. Ulyanenkov, *Theoretical Concepts of X-Ray Nanoscale Analysis - Theory and Applications*, (Springer Berlin Heidelberg, 2014).

[97] B. Cullity and S. Stock, *Elements of X-Ray Diffraction: Pearson New International Edition*, (Pearson Education, 2013).

[98] M. B. Stearns, *Magnetic Properties of Metals, 3d, 4d and 5d Elements, Alloys and Compounds 19a*, (Springer Verlag, 1986).

[99] E. Zolotoyabko, *Basic concepts of X-ray diffraction*, (Wiley VCH, 2014).

[100] B. Cullity, *Elements of X-ray Diffraction*, (Addison Wesley Publishing Company, 1956).

[101] B. E. Warren, *X-ray diffraction*, (Dover Publications, 1990).

[102] A. Kobs and H. P. Oepen, "Disentangling interface and bulk contributions to the anisotropic magnetoresistance in Pt/Co/Pt sandwiches", *Physical Review B* **93** (2016).

[103] C. H. MacGillavry and G. D. Rieck, *International Tables for X-Ray Crystallography Vol. III Physical and Chemical Tables*, (The Kynoch Press, 1968).

[104] C. Suryanarayana and M. G. Norton, *X-Ray Diffraction A Practical Approach*, (Springer Science + Business Media, 1998).

[105] J. A. C. Bland and B. Heinrich, *Ultrathin Magnetic Structure I: An Introduction to the Electronic, Magnetic and Structural Properties*, (Springer-Verlag, 2005).

[106] U. Pietsch, V. Holý, and T. Baumbach, *High-Resolution X-Ray Scattering*, (Springer New York, 2004).

[107] L. Névot and P. Croce, "Caractérisation des surfaces par réflexion rasante de rayons X. Application à l'étude du polissage de quelques verres silicates", *Revue de Physique Appliquée* **15**, 761 (1980).

[108] L. G. Parratt, "Surface Studies of Solids by Total Reflection of X-Rays", *Physical Review* **95**, 359 (1954).

[109] A. Nelson, "Co-refinement of multiple-contrast neutron/X-ray reflectivity data using MOTOFIT", *Journal of Applied Crystallography* **39**, 273 (2006).

[110] L. Maksymowicz and H. Jankowski, "Effective magnetic anisotropy field of Pd/Ni multilayers", *Journal of Magnetism and Magnetic Materials* **147**, 409 (1995).

[111] J. M. Shaw, H. T. Nembach, T. J. Silva, S. E. Russek, R. Geiss, C. Jones, N. Clark, T. Leo, and D. J. Smith, "Effect of microstructure on magnetic properties and anisotropy distributions in Co/Pd thin films and nanostructures", *Physical Review B* **80** (2009).

[112] A. O. Adeyeye, J. A. C. Bland, C. Daboo, J. Lee, U. Ebels, and H. Ahmed, "Size dependence of the magnetoresistance in submicron FeNi wires", *Journal of Applied Physics* **79**, 6120 (1996).

[113] V. A. Marsocci, "Magnetoresistance and Hall-Voltage Measurements on Single-Crystal Ni and Ni-Fe Thin Films", *Journal of Applied Physics* **35**, 774 (1964).

[114] W. Döring, "Die Abhängigkeit des Wiederstandes von Nickelkristallen von der Richtung der spontanen Magnetisierung", *Annalen der Physik* (1938).

[115] T. Chen and V. Marsocci, "Planar magnetoresistivity and planar Hall effect measurements in nickel single-crystal thin films", *Physica* **59**, 498 (1972).

[116] H.-l. Liu, T. Skeren, A. Volodin, K. Temst, A. Vantomme, and C. Van Haesendonck, "Tailoring the magnetic anisotropy, magnetization reversal, and anisotropic magnetoresistance of Ni films by ion sputtering", *Physical Review B* **91** (2015).

[117] R. Ramos, S. K. Arora, and I. V. Shvets, "Anomalous anisotropic magnetoresistance in epitaxial Fe_3O_4 thin films on MgO(001) ", *Phys. Rev. B* **78** (2008).

[118] R. Ramos, S. K. Arora, and I. V. Shvets, "Influence of miscut on the anisotropic magnetoresistance of magnetite thin films", *Journal of Applied Physics* **105**, 07B108 (2009).

[119] P. Li, B. Guo, and H. L. Bai, "Large anisotropic magnetoresistance across the Schottky interface in all oxide ferromagnet/semiconductor heterostructures", *Europhysics Letters* **94**, 57007 (2011).

[120] N. Naftalis, A. Kaplan, M. Schultz, C. A. F. Vaz, J. A. Moyer, C. H. Ahn, and L. Klein, "Field-dependent anisotropic magnetoresistance and planar Hall effect in epitaxial magnetite thin films", *Physical Review B* **84** (2011).

[121] P. Li, C. Jin, E. Y. Jiang, and H. L. Bai, "Origin of the twofold and fourfold symmetric anisotropic magnetoresistance in epitaxial Fe_3O_4 films", *Journal of Applied Physics* **108**, 093921 (2010).

[122] D. Wu, P. Wei, E. Johnston-Halperin, D. D. Awschalom, and J. Shi, "High-field magnetocrystalline anisotropic resistance effect in (Ga,Mn)As", *Physical Review B* **77** (2008).

[123] J. Li, S. L. Li, Z. W. Wu, S. Li, H. F. Chu, J. Wang, Y. Zhang, H. Y. Tian, and D. N. Zheng, "A phenomenological approach to the anisotropic magnetoresistance and planar Hall effect in tetragonal $La_{2/3}Ca_{1/3}MnO_3$ thin films", *Journal of Physics: Condensed Matter* **22**, 146006 (2010).

[124] R. Van Gorkom, J. Caro, T. Klapwijk, and S. Radelaar, "Temperature and angular dependence of the anisotropic magnetoresistance in epitaxial Fe films", *Physical Review B* **63**, 134432 (2001).

[125] F. Takata, K. Kabara, K. Ito, M. Tsunoda, and T. Suemasu, "Negative anisotropic magnetoresistance resulting from minority spin transport in $Ni_xFe_{4-x}N$ (x = 1 and 3) epitaxial films", *Journal of Applied Physics* **121**, 023903 (2017).

[126] K. Ito, K. Kabara, T. Sanai, K. Toko, Y. Imai, M. Tsunoda, and T. Suemasu, "Sign of the spin-polarization in cobalt-iron nitride films determined by the anisotropic magnetoresistance effect", *Journal of Applied Physics* **116**, 053912 (2014).

[127] J. J. Thomson, "On the theory of electric conduction through thin metallic films", *Mathematical Proceedings of the Cambridge Philosophical Society* **11**, 118 (1901).

[128] K. Fuchs, "The conductivity of thin metallic films according to the electron theory of metals", *Mathematical Proceedings of the Cambridge Philosophical Society* **34**, 100 (1938).

[129] P. J. Price, "Anisotropic conduction in solids near surfaces", *IBM Journal of Research and Development* **4**, 152 (1960).

[130] E. Sondheimer, "The mean free path of electrons in metals", *Advances in Physics* **1**, 1 (1952).

[131] L. Zou, Y. Zhang, L. Gu, J. Cai, and L. Sun, "Tunable angular-dependent magnetoresistance correlations in magnetic films and their implications for spin Hall magnetoresistance analysis", *Physical Review B* **93**, 075309 (2016).

[132] N. Thanh, L. Tu, N. Ha, C. Kim, C. Kim, K. Shin, and B. Parvatheeswara Rao, "Thickness dependence of parallel and perpendicular anisotropic resistivity in Ta/NiFe/IrMn/Ta multilayer studied by anisotropic magnetoresistance and planar Hall effect", *Journal of Applied Physics* **101**, 053702 (2007).

[133] R. Rowan-Robinson, A. Hindmarch, and D. Atkinson, "Enhanced electron-magnon scattering in ferromagnetic thin films and the breakdown of the Mott two-current model", *Physical Review B* **90**, 104401 (2014).

[134] C.-J. Zhao, L. Ding, J.-S. HuangFu, J.-Y. Zhang, and G.-H. Yu, "Research progress in anisotropic magnetoresistance", *Rare Metals* **32**, 213 (2013).

[135] C. Leroux, M. Cadeville, V. Pierron-Bohnes, G. Inden, and F. Hinz, "Comparative investigation of structural and transport properties of L10 NiPt and CoPt phases; the role of magnetism", *Journal of Physics F: Metal Physics* **18**, 2033 (1988).

[136] L. Reimer, "Measurements of the Hall effect on ferromagnetic nickel layers", *Z. Phys.* **150**, 277 (1958).

[137] C. Ghosh and A. Pal, "Electrical resistivity and galvanomagnetic properties of evaporated nickel films", *Journal of Applied Physics* **51**, 2281 (1980).

[138] G. Wedler and H. Schneck, "Galvanomagnetic and magnetic properties of evaporated thin nickel films II. Thickness dependence of the Hall coefficients, the magnetoresistivity and the saturation magnetization", *Thin Solid Films* **47**, 147 (1977).

[139] G. Wedler and H. Schneck, "Galvanomagnetic and magnetic properties of evaporated thin nickel films I: Field dependence of the Hall voltage and the magnetoresistivity", *Thin Solid Films* **47**, 137 (1977).

[140] A. Gerber, A. Milner, M. Karpovsky, B. Lemke, H.-U. Habermeier, J. Tuaillon-Combes, M. Negrier, O. Boisron, P. Melinon, and A. Perez, "Extraordinary Hall effect in magnetic films", *Journal of Magnetism and Magnetic Materials* **242**, 90 (2002).

[141] A. Gerber, A. Milner, A. Finkler, M. Karpovski, L. Goldsmith, J. Tuaillon-Combes, O. Boisron, P. Mélinon, and A. Perez, "Correlation between the extraordinary Hall effect and resistivity", *Physical Review B* **69**, 224403 (2004).

[142] K. Baberschke, "The magnetism of nickel monolayers", *Applied Physics A: Materials Science and Processing* **62**, 417 (1996).

[143] N. W. Ashcroft and N. D. Mermin, *Solid State Physics*, (Saunders College, Philadelphia, 1976).

[144] G. K. White and S. Woods, "Electrical and thermal resistivity of the transition elements at low temperatures", *Philosophical Transactions of the Royal Society of London A: Mathematical, Physical and Engineering Sciences* **251**, 273 (1959).

[145] S. Kim, H. Suhl, and I. K. Schuller, "Surface phonon scattering in the electrical resistivity on Co/Ni superlattices", *Physical Review Letters* **78**, 322 (1997).

[146] M. V. Kamalakar and A. Raychaudhuri, “Low temperature electrical transport in ferromagnetic Ni nanowires”, *Physical Review B* **79**, 205417 (2009).

[147] S. Vitta, A. Khuntia, G. Ravikumar, and D. Bahadur, “Electrical and magnetic properties of nanocrystalline $\mathrm{Fe}_{100-x}\mathrm{Ni}_x$ alloys”, *Journal of Magnetism and Magnetic Materials* **320**, 182 (2008).

[148] D. Grieg and J. Harrison, “The low temperature electrical transport properties of nickel and dilute nickel-copper alloys”, *Philosophical Magazine* **12**, 71 (1965).

[149] P. Carcia, “Perpendicular magnetic anisotropy in Pd/Co and Pt/Co thin-film layered structures”, *Journal of applied physics* **63**, 5066 (1988).

[150] N. Sato, “Crystallographic structure and magnetism of co-pd and co-pt films with an artificially layered structure”, *Journal of applied physics* **64**, 6424 (1988).

[151] B. Lairson, J. Perez, and C. Baldwin, “Pd/Co multilayers for perpendicular magnetic recording”, *IEEE Transactions on Magnetics* **30**, 4014 (1994).

[152] D. Rosenblatt, M. Karpovski, and A. Gerber, “Reversal of the extraordinary Hall effect polarity in thin Co/Pd multilayers”, *Applied Physics Letters* **96**, 022512 (2010).

[153] G. Winer, A. Segal, M. Karpovski, V. Shelukhin, and A. Gerber, “Probing Co/Pd interfacial alloying by the extraordinary Hall effect”, *Journal of Applied Physics* **118**, 173901 (2015).

[154] S.-K. Kim, Y.-M. Koo, V. A. Chernov, J. Kortright, and S.-C. Shin, “Comparison of atomic structure anisotropy between Co-Pd alloys and Co/Pd multilayer films”, *Physical Review B* **62**, 3025 (2000).

[155] F. Wen, F. Zhang, Y. Lü, J. Xiang, W. Li, Y. Lu, Z. Liu, B. Xu, D. Yu, J. He *et al.*, “Time dependence of interlayer coupling in Pd(50 Å)/Co(t_{Co} Å)/Pd(54 Å)/Co(t_{Co} Å)/Pd(50 Å) multilayer with perpendicular anisotropy”, *Journal of Applied Physics* **110**, 043918 (2011).

[156] M. Pasturel, M. Slaman, H. Schreuders, J. Rector, D. Borsa, B. Dam, and R. Griessen, “Hydrogen absorption kinetics and optical properties of Pd-doped Mg thin films”, *Journal of applied physics* **100**, 023515 (2006).

[157] B. Hjörvarsson, J. Dura, P. Isberg, T. Watanabe, T. Udovic, G. Andersson, and C. Majkrzak, “Reversible tuning of the magnetic

exchange coupling in Fe/V (001) superlattices using hydrogen", *Physical review letters* **79**, 901 (1997).

[158] G. Andersson, B. Hjörvarsson, and H. Zabel, "Hydrogen-induced lattice expansion of vanadium in a Fe/V (001) single-crystal superlattice", *Physical Review B* **55**, 15905 (1997).

[159] D. Matsumura, T. Nakagawa, H. Watanabe, H. Abe, K. Amemiya, T. Ohta, and T. Yokoyama, "Magnetization process of Co/Pd (111) thin films: Chemisorption-induced spin-reorientation transition", *Surface Science* **602**, 1999 (2008).

[160] F. J. Ackerman and G. J. Koskinas, "Permeation of hydrogen and deuterium through palladium-silver alloys", *Journal of Chemical and Engineering Data* **17**, 51 (1972).

[161] Y.-M. Lin and M.-H. Rei, "Process development for generating high purity hydrogen by using supported palladium membrane reactor as steam reformer", *International Journal of Hydrogen Energy* **25**, 211 (2000).

[162] N. Mott, "A discussion of the transition metals on the basis of quantum mechanics", *Proceedings of the Physical Society* **47**, 571 (1935).

[163] H. Jamieson and F. Manchester, "The magnetic susceptibility of Pd, PdH and PdD between 4 and 300 K", *Journal of Physics F: Metal Physics* **2**, 323 (1972).

[164] K. Munbodh, F. A. Perez, and D. Lederman, "Changes in magnetic properties of Co/Pd multilayers induced by hydrogen absorption", *Journal of Applied Physics* **111**, 123919 (2012).

Conference contributions

- Afsaneh Farhadi Ghalati, André Philippi-Kobs, Dieter Lott, Jonathan Jacobsohn, Gerrit Winkler, and Hans Peter Oepen, "Impact of aging process on the magnetotransport properties of Co/Pd layered structures", Poster at Spring-meeting of the German Physical Society, Dresden (2017)

- Afsaneh Farhadi Ghalati, André Kobs, Gerrit Winkler, Carsten Thönnissen, and Hans Peter Oepen, "Higher order contributions to Anisotropic Interface Magnetoresistance (AIMR) in Ni/Pt thin films", Talk at Spring-meeting of the German Physical Society, Berlin (2015)

- André Kobs, Afsaneh Farhadi Ghalati, Gerrit Winkler, Carsten Thönnissen, and Hans Peter Oepen, "Higher order contributions to the Anisotropic Interface Magnetoresistance (AIMR) in Ni/Pt layered structures", Poster at the International Colloquium on Magnetic Films and Surfaces (ICMFS), Poland (2015)

- Axel Frauen, André Kobs, Tim Böhnert, Ann-Kathrin Michel, Afsaneh Farhadi Ghalati, Kornelius Nielsch, and Hans Peter Oepen, "Anisotropic interface contributions to the magnetothermoelectric power (MTEP) in Co/Pt layered structures", Poster at Spring-meeting of the German Physical Society, Berlin (2015)

Acknowledgement

This work would not have been possible without the support of many people, all of whom I would like to thank at this point.

First of all, I am fully indebted to Prof. Dr. Hans Peter Oepen for giving me the opportunity to pursue my education and fulfill my dream of doing my PhD in this field. I would like to acknowledge him for numerous discussions, for his understanding and patience, and for pushing me forward in this challenging way. In addition, I would like to express my gratitude to Prof. Dr. Wolfgang Hansen for accepting to review this thesis as the second referee.

A special thanks goes to Dr. André Philippi-Kobs, who has played a key role in coordinating the whole project, for his support, continuous guidance, suggestions, and for his inexhaustible patience during the correction phase of this dissertation.

I am also grateful to all members of group G, Dr. Robert Frömter, Dr. Gerrit Winkler, Dr. Mahmoud Reza Rahbar Azad, Dr. Axel Frauen, Dr. Edna Corredor Vega, Eva Wilhelm, Jonathan Jacobsohn, Sussane Kuhrau, Philipp Staeck, Carsten Thönnißen, Jochen Wagner, Sonja Hesselmann, Brigitte Muhlack, and all other former and present members, with whom I have had the pleasure to work during my professional time at Hamburg university. Furthermore, I would also like to wish my sincere thanks to Stephanie Baer (Prof. Oepen's secretary), for her cordial helps in all organizational affairs from the very beginning of my arrival to Germany.

Besides Group G, I am feeling obliged to take this opportunity and thank Dr. M. Reza Bakhtiari, to whom I am highly indebted for his beneficial suggestions and supports during hard time of doctoral journey and also for his feedback on an earlier version of this thesis. Next to him, special thanks goes to all of my friends for helping me survive all the stresses of the work and not letting me give up.

Finally, I would express a deep sense of gratitude to my parents and my brothers, for their unbelievable support, love, and inspiration in spite of being far away from me. They are the most important people in my world and I dedicate this thesis to them.

Eidesstattliche Versicherung / Declaration on oath

Hiermit versichere ich an Eides statt, die vorliegende Dissertationsschrift selbst verfasst und keine anderen als die angegebenen Hilfsmittel und Quellen benutzt zu haben.
Die eingereichte schriftliche Fassung entspricht der auf dem elektronischen Speichermedium.
Die Dissertation wurde in der vorgelegten oder einer ähnlichen Form nicht schon einmal in einem früheren Promotionsverfahren angenommen oder als ungenügend beurteilt.

Hamburg, den